DEEP SEISMIC REFLECTION IMAGING USING SOURCES OF OPPORTUNITY RECORDED BY DENSE SEISMIC ARRAYS

A Dissertation

Presented to the Faculty of the Graduate School

of Cornell University

In Partial Fulfillment of the Requirements for the Degree of

Doctor of Philosophy

by

Doyeon Kim

May 2018

DEEP SEISMIC REFLECTION IMAGING USING SOURCES OF OPPORTUNITY RECORDED BY DENSE SEISMIC ARRAYS

Doyeon Kim, Ph. D.

Cornell University 2018

The main focus of this dissertation is development of innovative approaches to the high resolution imaging of the earth that take advantage of recent advances in seismic instrumentation (dense arrays) which facilitate the unaliased recording of local earthquakes. These new methods can be applied to the study of any structures at depth as long as there is an adequate distribution of local seismic energy available for effective illumination.

Introduction places the research reported in this dissertation in the context of the broader field of seismic imaging.

Chapter 1 investigates geometries favorable to body wave imaging by interferometric analysis of distributed but known subsurface sources, with application to the aftershock sequence of the 2011 Mw 5.8 Virginia earthquake.

Chapter 2 and Chapter 3 use microseismicity recordings at the geothermal field at Krafla, Iceland, to image magmatic features at depth using two distinct approaches: seismic interferometry and reverse Vertical Seismic Profiling (rVSP). Strong reflections from a body at the same depth as magma encountered in boreholes at Krafla, Iceland were detected and mapped by both techniques. Deeper reflectors suggest a distributed system of smaller magma sills rather than a large pervasively molten feeder chamber at Krafla.

Chapter 4 reports an effort to use subduction zone earthquakes in central Alaska to produce a high resolution image of the subducting oceanic lithosphere. The

results include one of the first seismic images using an interferometric method with local earthquakes to successfully image mantle structure with a greater resolution than that previously achieved with more conventional methods.

Chapter 5 of this dissertation presents the first industry scale 3D reflection image of deep intrabasement features in the United States, generated by opportunistic processing of pre-existing oil exploration data. More importantly, this work illustrates how modern, nodal industry seismic reflection surveys are routinely collecting 3D imagery that- if preserved and properly processed- can yield important new insights into the structure and evolution of the deeper parts of the earth.

BIOGRAPHICAL SKETCH

Doyeon was born October 14th 1984 in Tallahassee, Florida, to HyunPyo Kim Ph. D. and YoungSook Jung M.S. He earned the privilege of receiving a dual-citizenship in the U.S. and South Korea after honorable discharge in 2008 as a non-commissioned officer at U.S. Army Garrison Humphreys Camp Long at Wonju, Korea.

Geophysics was not an initial academic choice for Doyeon. He earned a B.S. in Civil Engineering and M.S. in Civil and Environmental Engineering at Yonsei University, Korea in 2010 and 2012, respectively. In summer 2013, Doyeon entered the Ph. D. program in Civil and Environmental Engineering at Cornell University, working with Prof. William Philpot to develop a physically based optical model in remote sensing that can account for the effect of soil moisture content.

In summer 2014, Doyeon decided to change his academic concentration to Geophysics, due to his shifting interest from surface processes to the entire earth system. Under the direction of Prof. Larry Brown, Doyeon entered the Graduate Program in Geological Sciences at Cornell. The dissertation presented here is the result of his academic research during the Ph. D. program.

ACKNOWLEDGMENTS

I would like to acknowledge my appreciation to all of the financial support I have received to accomplish the work presented in this dissertation. This includes National Science Foundation (NSF) Division of Earth Sciences (EAR) (Grant No. 1347262) and NSF Interdisciplinary Graduate Education and Research Traineeship (IGERT) Fellowships (Grant No. 966045) provided by Earth-Energy Institute at Cornell University, research and teaching assistantships, travel grants from the department of Earth and Atmospheric Sciences and the graduate school, and a summer support at Lawrence Livermore National Laboratory (LLNL).

I thank many individuals who inspired me to pursue my academic career as a Ph. D. First and foremost, I thank Dr. Hyunpyo Kim, my father, for allowing me to realize my potential. His strong influence as a professor led me to pursue an advanced degree. I also need to thank Prof. Heo Joon and Prof. Hong-gyu Sohn for their support and guidance during my B.S. and M.S. studies at Yonsei University.

I also thanks to all the people I have met at Cornell University. I acknowledge Dr. William Philpot for initially making it possible for me to purse Ph. D. degree at Cornell. I am very grateful that he supported my academic growth, even though it deviated from his own.

All of the members in EAS community, I would like to express my sincere gratitude to all of you for your contributions to the department. I thank Prof. Jeff Tester for his invitation to Earth-Energy Institute for me to start the core of my dissertation project in Iceland. I thank to Prof. Geoff Abers for welcoming me to work with him and providing a different perspective of earth science, as well as showing a vested interest in my academic career. Special thanks to Prof. Emeritus Muawia Barazangi and Nimat Barazangi for your countless lessons and advices in both life and

science. My fellow colleagues in EAS: Casey Root, Chris Siron, John Mason, Michael Mann, Dana Peterson, Juan Carlos, Cat Lambert, Nate Stevens, Kayla Crosbie, Kyle Murray, Roque Soto, Paula Burgi, Paul Morgan, Whyjay Zheng, Joey Durkin, Francisco Delgaro, Alida Fodich, Katie Grant, Andres Aguirre, and Andrea Aguirre, thank you for making my PhD experience rich and enjoyable.

Thanks to my collaborators for sharing their knowledge and providing numerous support of any kind: Rengin Gok, Kevin Mayeda, Jorge Roman-Nieves, Knútur Árnason, Kristján Ágústsson, Gylfi Páll Hersir, Ólafur G. Flóvenz, Ólafur Gudmundsson, Anastasija Cabolova, Lauren McLeod, and Diego Quiros.

Thanks to my families and friends. To my parents, Hyunpyo Kim and Youngsook Jung, and my brother Dohyoung Kim, you should know that your encouragement was worth more than I can express on paper. Special thanks to Tayo Johnson for endless moral support whom I love so much. Without her, I may never have gotten this far.

I have had so many exciting fieldwork opportunities: train noise experiment in New Mexico, a wind noise experiment in New York, Cornell Earth Source Heating project, magmatic system in Iceland, induced seismicity in Oklahoma, East African rift study in Ethiopia, and volcanoes in Chile. Many of these amazing opportunities were provided by Prof. Katie Keranen. I am truly grateful of her for trusting my work and mentoring me to become an earth scientist.

Many thanks to Prof. Greg McLaskey who graciously agreed to serve on my dissertation committee. His Time Series and Data Analysis class is by far my favorite class at Cornell University, and his guidance during my PhD has been invaluable.

Finally, I thank my advisor, Prof. Larry Brown. It has been an honor to be one of his graduate students. He has been always supportive and taught me countless things. More than anything, I learned how to enjoy science under his supervision.

TABLE OF CONTENTS

INTRODUCTION

Seismic imaging has played an essential role in advancing our understanding of the geometries and physical properties of the interior of the earth. To the first order, seismic resolution depends on the wavelength of a seismic source with which the subsurface is measured. Controlled source seismic methods can resolve small structures in the upper few km with great accuracy, in part because relatively high frequency sources are available and in part because industry has developed processing methods that take great advantage of highly redundant (e.g., high-fold) wavefield sampling. However, ultimately signal penetration is limited by the size of the artificial sources that are practical (*e.g.,* Oliver et al., 1976). Moreover controlled source methods tend to be relatively expensive because of the large number of sensors required and the cost of artificially generated seismic wave. In contrast, techniques associated with earthquake seismology (*e.g.,* seismic tomography, receiver functions), are capable of imaging deeper but are fundamentally limited by the low frequency available from teleseismic sources for imaging (Figure 1).

In this dissertation, we propose to apply a new, complimentary approach to probing, and ultimately monitoring, the earth's interior using body waves from local earthquakes. Here, we investigate body waves that have been reflected from subsurface interfaces. Because local earthquakes provide higher frequencies than teleseismic sources, higher resolution can be expected. Because this approach uses natural sources rather than expensive controlled sources, the lower cost will translate into greater feasibility for 3D as well as time lapse (*e.g.,* 4D) reflection imaging, the latter having special relevance to monitoring active subsurface processes. Of course, this approach is highly dependent upon having sufficient seismicity within an observation period. Also, true high-frequency imaging requires wavefield sampling

that is unaliased at the wavelengths of the signals being used (*e.g.,* Rost and Thomas, 2002).

In this regards, the use of "Large N" seismic recording system is required to fully utilize those high frequency sources and produce accurate seismic image. An adequate "Large N" seismic recording system would require the deployment of multiple seismometers with spacing small enough that both the waveforms and the structure of interest are not spatially aliased. For example, the 300 – 500 m station spacing will allow coherent stacking to 10 – 25 Hz for phase velocities of appropriate for reflections at 30 km depth (Figure 2). Such a "Large N" array for passive recording has recently become more feasible by the development of nodal recordings systems by the oil exploration industry (*e.g.,* Lin et al., 2013).

This dissertation applies these techniques to three very distinct types of geological targets: 1) an active, intraplate fault zone in the upper crust, 2) a volcanic system along a mid-ocean ridge, and 3) a subduction zone representative of the Pacific Rim. In the final chapter is a demonstration of how reprocessing of modern, nodal "Large N" industry surveys that are now being routinely collected to explore the sedimentary rocks of shallow basins, can use to generate valuable 3D imagery of the underlying basement.

Figures

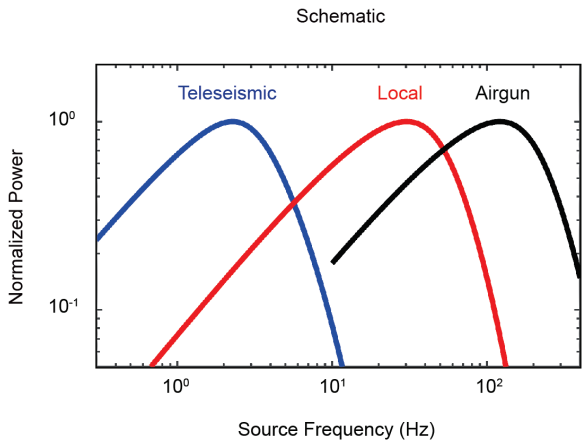

Figure 1: Schematic source frequencies from typical teleseismic, and local earthquake, and controlled source (e.g. airgun) seismic sources.

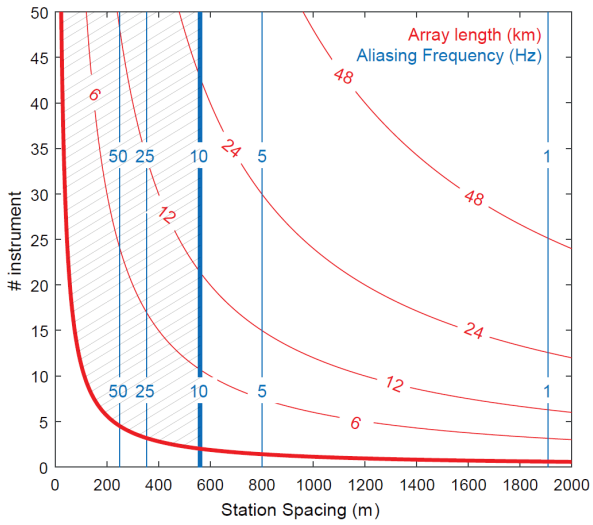

Figure 2: Array design factors for imaging with local earthquakes. Blue lines show maximum unaliased frequency of P-waves of an earthquake at 28 km depth reflecting at an interface at 30 km depth. Red lines show total array length. Thick red line shows Fresnel zone width for a 30 km deep reflection at 10 Hz, expressed as total array length. To sample multiple Fresnel zones (50% overlap) the array must be longer than this width, but with station short enough to record 10 Hz energy (this corresponds to the shaded region between two bold lines).

REFERENCE

Lin, F.-C., D. Li, R. W. Clayton, and D. Hollis (2013b), High-resolution 3D shallow crustal structure in Long Beach, California: Application of ambient noise tomography on a dense seismic array, Geophysics, 78(4), Q45–Q56.

Oliver, J., M. Dobrin, S. Kaufman, R. Meyer, and R. Phinney. (1976) Continuous seismic reflection profiling of the deep basement, Hardeman County, Texas: Geological Society of America Bulletin, 87, 1537-1546.

Rost, S., and C. Thomas (2002), Array seismology: Methods and applications, Rev. Geophys., 40(3), 1008, doi:1010.1029/2000RG000100.

CHAPTER 1

VIRTUAL REFLECTION IMAGING WITH AFTERSHOCK SOURCES

1.1 Abstract

Application of interferometry to recording of ambient "noise" (microseisms) has proven widely successful in recovering surface wave information for imaging crustal velocity structures. While the theoretical foundations of recovering body waves with seismic interferometry are well established, such recovery has proven to be challenging in practice. In this study we investigate the geometries favorable to body wave imaging by common reflection point stacking of virtual shot gathers computed by applying interferometry to subsurface aftershock sources. We test these methods using high spatial density recordings collected after the Mw 5.8 Mineral, Virginia earthquake of 2011. The approach described here represents a promising new means of body wave imaging of 3D structure that can be applied to a wide array of geologic and energy problems that involves natural or induced seismic clusters.

1.2 Introduction

Recent research has shown how the ambient seismic wave field can be used as a source for subsurface imaging using a technique called seismic interferometry (Claerbout, 1968; Rickett and Claerbout, 1999). Seismic interferometry involves cross-correlation of the recordings from two seismic receivers to generate a "virtual" signal which can be interpreted as the travel-time of the signal from one receiver as if there was a source at the other. Among the attractions of this technique is that real seismic sources (intractable for natural sources; expensive for artificial, controlled sources) are replaced by “virtual” sources constructed from "free" energy already in the environment. Seismic interferometry is perhaps best known for its success in facilitating surface wave tomography from ambient microseismic “noise” (e.g. Shapiro

A portion of the material in Chapter 1 has been published under Kim et al., Body wave imaging with interferometry of aftershock sources, *Society of Exploration Geophysicists New Orleans Annual Meeting 2015, http://doi.org/10.1190/segam2015-5931020.1*

et al, 2005; Lin et al., 2008) and less widely appreciated for industry applications using artificial sources (Schuster, 2009; Wapenaar et al., 2010). However, the effectiveness of interferometry in extracting useful body wave information from ambient noise has not been entirely convincing, albeit with some notable success (e.g. Roux et al., 2005, Draganov et al, 2007; Zhan et al., 2010; Ryberg, 2011 and Lin et al, 2013).

The reflection response of layered media can be recovered by correlating the transmission response with itself that is autocorrelation (Claerbout, 1968) (Figure 1.1). The reflection record from the “virtual” source produced by autocorrelation provides the reflection response one would record from a real source at the surface coincident with a receiver. The virtual reflection trace does not depend on either the time or the depth of the source. As a result, the virtual records computed from N independent recordings can be stacked to increase the signal amplitude by the factor of N. If we were to stack a number of randomly distributed sources aligned vertically beneath the station, the process could properly be called "ambient noise" imaging (i.e. the individual sources playing the role of "noise"). Note that in this situation the signal associated with initially downgoing energy from sources at various depths will tend to interfere destructively with a resulting degradation of the associated artifact shown in Figure 1.1. The vertical angle of incidence in this case corresponds to a stationary phase. If the structures of interest can be approximated as flat-lying layers of constant velocity and there were to exist real sources beneath every surface location, we could "profile" the subsurface by moving a single station along the ground, or by deploying an array of stations to record the vertically traveling energy to image reflectivity vs. depth beneath it. For body-wave sources that are sufficiently numerous and suitably distributed, reflections can be extracted from such ambient noise using this approach (e.g. Vidal et al., 2014; Ito and Shiomi, 2012). Ito and Shiomi (2012) for example,

used a brute force autocorrelation approach to image dipping energy that they interpret as reflections from the subducting Pacific plate beneath Honshu, Japan. Alternatively, Ruigrok and Wapenaar (2012) autocorrelated body waves from earthquakes at global distances that contain stationary raypaths to recover P-wave reflectivity below the Himalayas and Tibetan Plateau.

Nevertheless, the real world has strong 3D structural and velocity complexity, and sources are not always vertically aligned with recording stations nor sufficiently random in their distribution. Here we explore an imaging procedure that is generalized for non-coincident receivers that record subsurface sources that are offset from the receivers by adapting conventional Common Reflection Point (CRP) methods to interferometric geometries.

Using synthetic seismograms we have evaluated geometries representing realistic distribution of subsurface sources and corresponding surface receivers that can result in useful stacking of virtual body wave energy to produce seismic reflection imagery. To explore the feasibility of this approach in practice, seismic recordings of 50 aftershocks following the magnitude of Mw 5.8 Mineral, Virginia, earthquake that occurred in August, 2011 have been processed to produce seismic reflection images of the crustal structure in the vicinity of the aftershock cluster.

1.3 Method and Discussion

1.3.1 Synthetic seismograms

Synthetic seismograms were computed for subsurface sources analogous to microearthquake distributions as they would be recorded by a linear array of 59 receivers at the free surface spaced 200m apart (Figure 1.2). The seismograms were computed using the CREWES 2nd order finite difference code (Margrave, 2001) and assuming each source was a simple impulse representable as a Ricker wavelet with frequencies of 15-40 Hz (Margrave, 2001). The number of stations, station spacing

and the depth range of sources (from 3 to 5km) were selected to mimic the parameters used in the Virginia experiment. A simple flat, velocity model with a reflector at 6 km depth was the basis of the modeling. This depth was selected to correspond to that of reflectors identified by a conventional crustal reflection surveying conducted near the epicentral area of the Virginia event in 1981 (e.g. Pratt et al. 1988; 2015).

Figure 1.2a is a synthetic shot gather meant to represent a conventional, i.e. "real", surface source at station No. 6 within the recording array, producing a direct wave and a simple reflected wave from the interface in the model. Figure 1.2b shows a synthetic shot gather meant to represent a real subsurface source (e.g. microearthquake, at the red dot) at depth directly beneath station 6. The source function is represented by a Ricker wavelet in both cases. Since we will be working with auto and cross-correlations of the signals in the virtual shot gathers, the actual wavelet shape is largely irrelevant, as it will be represented by its zero phase equivalent after correlation. We defer, for the moment, the complicating issue of the microearthquake focal mechanism.

The principle arrivals in Figure 1.2b are the direct wave (*d*), the direct reflection from the interface (*rd*) and the peg-leg multiple of the reflection corresponding to the surface reflection of the direct wave (*m*). As discussed above, cross-correlation of the record of a source at station 1 with one at station 2 produces a "virtual" seismic trace that "represents" the signal at station 2 as if the source were at station 1, with the same spectral content as the real source but with zero phase spectrum. Figure 1.2c, is the virtual shot gather computed by cross-correlating the trace of the single microearthquake recording at station 6 with itself and with the traces for the same event recorded at all the other stations. There are three distinct arrivals on the virtual shot gather. The strongest wave marks energy propagating directly from the virtual shot location (marked as a red flag in the figure) and is the re-

datumed direct wave (*dv*) of the "real" microearthquake recordings. Unlike the real direct wave (d in Figure 1.2a) which has a linear travel time behavior (as expected for a constant velocity material), the virtual direct wave (*dv*) is curved. The subsequent arrivals on the virtual shot gather represent the "secondary" cross correlation of arrivals associated with path *x* and *y1* and path *x* and *y2*, respectively, in Figure 1.3, followed by the virtual reflection (*rv*). The virtual reflection mimicking a surface source (*rv*) arises from cross-correlating the direct wave with the peg-leg multiple corresponding to the surface reflection of the direct wave. Note that other combinations of arrivals that are correlated together (*e.g.,* direct waves from a subsurface source with higher order surface-related multiples) may also contribute to the amplitude of the surface virtual sourced reflection (Figure 1.9, Wapenaar et al., 2010). The strongest of the virtual "arrivals" derives from correlating the direct wave with the direct reflection from the reflector (*rc*). In this treatment, *rc* along with all other energy except *rv*, are considered to be "artifacts" to be minimized by processing.

Finally, Figure 1.2d represents a stack of all the virtual gathers computed using station 6 as the virtual source for a distribution of microearthquakes in the subsurface as shown. Stacking tends to cancel the energy corresponding to the artifacts discussed above, while enhancing the amplitude of the energy associated with direct wave and the surface-related multiple (e.g. case 1 in Figure 1.3). In the parlance of interferometry, energy corresponding to case 1 in Figure 1.3 corresponds to a stationary phase for the direct wave (*dv*) and the surface reflection of the direct wave (*m*) (Snieder, 2007; Schuster, 2009). The power of this approach is that it is completely independent of the time of the event, and only weakly depending up its position, as will be discussed below. Thus, unlike more conventional approaches (*e.g.,* VSP; Quiros et al., 2015) the success of this imaging technique does not strongly depend upon the precision of origin times and locations of the sources.

The effectiveness of stacking multiple events to enhance the stationary phase is dependent upon the number and distribution of sources available. In the ideal "ambient noise" case, a large number of randomly distributed sources should yield satisfactory results by brute addition of all virtual gathers. This is equivalent to transforming a VSP to a SSP as described by Schuster, (2009). When the source distribution falls short of this ideal, artifacts (*e.g.,* the energy corresponding to other event correlations) can be introduced. Note the non-causal energy arriving "before" the direct wave, labeled *nc* in Figure 1.2d. Here we show how a finite suite of sources can be sorted and moveout corrected to achieve signal to noise enhancement while minimizing such artifacts for a spatially limited set of sources.

In Figure 1.4a, a virtual reflection from a virtual surface source shot gather is compared to a reflection from a "real" surface source at the same location as the virtual source. Note that these two arrivals are coincident out to a substantial source receiver offset (Fresnel zone), beyond which the two curves diverge. In Figure 1.4b a conventional, surface source normal moveout correction (NMO) is applied to both curves. As the result, the energy of both real and virtual reflections are aligned at out to much larger offsets than that represented by the Fresnel zone. If the offset between a source epicenter and a virtual source gets too large, then acausal virtual reflections will be manifested in the record. For example, the apparent travel times for an acausal event in Figure 1.2e appear earlier than the minimum physical travel time for the reflection (i.e. 2 seconds). This is because the direct arrivals from a source will start to take longer paths than the peg-leg multiple corresponding to the surface reflection of the direct wave.

As shown in Figure 1.4c, conventional NMO correction to such non-causal energy will be completely unaligned with the signals recovered for virtual sources that are physically near the epicenter of the real source.

Thus, if the range for which the real and virtual NMO are sufficiently similar, virtual shot (or CMP) gathers can be stacked like surface source-gathers following application of conventional NMO corrections. We reiterate that the zone of signal alignment after application of the NMO is substantially larger than the Fresnel zone for a reflector at this depth (*e.g.,* Figure 1.10b, Wapenaar et al., 2010) (*i.e.,* 4-fold difference of the red and blue box in Figure 1.4).

In Figure 1.5a, three virtual shot gathers derived from stacking the appropriately correlated recordings for six subsurface sources that are distributed beneath the entire range of surface receivers are shown. In Figure 1.5b, CMP gathers corresponding to the near offset boxes shown in blue in Figure 1.5a are displayed after applying a conventional NMO correction based on the virtual source to virtual receiver offsets. In addition to the virtual reflections that occur at 2.0 second, these synthetics show various artifacts due to the cross-correlation arrival of the direct wave with the direct reflection from the reflector (*i.e.,* case 2 in Figure 1.3). Since these artifacts are not aligned within the CMP gather, they will tend to cancel during stacking. As the virtual shot locations moves laterally (*e.g.,* proceeds to the right) the "footprint" (blue box in Figure 1.5) within which virtual energy mimics surface source NMO likewise tracks along the subsurface. Summing these small offset CMP traces will result in constructing a seismic section equivalent to a surface source reflection profile (Figure 1.6). In short, if we simply window the data within the appropriate aperture, the virtual reflection energy can be stacked with traditional NMO corrections.

Figure 1.6 compares a conventional, stacked section for six surface sources (Figure 1.6a) to corresponding stacked sections derived from virtual sources. The brute force autocorrelation in Figure 1.6b shows the degraded reflector at depth with many of the artifact associated with cross correlation (*e.g.,* Figure 1.4c). As more signals comes into play from the virtual CMP gathers after NMO correction (*i.e.,*

Figure 1.6c and 1.6d), the stacking has severely attenuated those artifacts resulting in a virtual stacked image of the reflection at 2.0 second that is a close copy of that produced from the surface sources. The amplitude of the virtual reflection is largest near the center of the profile, corresponding to the fact that the CMP gathers for this section have a larger number of traces (*i.e.,* fold). The contribution of the artifacts will be correspondingly minimized when stacking a larger number of sources spanning a larger range of depths (*e.g.,* Figure 1.2d). Interestingly, the CMP profile computed with range limited stacks of virtual surface sources in Figure 1.6d shows little improvement from that of Figure 1.6c in which using full aperture from the CMP gathers. For better representation of using limited range of stacks, we tested the same order of sequence as above to a different model with more sources involved.

Figure 1.7 confirms that the process is much effective for using realistically distributed sources. The model mimics a fault zone setting with associated seismicity randomly distributed beneath the recording surface. The dipping reflectors shown in Figure 1.7 and these images are subject to the same caveats that apply to conventional CMP imaging of dipping events (*e.g.,* variation of the reflection point with offset, increasing apparent stacking velocity with dip and migration effects; Yilmaz, 2001).

For a given period wavelet at a given velocity, a maximum offset of a "footprint" can be generalized with respect to each corresponding depth of a source. As a wavelet entirely cancels if the two hyperbolas (*e.g.,* a real reflection and a virtual reflection) have discrepancy of half of a period, we can set up such a criterion and thus solve for the appropriate aperture. Here we define aperture to be an offset between the epicenter of a real source to receiver. Figure 1.8 depicts maximum offset versus depth of source for 50Hz Ricker wavelet at a given velocity (*e.g.,* 6.0 km/s). The major advantage of this plot is that it can provide a rough estimate of the "window" required for the valid correction using traditional NMO-correction as long as the epicenter of a

subsurface source is located at small offset to a virtual shot location. The time difference between the normal moveout from a source at surface and that of the virtual reflection ($t_{r,virtual}$) recovered using a subsurface source will provide the maximum offset under a certain range of time (*e.g.,* half a period for a given source spectrum). In practice one can identify the virtual source positions above the subsurface source since they correspond to the minimum travel time for the direct arrivals from each source, at least for flat layered velocity structures. Thus this approach does not require precise source location, merely identification virtual source close to the epicenter of a real source below the survey. Moreover this approach is virtually independent of the source depth, which is usually the least well determined component of a hypocentral determination subject to the caveat that epicentral position and depth are both coupled with origin times in hypocentral location algorithms. Because of the weak linkage to source depth and position, this technique can thus exploit subsurface sources too small for accurate location determinations.

However treating the virtual reflection as coming from the common midpoint between virtual source and receiver is at best an approximation. In actual fact, the virtual reflection geometry entails a lateral shift of reflection location as well as the time shift inherent in the NMO correction.

More precise positioning of virtual reflection energy in travel time and space does require knowledge of source location and time. Here we modify the surface source NMO correction to more accurately account for the apparent NMO of a virtual source computed from a real subsurface source. In other words, if the location of the subsurface source is known, then a virtual NMO correction can be applied to the virtual reflection so that it stacks coherently out to much larger virtual source to virtual receiver offsets than allowed by the brute application of a conventional surface source NMO as described above. As illustrated in Figure 1.9, the travel time for the virtual

reflection is as follows:

$$t_{r,virtual} = travel\ time\ of\ path\ y2 - travel\ time\ of\ path\ x$$
$$= \frac{1}{v_0}(\sqrt{a^2 + b^2} - \sqrt{x_0^2 + d_0^2}\ ) \quad (1.1)$$

where v_0 is the velocity of a layer, t_0, two-way travel time from zero-offset, d_0, source depth, x_0, lateral offset of the virtual shot versus the source and $a = t_0 \times v_0 + d_0$, $b = x + x_0$ (Figure 1.9a).

We approach this problem using common receiver gathers instead of common shot gathers since the virtual reflection arrivals in the common virtual receiver gather represents energy recovered from a single CRP from subsurface for all virtual sources. Moreover the virtual sources involved do not, in general, correspond to the physical locations of real recording stations. Figure 1.10a shows a virtual receiver gather at station 6 acquired from all of the virtual source gathers computed by cross-correlation. In other words, each reflection of the peg-leg multiple recorded by a given receiver is correlated with the direct arrivals recorded from all the real recording stations. In this case, the virtual reflections in the virtual source gathers (*e.g.,* Figure 1.9a) no longer sample the same CMP as for the conventional surface source NMO correction (Figure 1.9b). Figure 1.10c shows a representative CRP gather after applying both time and space shifts associated with the true virtual reflection geometry. These shifts are analogous with those associated with VSP processing (*e.g.,* Hardage, 2000, Quiros et al., 2015). The resulting stack recovers the target reflection with amplitudes that increase (center) in proportion to the number of earthquakes available for imaging. In addition to correcting the virtual reflection to the 2.0 second t_0 time, this process results in aligning the artifacts associated with cross-correlation for a single real source (*e.g.,* Figure 1.10c).

$$t_{r,aritifact} = travel\ time\ of\ path\ y1 - travel\ time\ of\ path\ x$$

$$= \frac{1}{v_0}(\sqrt{a'^2 + b^2} - \sqrt{x_0^2 + d_0^2}) \quad (1.2)$$

where $a' = t_0 \times v_0 - d_0$. The above equation defines the travel time for the reflection of the down going wave from the source, and it resembles equation 1.1 except for a' subtraction of source depth applies instead of an addition. Thus if the offset between a real source and a virtual receiver (*e.g.,* value *b* in equation 1.1 and 1.2) is effectively larger than a or a', the curvature for $t_{r,virtual}$ and $t_{r,aritifact}$ will be approximately identical so that the virtual NMO correction using equation 1.1 also align the artifact. Although this artifact will be degraded by stacking of virtual source gathers from earthquakes from different locations (*e.g.,* Figure 1.10d) in our treatment, such energy could also be treated as an alternative reflection signal for imaging (King and Curtis, 2012).

To summarize, synthetics models make clear that virtual reflection imaging of subsurface structure is feasible even for a subsurface distribution of sources that is inadequate in number or distribution for conventional ambient noise analysis.

More precise

1.3.2 The Virginia experiment

To explore the effectiveness of this approach with real data, we examined aftershock recordings made following the magnitude of 5.8 Virginia earthquake in 2011 that were acquired using single component (Texan) recorders equipped with 4.5 Hz vertical geophones (Davenport et al, 2015). The Virginia experiment included 103 Texan recorders deployed along 5 quasi-linear array segments at 200m station spacing in the region of the aftershock events (Figure 1.11a). In this study, seismic recordings of 50 aftershocks of magnitude between M_L -1.5 and M_L -2 (Davenport et al, 2015)

were visually identified and extracted for imaging via interferometry. Although these events were recorded by various array segments, attention here is focused on those recorded by the highlighted stations in Figure 1.11a, for the geometric reasons made clear by the modeling previously described. These events lie beneath and laterally near the recording array used for imaging, two conditions identified as favorable for signal stacking and imaging.

To start with, a brute force autocorrelation section was created using 50 aftershock recordings (Figure 1.12a). This autocorrelation section mimics a vertically stacked, single fold zero source-receiver offset survey. Ideally, autocorrelating signals with local earthquakes will work the greatest if those sources are distributed directly beneath every station. The resulting reflection section shows some coherency in the same depth range as a nearby conventional surface survey collected (Figure 1.12d; Pratt et al., 2015), but this coherency is relatively localized and scattered. The autocorrelation provides little indication of the southeast dipping thrust structures inferred from the conventional deep seismic line (Figure 1.12d). However, it should be noted that this conventional seismic survey is located approximately 10 km southwest of the virtual reflection seismic images presented, so that a one-to-one correlation of reflection patterns is not necessarily expected.

Figure 1.12b shows an attempt to stack virtual CMP gathers using the aftershock recordings with conventional NMO corrections to date within the aperture limits described earlier. Coherent bands of southeast dipping reflection energy are evident at travel times of 0.5 to 3.5 sec (ca 1.5 to 11.5 km depth). This band is very similar to the southeast dipping band of energy on the conventional reflection image, albeit at slightly greater travel times (depth).

Figure 1.12c shows a stacked reflection image using our full aperture virtual NMO correction, but retaining the conventional binning of the CMP stack. At the

primary depth of interest here (6-12 km), the lateral shift of the CRP from the CMP is smaller than the normal bin size corresponding to the conventional CMP. The resulting section in Figure 1.12c shows somewhat more pervasive coherency than Figure 1.12b, but reflection amplitudes are much more subdued. Due to larger source to receiver offsets involved, the CRP locations show significantly more lateral scatter than the CMP positions (Figure 1.11b). If the reflecting interfaces themselves have substantial 3D variation in geometry, this increased scatter would expect to degrade the CRP stack more severely than the CMP stack. Given the three dimensional nature of both source and structure, effective CRP stacking may require true 2D receiver arrays and associated 3D subsurface.

Application of FX deconvolution to enhance linearity in all three images tends to bring out a subhorizontal coherency of all three sections at a time similar to that of subhorizontal coherency in the surface seismic survey. Although the coherent "stacked" reflections on these images are less than impressive, the same could be said for the reflections on the original deep seismic stacks using conventional surface sources (Pratt et al, 1988). Also, note that there is a substantial difference in CMP spacing (*i.e.,* 33m vs. 200m) between these virtual reflection sections versus the conventional profile (Figure 1.12 and Figure 1.13).

Possible complications not addressed here which could have affected the final images include: a) S wave energy, b) variations in microearthquake focal mechanisms which could result in polarity changes that degrade the stack, c) lateral variations in subsurface velocity structure that would distort the presumed hyperbolic travel times, and d) static time shifts due to variations in the near surface. Although S wave energy undoubtedly contaminates any cross-correlations sums it should destructively interfere as we increase the number of aftershocks in the process. Even if such energy still remains in the stack, virtual reflection arrivals can hardly be affected because P-S time

intervals from the aftershock recordings in Virginia were less than 2 seconds. Ideally recording with 3 components would allow separation of P from S wave energy before correlation. The impact of variations in the source function should be minimal due the zero phase nature of the cross-correlated waveforms. Certainly, polarity reversals across focal planes for either the direct or various reflected signals within the array could be detrimental. However, here the direct arrivals of the selected microearthquakes show the same polarity across the highlighted stations (Figure 1.11) suggesting polarity changes due to focal mechanisms are not a serious issue here. Velocity analysis of the Virginia data (Davenport et al, 2015) indicates an almost homogeneous upper crust within the array, which rules out lateral velocity variations as a problem. Static shifts could be an issue, given the saprolitic nature of the near surface. There are no near-offset, surface source measurements to provide traditional refraction statics corrections. Attempts to recover useful statics from cross-correlation techniques were unsuccessful. In addition, elevation statics were negligible considering the minimal relief within the Virginia array.

These results, and the modeling behind them, suggest that this methodology would be more effective with recording by true 2D surface arrays (and thus stacking within 2D spatial windows of stationary phase and producing true 3D imagery), by using 3 component sensors to separate P and S wave energy and, of course, by using a much larger number of sources (Majer et al., 2007). Most aftershock sequences involved hundreds, if not thousands of sources.

1.3.3 Advantages

We have argued above that an advantage of this approach over conventional reflection surveys is the absence of the need for expensive controlled sources, assuming an adequate number of natural sources are available. Here we point out another advantage of this technique over other commonly used seismic methods using

natural sources.

While recent developments in imaging with the teleseismic sources using techniques such as receiver functions (Bostock et al., 2001; Poppeliers and Pavlis, 2003) as well as interferometry (e.g., Ruigrok et al., 2008; Ruigrok and Wapenaar, 2012; Lin et al., 2013) of global phases have led to marked advances at wavelengths of a couple km to tens of km, the teleseismic wavefield is fundamentally limited by its low frequency content (Figure 1.14). In contrast, peak frequencies for the local earthquake sources are many times higher than those available from teleseismic sources due to path attenuation differences. These differences map into substantial differences in resolution. This contrast is illustrated by the simple synthetic example in Figure 1.15.

Figure 1.15 compares a receiver function profile based on synthetic teleseismic Ps waves with that of a synthetic aperture-limited CMP stack derived by applying the methods described above to local earthquakes under the recording array for a simple subducting slab model. Whereas both methods reveal the presence of the widely spaced discontinuities, only the virtual reflection profile distinguishes the thin layer at the top of the synthetic slab. The slab imaging example briefly mentioned here will be discussed in more detail later in Chapter 4.

Certainly the crustal structures that are essential to understanding the tectonics of the Virginia seismic zone fall well below in feasible teleseismic bandwidth, but well within the bandwidth of the aftershock sources used in the imaging reported here (*e.g.,* Figure 1.14b).

1.4 Conclusion

We here present a novel variation on body wave imaging of structures using microearthquakes (natural or induced) as subsurface sources for CRP stacked sections. It has applicability for geological and energy problems where such sources are present

in abundance. Compared with conventional surface reflection profiling, this approach removes the costly requirement of artificial sources. Unlike other imaging techniques using natural sources, the aperture limited CMP stack using conventional NMO does not require precise source locations or times as long as the sources are mainly distributed below the surveying site. It can thus exploit aftershocks too small for accurate location determination. More importantly, it can take advantage of the broader bandwidth of local natural sources, providing much higher resolution imaging of structure that passive techniques based on teleseismic sources. As an extension to the CMP approximation, a virtual NMO correction has been derived which can more effectively use the full recorded wavefield and provide more precise positioning of virtual reflection energy in space. The combination of natural sources with high resolution represents a potentially low cost approach to 3D and even 4D imaging of crustal structure in seismically active areas.

1.5 Figures

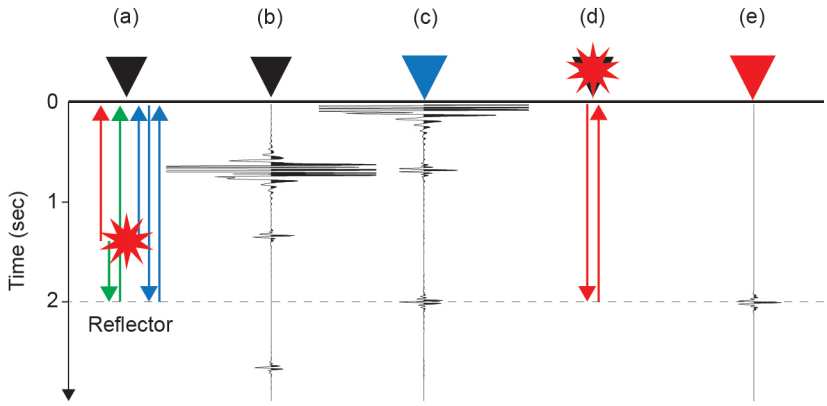

Figure 1.1: Reflection signal derived from autocorrelation of transmission (+ downgoing reflection) response of a subsurface source based on a simple velocity model of a flat layer at 6 km depth with a constant velocity of 6km/s: (a) seismic energy emitted from a subsurface source and its associated raypaths in red (direct path), green (primary reflection from the reflector), and blue (a surface-based multiple), (b) transmission response plus down-going reflection response from the subsurface source, (c) the autocorrelated trace of (b), (d) raypath for seismic energy emitted from a surface source and reflected from base of the layer, and (e) its

reflection response. Note that the autocorrelation not only recovers the virtual reflection of the energy from travelling upward from the source, it includes an "artifact" corresponding to the energy initially travelling downward before reflected from the subsurface discontinuity.

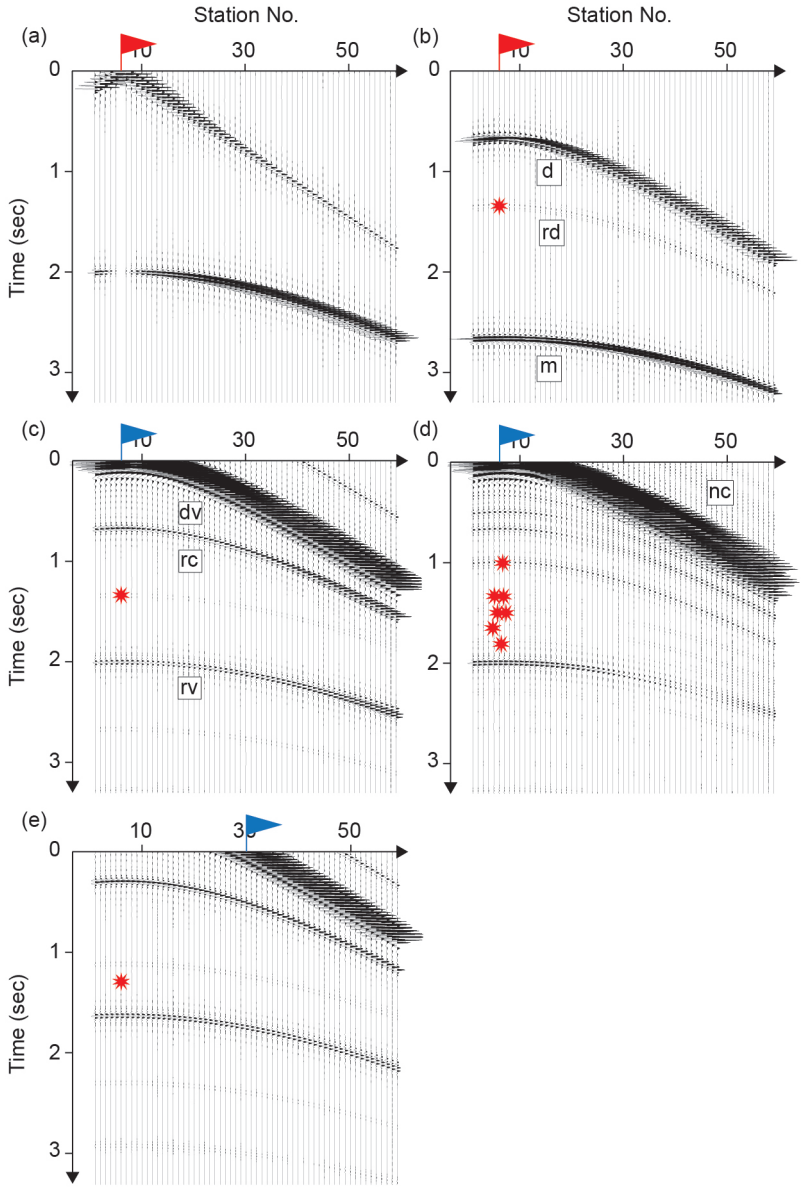

Figure 1.2: (a) Synthetic source-gather for a surface source (i.e. conventional controlled source reflection survey). (b) Synthetic source gather for an arbitrary subsurface source. (c) Virtual "surface" source gather computed by cross-correlating flagged trace in (b) with all other traces. (d) Sum of virtual "surface sources" computed from multiple arbitrary subsurface sources at red dots (e) Virtual "surface"

source gather computed by cross-correlating 30th trace (record from station 30) from (b) with all other traces. (The red and blue flag indicates real and virtual source positions respectively).

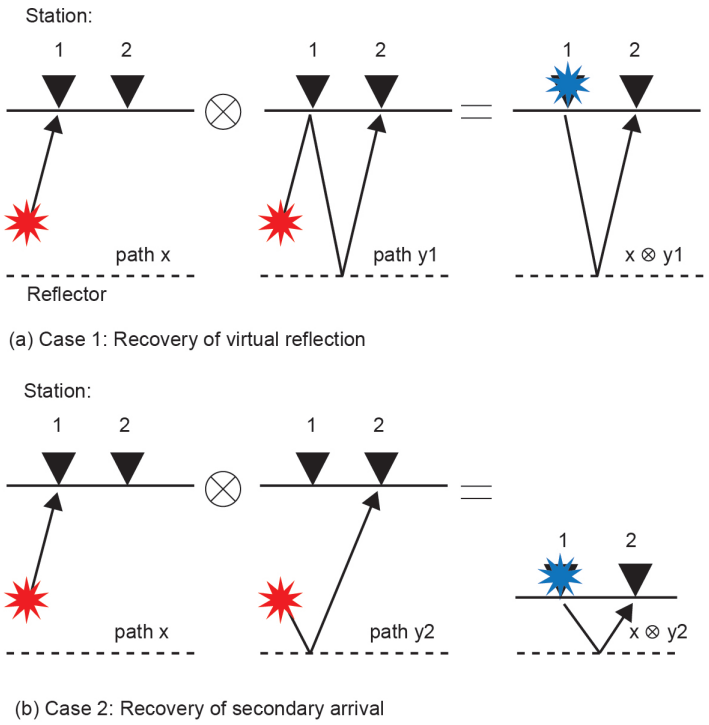

Figure 1.3: Cross-correlation arrivals in virtual shot gathers and their associated raypaths

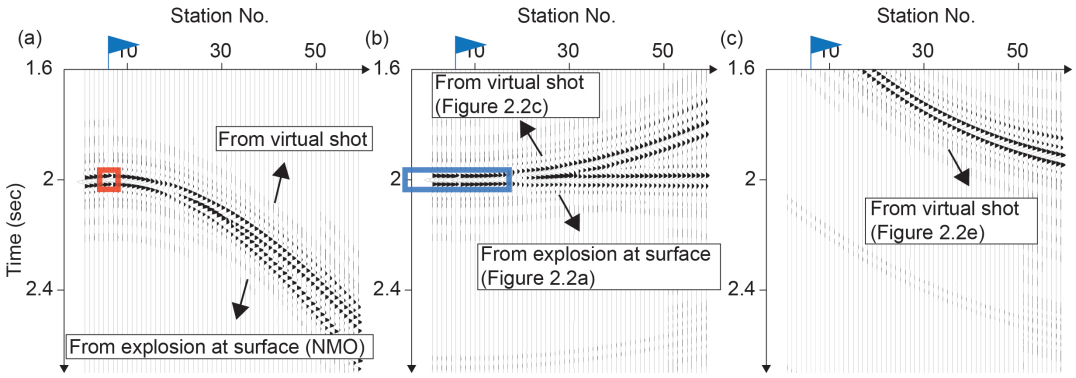

Figure 1.4: Comparison of a virtual reflection from a virtual shot gather and a real reflection from a surface source at the same location: (a) without NMO, (b) and (c) with corrections in Figure 1.4 and Figure 1.2e respectively (The red and blue box indicates the conventional Fresnel zone for a surface source reflection and the extended area of constructive interference due to NMO correction respectively).

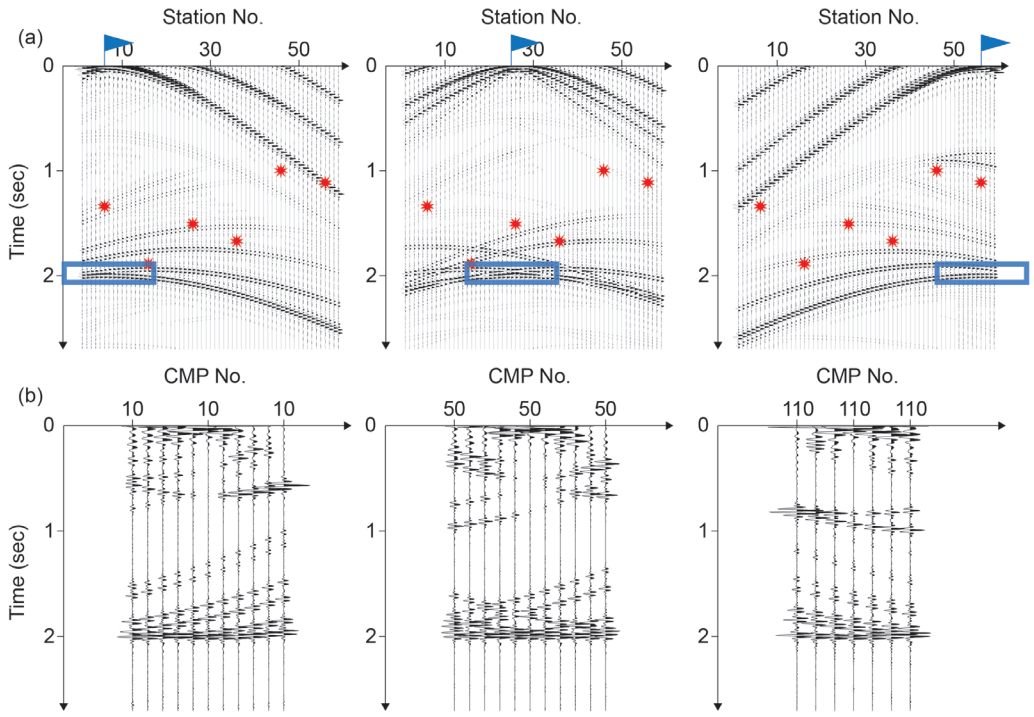

Figure 1.5: (a) Virtual shot gathers using six subsurface sources and (b) their corresponding NMO-corrected CMP gathers (The blue box on virtual shot gathers indicates the offset range at which useful signal enhancement can be achieved by simple application of a conventional surface source NMO correction). Note that the trace spacing for the CMP gathers is twice that for the corresponding virtual shot gathers.

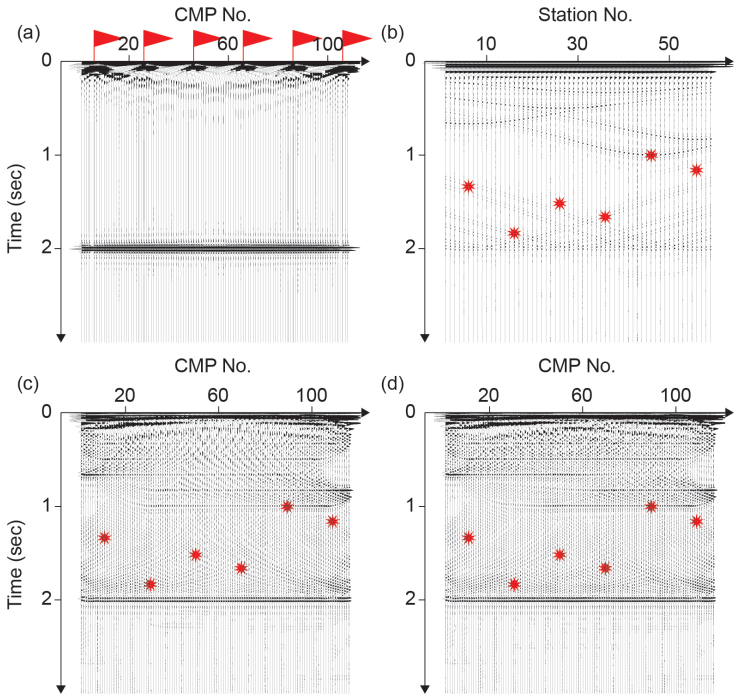

Figure 1.6: (a) A synthetic seismic section equivalent to a CMP stacked reflection profile corresponding to six surface sources compared with (b) the brute force autocorrelation, (c) the CMP profile computed with stacks of virtual surface sources derived from six subsurface sources, and (d) the CMP profile computed with range limited stacks of virtual surface sources.

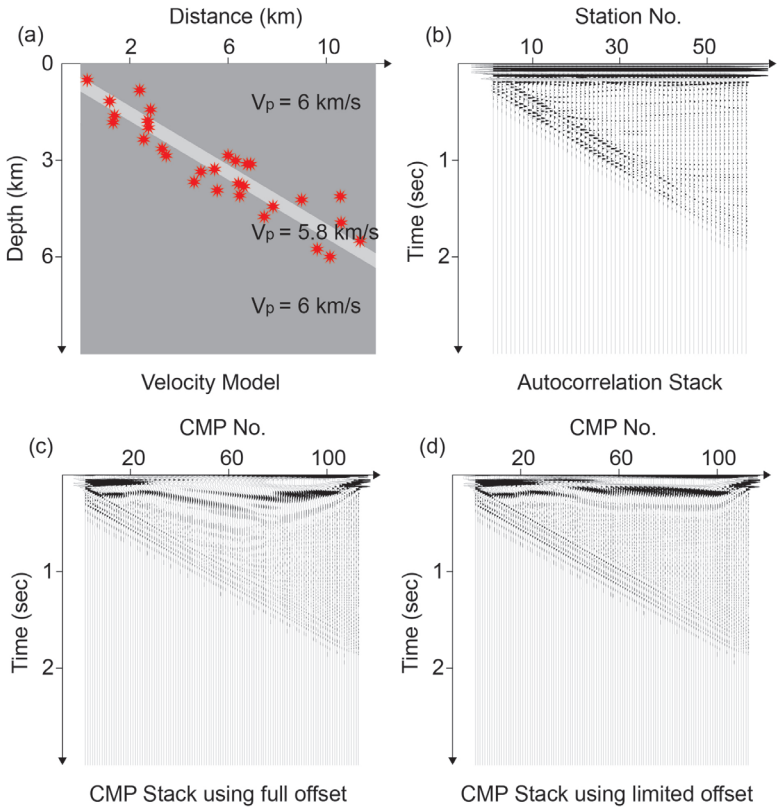

Figure 1.7: (a) Simple velocity model representing a fault zone setting with associated seismicity, (b) the brute force autocorrelation of its records, (c) the CMP profile computed with stacks of virtual surface sources derived from subsurface sources in red, and (d) the CMP profile computed with range limited stacks of virtual surface sources.

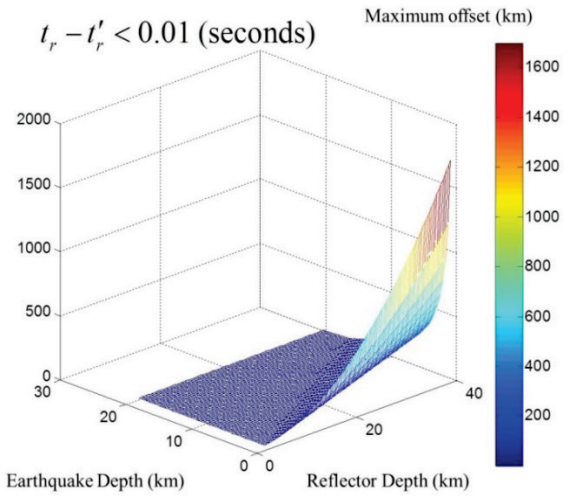

Figure 1.8: Maximum effective stacking offset (from epicenter of real source to receiver) versus depth of source for 50Hz Ricker wavelet and a medium velocity of 6.0 km/s

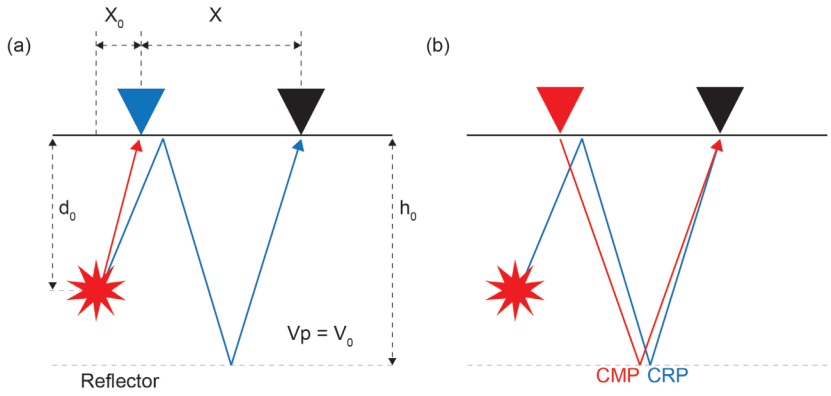

Figure 1.9: Associated raypaths for virtual reflection between two adjacent receivers (The station in blue indicates virtual source; the red and blue lines indicate path *x* and path *y2* from case2 in Figure 1.3 and the reconstructed path representing their travel time difference, respectively) (a) and spatial offset in imaging position with a surface source vs. a subsurface source (b). Only in the special case (corresponding to the stationary phase sensu stricto) where the angle of incidence of the upgoing wave at the first station is equal to the angle of reflection at the subsurface interface corresponding the offset between the two stations does the CMP = CRP.

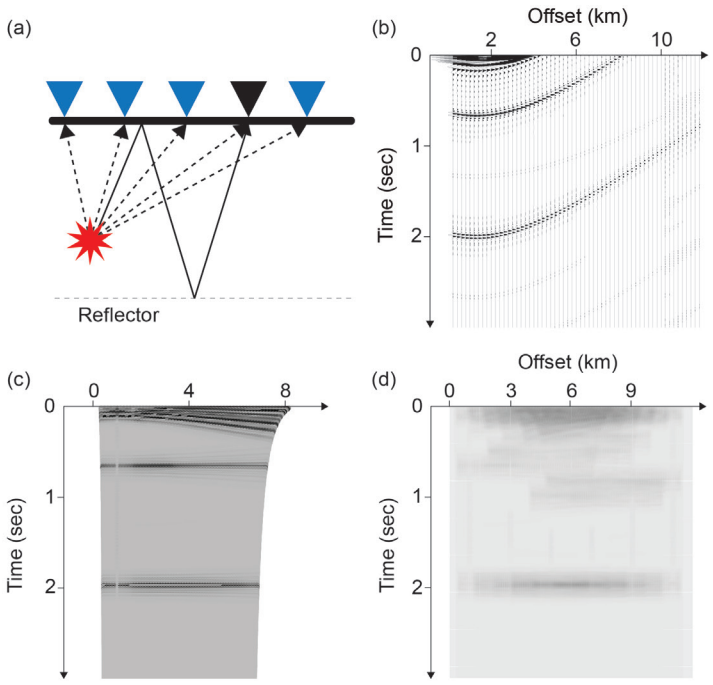

Figure 1.10: Associated raypaths (a) for virtual receiver gather (b) and virtual moveout corrected CRP gather (raster display) from all of the stations of the reflection profile (c). (d) CRP visual stacked image from six subsurface sources using virtual moveout correction (each sample has specific transparency level (*e.g.,* 1/6 for 6 subsurface sources) for the visual stack)

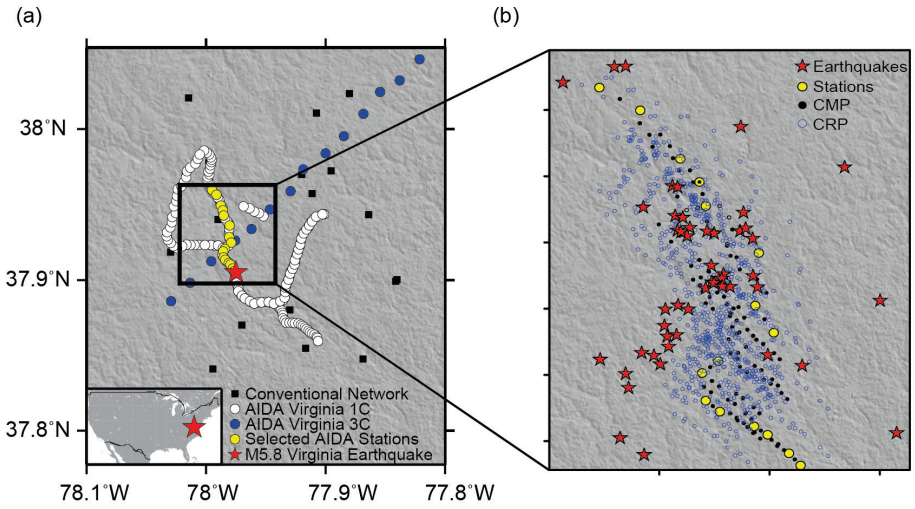

Figure 1.11: (a) Dense receiver array deployed in Virginia aftershock experiment (Davenport et al., 2015) and (b) the epicenter of CMP (green) and CRP (blue) constructed from the stations within the highlighted area in (a).

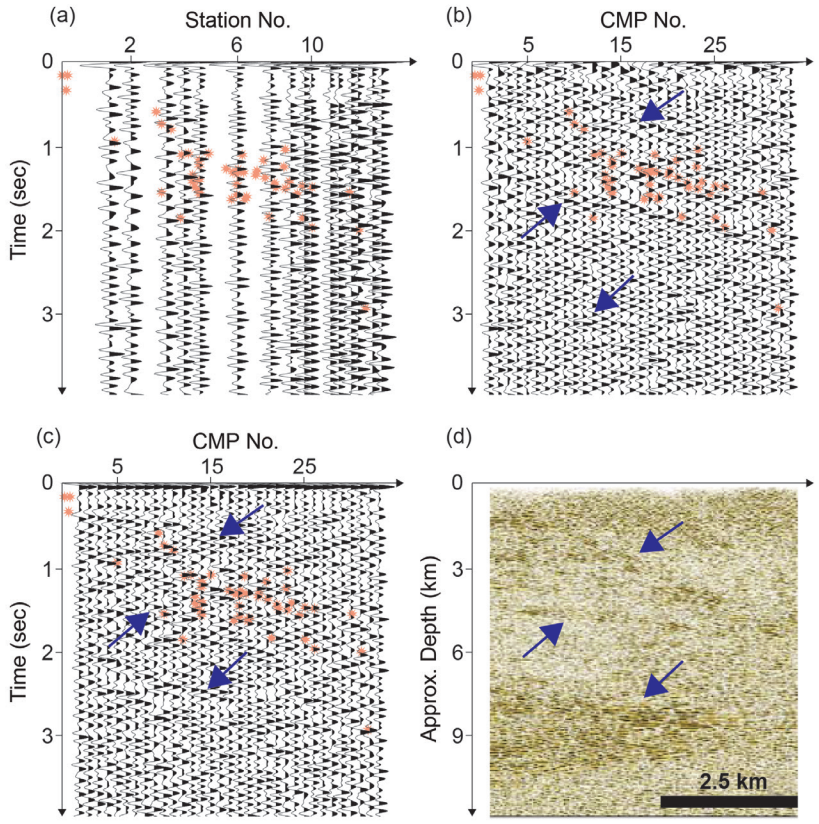

Figure 1.12: (a) A seismic section equivalent to a brute force autocorrelation, (b) a CMP stacked virtual reflection profile, and (c) a CRP stack using virtual normal moveout correction from Virginia experiment compared with (d) the crustal reflection surveying by Pratt et al., 2015 (red dots denote the selected microearthquakes). Blue arrows indicate southeast dipping structures inferred from (d). Note that the three seismic sections have received identical amplitude treatments. Northwest is to the left, southeast is to the right, for each section.

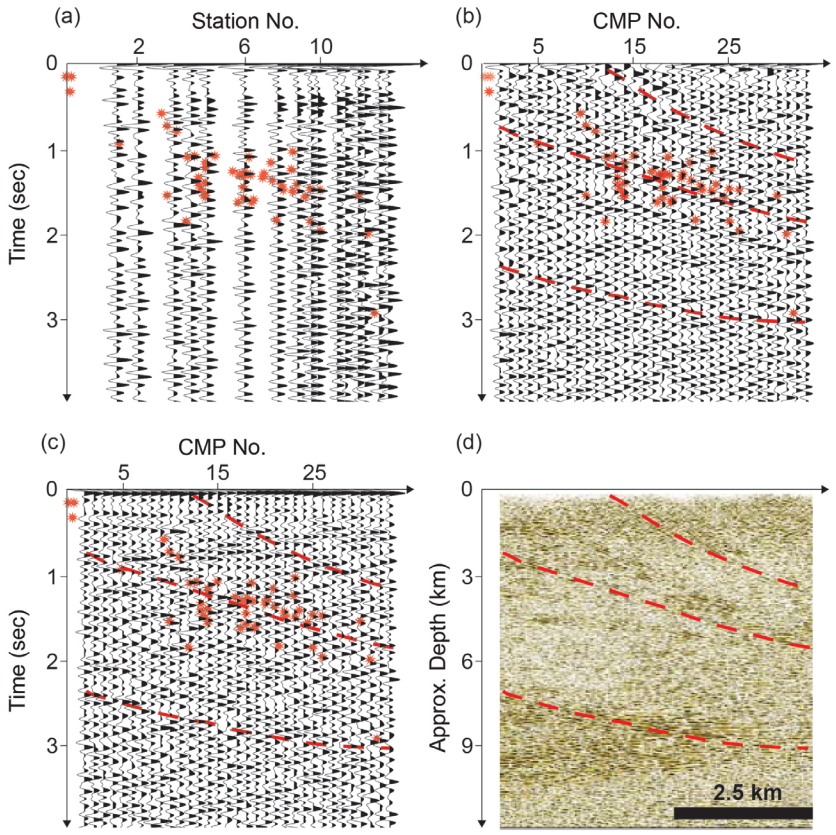

Figure 1.13: Stacked virtual reflection sections from Figure 1.12 enhanced using FX-deconvolution.

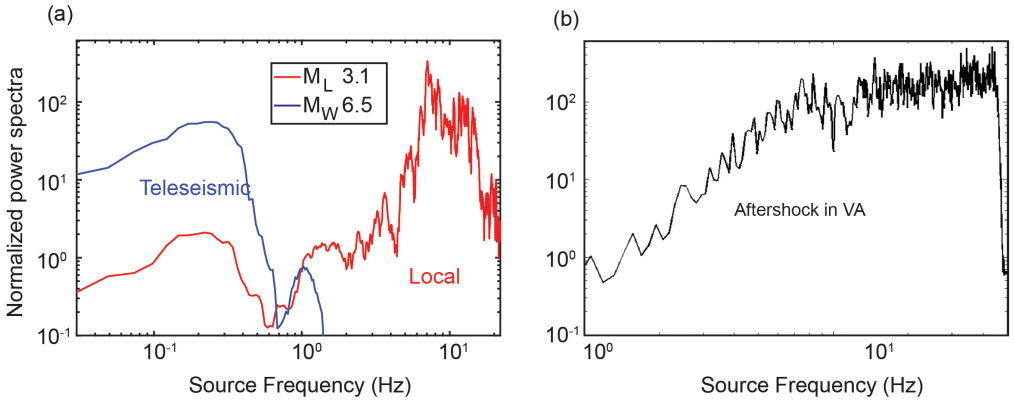

Figure 1.14: (a) Velocity power spectra for P waves from a local and teleseismic earthquake normalized to background noise levels, recorded at MOOS station HOPJ on the Kenai Peninsula. (b) Velocity power spectra representing Virginia experiment recordings.

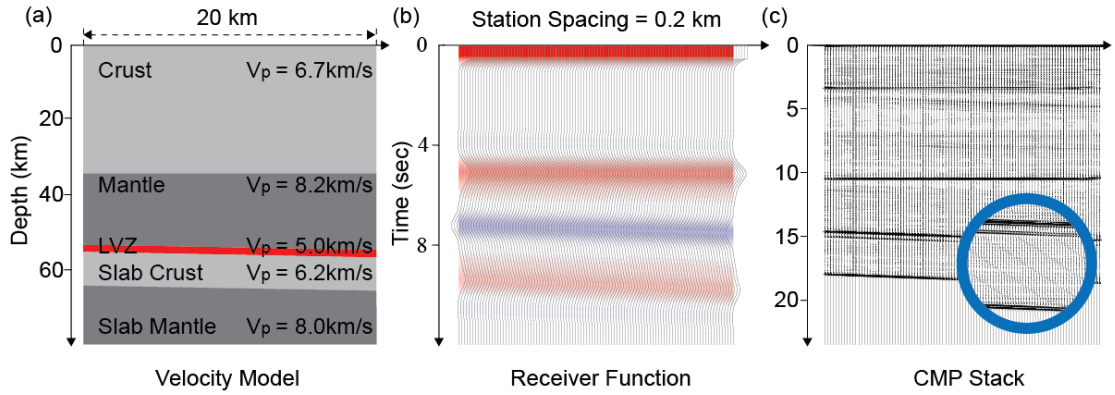

Figure 1.15: (a) Simple velocity model representing a portion of a subducting slab with a 1 km thick low-velocity layer (blue), (b) synthetic receiver functions derived from teleseismic Ps waves (Gaussian-filtered at 0.5 Hz) corresponding to the velocity model and (c) synthetic CMP stacked depth section computed via interferometry of high frequency (ca 10 Hz) from local sources (50 earthquakes). Inset shows a detail of the thin low velocity zone (the red zone in 1.15a) which is clear in the virtual stack but effectively invisible in the receiver function profile.

REFERENCES

Bostock, M. G., S. Rondenay, and J. Shragge, 2001, Multiparameter two-dimensional inversion of scattered teleseismic body waves; 1, Theory for oblique incidence, Journal of Geophysical Research, **106**, 30771-30782.

Chaput, J. A., and M. G. Bostock, 2007, Seismic Interferometry Using Non-Volcanic Tremor in Cascadia: Geophysical Research Letters **34**, L07304.

Claerbout, J, 1968, Synthesis of a Layered Medium from Its Acoustic Transmission Response: GEOPHYSICS **33**, 264–269.

Davenport, K. K., J. A. Hole, D. A. Quiros, L. D. Brown, M. C. Chapman, L. Han, and W. D. Mooney, 2015, Aftershock Imaging Using a Dense Seismometer Array (AIDA) after the 2011 Mineral, Virginia, Earthquake: Geological Society of America Special Papers **509**, 273–283.

Draganov, D., X. Campman, J. Thorbecke, A. Verdel, and K. Wapenaar, 2009, Reflection Images from Ambient Seismic Noise: Geophysics **74**, A63–67.

Hardage, B.A., 2000, Vertical Seismic Profiling: Principles, Pergamon.

Ito, Y. and K. Shiomi, 2012, Seismic scatterers within subducting slab revealed from ambient noise autocorrelation, Geophys. Res. Letters, **39**, doi:

10.1029/2012GL053321.

Lin, F. C., V. C. Tsai, B. Schmandt, Z. Duputel, and Z. Zhan, 2013, Extracting Seismic Core Phases with Array Interferometry: Geophysical Research Letters **40**, 1049–1053.

Majer, E. L., R. Baria, M. Stark, S. Oates, J. Bommer, B. Smith, and H. Asanuma, 2007, Induced Seismicity Associated with Enhanced Geothermal Systems: Geothermics **36**, 185–222.

Margrave, G. F., 2001, Numerical methods of exploration seismology with algorithms in Matlab: The University of Calgary Publ.

Poppeliers, C., and G. L. Pavlis, 2003, Three-dimensional, prestack, plane wave migration of teleseismic P-to-S converted phases: 2. Stacking multiple events, Journal of Geophysical Research, **108**, No. B5, 2267.

Pratt, T. L., C. Çoruh, J. K. Costain, and L. Glover, 1988, A Geophysical Study of the Earth's Crust in Central Virginia: Implications for Appalachian Crustal Structure: Journal of Geophysical Research: Solid Earth **93**, 6649–6667.

Pratt, T. L., J. W. Horton, D. B. Spears, A. K. Gilmer, and D. E. McNamara, 2015, The 2011 Virginia Mw 5.8 Earthquake: Insights from Seismic Reflection Imaging into the Influence of Older Structures on Eastern U.S. Seismicity: Geological Society of America Special Papers **509**, 285–294.

Quiros, D. A., Cabolova A., Brown L. D., Chen, C., Ebel, J. E., Starr, J., 2015, Aftershock Imaging with Dense Arrays (AIDA) Following the Mw 4.0 Waterboro Earthquake of 16 October 2012 Maine, U.S.A. Seismol Res Lett **86**, 1032-1039.

Rickett, J., and J. Claerbout, 1999, Acoustic Daylight Imaging via Spectral Factorization: Helioseismology and Reservoir Monitoring: The Leading Edge **18**, 957-960.

Snieder, R., 2007, Extracting the Green's function of attenuating heterogeneous acoustic media from uncorrelated waves: The Journal of the Acoustical Society of America 121, 2637-2643.

Ruigrok, E., Draganov, D., Wapenaar, K., 2008, Global-scale seismic interferometry: theory and numerical examples: Geophysical Prospecting **56**, 395-417.

Ruigrok, E., and Wapenaar, K., 2012, Global-phase seismic interferometry unveils P-wave reflectivity below the Himalayas and Tibet: Geophysical Research Letters **39**, L11303.

Ryberg, T, 2011, Body Wave Observations from Cross-Correlations of Ambient Seismic Noise: A Case Study from the Karoo, RSA: Geophysical Research Letters **38**, L13311.

Schuster, G. T., 2009, Seismic Interferometry: Cambridge University Press.

Shapiro, N. M., M. Campillo, L. Stehly, and M. H. Ritzwoller, 2005, High-Resolution Surface-Wave Tomography from Ambient Seismic Noise: Science **307**, 1615–1618.

Vidal, C.A., D. Dragonov, J. van der Neut, G. Drijkoningen, and K. Wapenaar, 2014, Retrieval of reflections from ambient noise using illumination diagnosis, Geophys.J. Int., **198**, 1572-1584.

Wapenaar, K., D. Draganov, R. Snieder, X. Campman, and A. Verdel, 2010, Tutorial on Seismic Interferometry: Part 1 — Basic Principles and Applications: GEOPHYSICS **75**, 195–209.

Xu, Z., C. Juhlin, O. Gudmundsson, F. Zhang, C. Yang, A. Kashubin, and S. Lüth, 2012, Reconstruction of Subsurface Structure from Ambient Seismic Noise: An Example from Ketzin, Germany: Geophysical Journal International **189**, 1085–1102.

Yilmaz, Ö., 2001, Seismic Data Analysis: Society of Exploration Geophysicists.

Zhan, Z., S. Ni, D. V. Helmberger, and R. W. Clayton, 2010, Retrieval of Moho-Reflected Shear Wave Arrivals from Ambient Seismic Noise: Geophysical Journal International **182**, 408–20.

CHAPTER 2

MAGMA REFLECTION IMAGING IN KRAFLA, ICELAND, USING MICROEARTHQUAKE SOURCES

2.1 Abstract

The details of magma plumbing beneath active volcanoes remain a major challenge in geochemistry, geophysics and volcanic hazard evaluation. Here we apply a relatively novel variation of seismic interferometry, which we call Virtual Reflection Seismic Profiling (VRSP), to produce a high-resolution image of a known crustal magma body. The technique takes advantage of recent advances in both seismic instrumentation (dense arrays) and seismic analysis (seismic interferometry). We have applied this technique to data recently acquired at an iconic volcanic system, Krafla, which lies on the mid-Atlantic ridge as exposed in northern Iceland. What make this particular site exceptional are encounters with rhyolitic magma in two drillholes, K-39 and Iceland Deep Drilling Project-1 (IDDP-1). These known magma bodies represent a unique calibration opportunity for surface geophysical measurements of magma distribution at depth. In this study, we produced a stacked, seismic reflection section by applying common depth point processing techniques to virtual shot gathers derived from interferometry of P waves from microearthquakes generated by tectonic, magmatic and/or geothermal activity. We observe a strong, coherent reflection on the seismic section at a travel time corresponding to the depth at which magma was encountered in the IDDP-1 wellbore. We interpret this reflection to be from magma or magma-related fluids. Additional coherent reflections may correspond to other components of the magma plumbing beneath Krafla. These results represent a promising new technique for structural imaging with natural sources that can be applied to a wide array of geologic and energy problems that involve natural or induced seismic clusters.

The material in Chapter 2 has been published under Kim et al., Magma reflection imaging in Krafla, Iceland, using microearthquake sources. *Journal of Geophysical Research: Solid Earth (2017)* **122**, 5228-5242

2.2 Introduction

The distribution and movement of magma in the earth's crust has been a critical concern of geochemical and geophysical investigations for much of the past century (*e.g.,* Spera, 1980; Crisp, 1984; Corry, 1988; Glazner and Ussler III, 1988; Emerman and Marrett, 1990; Ishihara, 1990; Parson et al., 1992; Gudmundsson, 2000; Polteau et al., 2008). Fundamental and persistent questions related to magma plumbing include the relative importance of magma chambers vs sill or dyke complexes, the role of density and viscosity in the transport of magma in the crust, the relative mixing of original magma with host rocks during ascent, and ultimately, the recognition of precursors to major eruptive events (*e.g.,* Voight and Cornelius, 199l; Scarpa, 2001).

Some of the better known attempts at magma imaging with seismic methods include passive tomographic studies (Lees, 2009) to delineate the magma chambers beneath Yellowstone (*e.g.,* Iyer et al., 1981; Benz and Smith, 1984; Huang et al., 2015) , efforts to map the Socorro magma body under central New Mexico using reflected body waves from microearthquake sources (*e.g.,* Sanford and Long, 1965; Sanford et al., 1973; Sanford et al., 1977) , and similar work in Japan to associate magma with reflected shear waves on microearthquake recordings (*e.g.,* Matsumoto and Hasegawa, 1996). There are also now a number of examples of magma bodies being detected and/or mapped by multichannel controlled-source surveys, beginning with COCORP's profiling of the Socorro Magma Body in 1976 (Brown et al; 1979; Brocher, 1981) and detection of a similar sill-like body beneath Death Valley (De Voogd et al., 1986). Another prominent example of magma bodies being mapped by surface reflection surveys are the INDEPTH surveys on the southern Tibetan Plateau (Brown et al., 1996; Makovsky et al., 1996), which have been cited to support the role of partial melting in plateau uplift (Nelson et al., 1976). Active seismic reflection

mapping of magma chambers, including 3D, has been achieved beneath mid-ocean ridges by marine multichannel profiling (*e.g.,* Mutter et al., 1988; Kent et al., 2000). New passive techniques, such as receiver functions, have also reported the presence of molten material at intra-crustal depths, including independent detection of the Socorro Magma Body (Sheetz and Schlue, 1992) and perhaps most notably the mapping of the Altiplano-Puna magma body beneath the central Andes (Zandt et al., 2003; Ward et al., 2014). In many cases, the interpretation of magma from the seismic results has been strongly bolstered by complementary geophysical measurements, most notably magnetotelluric (*e.g.,* Wei et al., 2001).

The aforementioned diverse seismological results represent independent but complementary means of detecting magma at crustal depths, each with its strengths and limitations. For example, receiver functions can probe to sub-lithospheric depths, but the bandwidth typically available from teleseismic sources severely limits resolution within the crust (Cassidy, 1992) and attenuation/scattering in volcanic areas often hampers the penetration achievable with higher-resolution active surface seismic surveys (*e.g.,* Ziolkowski et al., 2003). Moreover the source costs associated with conventional multichannel seismic reflection surveys on land is often prohibitive, especially in rugged terrain.

Subsurface imaging by processing the ambient noise field with a technique known as seismic interferometry has become a widely used and powerful tool for crustal-scale velocity imaging using surface wave tomography (*e.g.,* Shapiro et al., 2005; Lin et al., 2008). However, the effectiveness of interferometry in extracting useful body-wave information from ambient noise has been more challenging. Roux et al. (2005) documented the presence of P waves in their analysis of ambient noise in southern California. Draganov et al. (2009; 2013) describes efforts related to oil and gas exploration, while Ryberg (2011) reports recovery of both wide-angle reflections

and refractions that correlate with their counterparts from explosive sources in a regional seismic survey. Yu and Schuster (2001) use seismic noise generated by drilling operation to recover the reflectivity distribution beneath the survey. At a larger scale, seismic interferometry of ambient noise has been used to recover Moho reflections (*e.g.,* Tibuleac and Seggern, 2012; Gorbatov et al., 2013), reflections form the lithosphere-asthenosphere boundary (Kennett, 2015) and prominent core phases (Lin et al., 2013a). Although most interferometric analyses of both surface and body waves attempt to extract useful information from unknown, presumably random noise sources, of particular relevance to this study is the use of selected, known sources. This application of interferometry has found numerous applications in the exploration industry (*e.g.,* Wapenaar et al., 2008; Schuster, 2009), and has recently found application to earthquake sources. For example, Ruigrok and Waapenaar (2012) used interferometry of global phases from appropriately located teleseismic events to image lithospheric structure beneath southern Tibet. Nakata et al. (2014) retrieved body waves in southwestern Wyoming using multidimensional deconvolution of recordings of local and regional earthquakes. Nishitsuji et al. (2016) has produced crustal-scale reflection imagery using interferometry of the P coda from regional earthquakes in the southern Andes. Here, we apply a similar approach to high-resolution imaging of crustal structure using local microearthquakes generated by geothermal activity in Iceland.

In this study, seismic interferometry is applied to recordings of local microseismic events ($M_L < 2$) as energy sources. Unlike true "ambient noise" treatments, in which a wide and quasi random distribution of a large number of sources at unknown locations is assumed, our approach is to incorporate selected events (microearthquakes) and redatum them in the manner described by Schuster (2009) as VSP to SSP. We will refer here to this imaging technique as Virtual

Reflection Seismic Profiling (VRSP). VRSP focuses on using the surface ghost reflection (free-surface multiple) associated with up-going energy from a subsurface source whose epicenter is relatively near to virtual surface source locations to produce a stacked seismic image comparable to what one would get using real surface sources at those same virtual locations (*e.g.,* Schuster, 2009).

2.3 Study area

Iceland has long served as perhaps the world's most iconic exposure of mid-ocean ridge processes by virtue of an underlying mantle plume, or hot spot (Gudmundsson, 2000). While much attention was given to the Reykjanes peninsula in southwestern Iceland, where the modern plate boundary comes ashore, volcanic systems throughout Iceland have been of intense scientific and societal concern (e.g. Gertisser, 2010). The Krafla volcanic-geothermal system in particular (Figure 2.1) has been one of the most studied of the Icelandic magma system due to recurring fissure swarm eruptions over the past centuries (*e.g.,* Tryggvason, 1984; Einarsson, 1991; Saemundsson, 1991; Harris et al., 2000; Buck et al., 2006). A simple cross-sectional cartoon of the Krafla caldera is shown in Figure 2.2.

Various seismic measurements have suggested the existence of a magma chamber less than 4 km thick beneath Krafla, with horizontal dimensions of 2 x 7 km and a top ranging from 3 to 7 km depth (Einarsson, 1978; Brandsdóttir and Menke, 1992; Arnott and Foulger, 1994; Brandsdóttir et al., 1997; Darbyshire et al., 2000). Recent 3D tomographic images, generated by inverting both artificial and natural sources, also indicate velocity anomalies that are associated with a magma chamber within the caldera (Schuler et al., 2015).

The magmatic plumbing in Krafla gained particular notoriety in 2009 when a borehole, K-39, unexpectedly encountered magma at depths of 2062m while drilling into the geothermal system within the central volcano (Mortensen et al., 2010).

Subsequently, the nearby IDDP-1 drillhole also drilled into melt at a depth of 2104 m (Elders et al., 2014b). These magma bodies have received substantial attention both as targets of geochemical and geophysical surveys and as a model for superheated geothermal power generation (Elders et al., 2014a). The unexpected encounter of rhyolitic magma at such shallow depth also emphasized the limitations of conventional geophysical methods in detecting magma, as these bodies were not recognized in pre-drilling surveys.

2.4 Data and method

Seismic activity at Krafla is currently monitored by 17 permanent seismic stations (yellow symbols in Figure 2.1a) operated by ISOR on behalf of the National Power Company and the Iceland Meteorological Office (IMO). Krafla was also a subject of recent seismic deployments associated with an ongoing international initiative known as the Integrated Methods for Advanced Geothermal Exploration (IMAGE). The blue stars shown in Figure 2.1b represent stations deployed for vertical seismic profiling (VSP) measurements with controlled sources during the IMAGE field campaign (ISOR, 2016).

As a part of the Deep Roots of Geothermal systems (DRG) project, supported by ISOR, the GEOthermal Research Group (GEORG) and Icelandic power companies, 20 seismic stations were deployed at 200m spacing as shown by the red stars on Figure 2.1b. The DRG network used Lennartz 0.2 sec sensors with a sampling frequency of 200 Hz. The seismic data were recorded from July to August 2014 and a total of 989 microearthquakes were subsequently detected and located. Figure 2.3 shows representative recordings of both nearby and relatively distant microearthquakes captured by this array. In addition to prominent direct P and S arrivals, coherent energy is evident in the P wave coda (*e.g., Pr* in Figure 2.3). The relatively close spacing between these stations, coupled with the availability of

adjacent microearthquake clusters, suggested that the VRSP method might be successful in extracting reflection imagery.

In this study, seismic recordings of 989 microearthquakes of magnitude less than M_L 2 (smallest M_L -0.03) were extracted in 1 minute windows for imaging beneath Array 1 and 2 (Figure 2.4). We used vertical component records in order to minimize any S wave contamination in our P wave imaging. The recordings were normalized to the average root-mean-square (RMS) amplitude of each window on a trace-by-trace basis for each microearthquake. The strong coherent seismic energy labeled *Pr* in Figure 2.3a, arriving shortly after the direct P wave, is here interpreted as a reflection of downgoing energy from source reflecting from an interface beneath the hypocenter, an interpretation supported by the analysis described below. To avoid any individual record dominating summations in which it is involved (*e.g.,* during correlation), these traces were then renormalized on an earthquake ensemble-by-ensemble basis for each individual microearthquake. The recordings were also bandpass filtered with corner frequencies of 2 to 80 Hz prior to cross-correlation in order to emphasize body waves at the expense of any surface wave contributions (*e.g.,* ambient noise). The resulting correlations for each earthquake were then summed to produce either autocorrelations or cross correlations as described below.

VRSP uses seismic interferometry to redatum the surface-reflected energy (ghost) to surface source positions. This is accomplished by cross-correlating the signals from the station at the virtual source position with those recorded at the remaining real receivers. (*e.g.,* Schuster et al., 2004; Weaver, 2005; Torij et al., 2007; Draganov et al., 2007). The basic principle is illustrated in Figure 2.5a in which correlation of the signals at two stations results in a representation of the signal recorded at one station as if it came from the other station (virtual source). When the offset between virtual source and real receiver is zero, this reproduces the

autocorrelation model of Claerbout (1968). In this end-member case, the results are completely independent of the depth or timing of the real event, *e.g.,* microearthquake. If there is a sufficient number and appropriate distribution of sources, then summing all the autocorrelations is equivalent to imaging with ambient noise (*e.g.,* Draganov et al., 2009).

Figure 2.5b also illustrates how cross-correlation can generate an "artifact" from downgoing energy that encounters a reflecting interface. The result is an apparent reflection occurring at a travel time that corresponds to re-datuming of the surface to the depth of the earthquake. Note this will be only the case for laterally homogeneous medium, however, since in the presence of lateral inhomogeneity, it would not be easy to interpret the resulting artifact as a specific reflection. Although this arrival represents information about the reflection that can be extracted by other methods (*e.g.,* Quiros et al., 2015), it constitutes "noise" in the seismic image keyed to the re-datumed ghost (Figure 2.5a). However, by summing multiple earthquakes from varying depths, the signal corresponding to the raypaths in Figure 2.5a interfere constructively, while those in Figure 2.5b tend to interfere destructively (*e.g.,* Draganov et al., 2013).

Another potential artifact that can arise is when the distribution of sources is not uniform with respect to azimuth. Since VRSP uses the direct waves of the microearthquakes, the directivity of the events may contribute to the result as artifact (*e.g.,* Emoto et al., 2015). If the P-S time interval is sufficiently long to include higher order multiple reflections from an earthquake, one can process exclusively using coda waves (*e.g.,* Nishitsuji et al. 2016). Using the P wave coda from regional earthquakes for imaging can substantially reduce some artifacts. However, the relatively short S-P arrival times relative to the two wave travel time of the ghost reflections of interest for most of the earthquakes in this case (*e.g.,* Figure 2.3a) preclude effective use of this

approach. Moreover, the use of the P coda alone depends upon higher order multiples, which can be expected to be quickly attenuated in a hot volcanic system.

In this study, virtual shot gathers were generated by cross-correlating each station in turn with all the stations for each recorded earthquake, then summing over all microearthquakes. Figure 2.4 shows the distribution of the microearthquakes selected for imaging projected onto the nominal azimuths of the two recording arrays. The selection criteria for these events are described in more detail below. However, it is immediately obvious from Figure 2.4 that the earthquakes are not randomly distributed with respect to the arrays, but tend to be asymmetrically clustered in both lateral position and depth. Moreover, the span of these earthquakes would seem to violate one of the conditions of interferometric theory, *i.e.,* that the physical sources should enclose the receivers (Wapenaar and Fokkema, 2006; Draganov et al., 2006). In the following section, we will show how the use of both forward and backward directed virtual shot gathers, together with common reflection point binning of those shot gathers, can overcome these limitations.

After a preliminary analysis of autocorrelation results (see below), seismic reflection sections from the virtual shot gathers were then produced by conventional multichannel processing (*e.g.,* Yilmaz, 2001): Common Midpoint Point (CMP) binning (resulting in uniform image spacing), application of NMO corrections appropriate for previously measured P wave velocities (Brandsdóttir et al., 1997), and then stacking (summing) the recordings for all source-receiver pairs for each CMP Bin. To further highlight the dominant reflection signals, the resulting stacks were again bandpass filtered, this time between 6 to 12 Hz. Exponential gain recovery was applied prior to display.

3.5 Results

3.5.1 Autocorrelation

Initially, a brute force autocorrelation section was generated by simply adding the autocorrelations of each station's record for all 989 earthquakes (Figure 2.6a and 2.6b). This autocorrelation section mimics an unmigrated stacked, single-fold zero source-receiver offset survey. The best results are expected when autocorrelating signals from earthquakes that are either located directly beneath every station or the positions of these sources are well-distributed stochastically in space. Thus, we would expect the autocorrelation results to suffer from the clustering of the sources; this should especially be the case for the most northeastern stations from Array 1 (Figure 2.4a). For these "outlier" stations, we would expect virtual reflections to arrive earlier than their real counterparts (Cabolova, 2014).

The resulting seismic section for Array 1 (Figure 2.6a) does exhibit a number of coherent arrivals, both subhorizontal and dipping (*e.g.,* marked by arrows). However, this coherency appears to be relatively localized and scattered, due in part to the irregular spacing between stations. This is especially true for Array 2, which has fewer stations to define coherency. Moreover, the autocorrelations provide little basis for discriminating virtual reflections from coherent artifacts (*e.g.,* Figure 2.6b). Although the energy in such artifacts can be expected to weaken as the number and depth range of the microearthquake sources increase, the limited number and diversity of events available here may be inadequate for effective mitigation of artifact amplitudes.

2.5.2 Microearthquakes as stochastic noise

The most common approach to extracting body waves from passive recordings is to assume that the source energy arises from unknown but favorably distributed locations (Draganov et al., 2006). This approach is represented by the stacked reflection section in Figure 2.7a, computed from virtual shot gathers using all 989 earthquakes recorded by the network. Although the energy binning inherent in the

CMP processing results in a more uniform spatial distribution of traces, lateral coherence is still spotty and relatively unconvincing as evidence of subsurface reflectivity. There is a hint of subhorizontal coherency at 0.9 s and a weak but pervasive dipping coherency throughout the section.

Following the methodology of Nishitsuji et al. (2016), we have also cross-correlated the P coda alone, first using those earthquakes sufficiently distant (*i.e.,* $2^{\circ} \leq$ epicentral distance $\leq 6^{\circ}$) to provide an adequate window between P and S waves (Figure 2.7b). Before CMP processing of the P coda results, the virtual shot gathers were also filtered using multidimensional deconvolution (MDD) using an approximate point spread function (PSF) computed for a time-gate of $|t| < 0.5$ s. This step of applying MDD to interferometry has been found to minimize blurring of the PSF at larger offsets (Van der Neut et al., 2010). The MDD was performed based on truncated singular-value decomposition. However, the resulting reflection section (Figure 2.7b) seems to exhibit even less coherency than the autocorrelation and the simple cross-correlation stacks. As mentioned earlier, the higher order multiple reflections upon which this technique is based may be significantly attenuated in this volcanically active and structurally complex area. The seismic section in Figure 2.7c was produced in the same manner as the section in Figure 2.7b, but using only local microearthquakes. Although more subhorizontal coherency is apparent in 2.7c vs. 7b especially at about 0.8 s, the P-S times of the local earthquakes are too short to allow an estimation of the PSF without potential leakage of S wave energy into the result.

2.5.3 Imaging with selected earthquakes

There are several possible explanations for the poor results obtained by the ambient noise approach to imaging with the full set (989) of earthquake sources. The issue of attenuation of multiply scattered energy associated with shallow magmatic activity has already been raised. Another possible factor is illustrated in Figure 2.8.

Virtual reflections from offline sources (green circle in Figure 2.8) sample subsurface locations (blue dots) that are different from the common midpoints (CMP) defined by the real stations and both the epicenter of the physical source (gray dots) and the virtual source positions (black dots). This discrepancy will decrease with decreasing offset of the source. The 3D distribution of earthquake sources results in a lateral spread of subsurface reflection points that sample different reflector positions, thus violating the common reflection point assumption used to bin and stack the data. Therefore, we would expect a better image should result when using only sources which lie beneath and laterally near the recording array so that their virtual CMPs lie within the CMP bins defined by the geometry of the resulting virtual source gathers.

Microearthquakes were thus selected such that their first-order ghost reflection points fall within 100 x 100m CMP bins defined by the 200m receiver spacing as shown in Figure 2.8b. The use of these selected epicenters should a) minimize lateral offset of virtual reflection points from the CMP bins defined by the virtual source-real receiver geometry as well as b) minimize the divergence of the normal moveout (NMO) correction computed from the virtual source-real receiver geometry from the actual moveout displayed by the virtual reflection. The first condition places priority on real sources being near the actual line of receivers. The second condition places a priority on using real sources near the virtual source (*e.g.,* Kim et al., 2015).

The result of simple cross-correlation and summing of the selected source records is illustrated by the virtual shot gather in Figure 2.9. It is noticeable that there are clear linear arrivals with apparent velocities (~ 4.0 km/sec) that are consistent with those measured locally for direct P waves (ISOR, 2016). Such direct waves imply horizontally propagating energy and near-surface sources, we postulate that this energy is derived from ambient background noise rather than the microearthquakes sensu stricto. More to the point, these virtual shot gathers exhibit more clearly defined

coherent phases than the full blown stacks computed by using the full set of available earthquakes (*e.g.,* Figure 2.7). Stacked virtual reflection sections produced from virtual shot gathers for selected subsets of the earthquakes are shown in Figure 2.10 and 2.11.

It is important to note that the strength of coherent energy (*e.g.,* R2 and R5 in Figures 2.10 and 2.11) increases as the number of events used in the stack increases (Figure 2.10 and 2.11), supporting our conclusion that they are reflections as opposed to random noise or processing artifacts. However, we found relatively little improvement in the signal-to-noise as the number of events increased beyond 40. This point of diminishing returns is associated with the inclusion of events that have large offsets from the array, consistent with our expectation that inclusion of more distant sources degrades the stack due to lateral dispersion of the real subsurface reflection points. Whereas all of the events used to produce the section shown in Figure 2.10a-d have reflection points that fall within the 100 x 100m CMP bins, the additional events in Figure 2.10e have offsets in excess of 700m. Note that coherent energy is more evident along Array 1 than Array 2 (Figure 2.11), which we attribute to the much smaller number of suitably located earthquakes available and smaller number of recording stations along Array 2 (resulting in much lower effective CMP stacking fold). To improve the visibility of reflection energy in these images, a common linear enhancement filter, FX deconvolution (Yilmaz, 2001), was applied in Figure 2.12.

As noted earlier, intrinsic to all of the imaging shown here is the fact that the distribution of earthquakes relative to the station locations would seem to violate the precept in seismic interferometry that the recording stations should be enclosed by the sources. Clearly for Array 1 for example, the stations at the NE end of the array lie well beyond the selected earthquakes used here. In other words, for these stations, the direct path from earthquake to virtual sources has no commonality with any ghost

reflection. Thus the shot gathers for which these stations are the virtual sources have no useful reflection contribution to make any CMP gather to which they participate. However, this is compensated by the virtual sources to the SW which, with exception of the SW most station, do have an appropriate geometry to generate a virtual reflection at the appropriate time. Thus, almost every CMP gather has a contribution from NE stations as virtual sources and SW stations as virtual sources. The latter is simply the time reverse cross-correlation sum of the former. Thus each CMP gather has both positive and negative lags of the cross-correlations of each station with another.

2.6 Discussions

2.6.1 Interpretation

The features responsible for the more prominent reflection bands in the VRSP (*e.g.,* Figure 2.13) are largely a matter of conjecture. Since this section does not pass directly over the boreholes (Figure 2.1b), direct correlations with known lithologic variations are extrapolations at best. However, the prominent phase R2 in Figure 2.10 corresponds to a depth of about 2.75km, comparable to the depth of the shallow magma body intersected by IDDP-1 at 2104 km (Ármannsson et al., 2014). To assess this correlation, a synthetic VRSP (Figure 2.12c) was computed from the simple geologic model shown in Figure 2.12d. The thickness of the magma target in the model is arbitrarily set to be 100m. To obtain the synthetic stack, synthetic seismograms were computed using ray based modeling software (Omni TM Schlumberger) for 23 impulsive subsurface sources (P wave only) with dominant frequencies of 6 to 12Hz corresponding to the microearthquake distributions used in Figure 2.12b as they would be recorded by a linear array of 14 receivers at the free surface spaced 200m apart.

R1 in Figure 2.12 marks the expected phase that may have resulted from cross-

correlating the direct P wave with the reflection from the top of the magma reflector of originally downgoing energy from the microearthquake sources, *e.g.,* the geometry depicted in Figure 2.5b. However, the arrival time on the virtual reflection section for this energy is dependent upon the depth of the source. Hence, stacking such energy for the same reflector but for sources at various depths that illuminates from all angles to the receivers should result in its destruction as a coherent phase (Draganov et al., 2004). Moreover, no such artifact emerges from the synthetic section (Figure 2.12c). Finally, this phase is also visible in Figure 2.7c derived independently using seismic interferometry with coda waves with MDD. Thus, we interpret R1 as most likely a shallow reflector rather than an interferometric artifact.

The flat reflection R2 from the hypothesized magma layer arrives on the synthetic reflection section at the same travel time as the observed phase on the VRSP section derived from the selected microearthquake recordings. This simple correspondence strongly reinforces the association of the coherent subhorizontal phase at about 1s travel time with the magma encountered during drilling. R2 being a virtual reflection from the magma interface is also consistent with the *Pr* in Figure 2.3 being a reflection of the downgoing energy from the same interface (e.g. Figure 2.5). The cross-correlation of direct P arrivals with the ghost reflections from a liquid to solid transition should result in positive polarity reflection, *i.e.,* a deflection to the right (black) on the seismic traces, as is observed on the virtual section. The combination of relatively high amplitude, positive polarity and flat geometry of R2 are all consistent with a fluid. Although melt is the most likely possibility, due to the correlation to the borehole magma, other fluids associated with magma (entrapped brines, steam, CO2, SO2) could also give rise to strong reflection (Makovsky et al., 1996). R3 could correspond to a reflection from its base if it were 500 m thick, or simply be another pre-existing extrusive or intrusive interface. R4, the dipping band of energy just below

R3 is only evident from Array 1; without 3D control, it could represent energy arriving from out of the plane of the section (*e.g.,* sideswipe).

The identification of other coherent phases is more speculative. R5, for example, could mark the top of the postulated deeper feeder chamber in the geologic model of Krafla (Figure 2.2), or simply represent another intrusion, lava unit, other fluid (brine, steam) accumulation or fault. It is important to note that the phases not clearly imaged on the cross line could arise from structure located laterally away from Array 1 (*e.g.,* sideswipe). This ambiguity emphasizes the need for 3D imaging using a true 2D surface recording array.

3.6.2 Complications

Complications not addressed here which could affect VSRP imaging include: a) S wave contributions to the cross-correlation functions, b) variations in microearthquake focal mechanisms, such as polarity changes, that degrade the stack, c) variations in the source function of rupture, which could likewise negatively affect wavelet stacking, and d) contributions from converted phases (*e.g.,* S to P). Although some S wave energy may contaminate cross-correlation sums (even though only vertical component records were used here), it should destructively interfere as we increase the number of earthquakes of different P-S interval times in the process. Even if such energy still remains in the stack, the direct P-S time differences from the selected microearthquakes are too short to explain the magma reflection. Moreover, the velocity used to stack the P reflections should work to degrade such arrivals in the CMP stack. The impact of source function variations should be minimal due the use of small magnitude microearthquakes. Also the actual wavelet shape is largely irrelevant, as it will be represented by its zero-phase equivalent after correlation. Polarity reversals across focal planes for either the direct or various reflected signals within the array could be detrimental. However, the direct arrivals of the selected

microearthquakes exhibit the same polarity across the arrays (*e.g.,* Figure 2.4) suggesting polarity changes due to focal mechanisms are not a serious issue.

3.7 Conclusions

The K-39 and the IDDP-1 wells provide a unique opportunity for calibrating geophysical methods against a known magma target at depth. In this study, we show how body waves from microearthquakes can be processed by seismic interferometry (VRSP) to produce high resolution reflection imageries beneath the geothermal field at Krafla, Iceland. The VRSP image produced by the pilot dataset contains prominent reflections that correspond to the depth of a magma body encountered by the IDDP-1 well. Other virtual reflections could correspond to additional intrusions, including feeder chambers, buried extrusive layering or even fluid pockets. However, true 3D recording (*e.g.,* 2D dense surface array) is needed to properly position of many of these features, thus their identification at present is speculative at best. Dense recording arrays, such as those used in this study, represent a new capability to generate high resolution subsurface imagery. Such technology is becoming more economically available even for 2D arrays for true 3D imaging in the form of the continuously recording nodal systems now in common use in oil exploration (*e.g.,* Lin et al., 2013; Inbal et al., 2015). We do not suggest that VRSP is a replacement for more conventional, controlled source survey at the surface. However, it does have the obvious advantage of not requiring the use of expensive artificial sources, such as explosives in boreholes or vibroseis trucks. It also eliminates any negative environmental or societal impacts, not to mention acquisition permit difficulties, associated with artificial sources at the surface. The cost differential becomes particularly acute if time-lapse imaging (*i.e.,* multiple surveys to search for time dependent changes in reflectivity at depth) is desired. The advantage of this approach over teleseismic techniques (*e.g.,* receiver functions) is the higher resolution that can

be achieved from the higher frequency content of microseismic events. Ambiguities notwithstanding, these results confirm virtual reflection techniques as a promising new method for detecting and mapping subsurface structure at sites characterized by high levels of microseismicity.

2.8 Figures

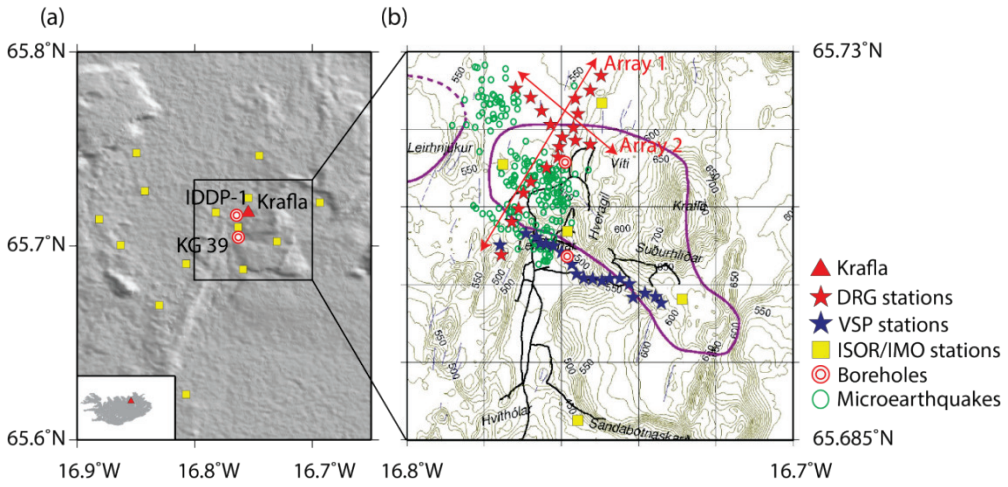

Figure 2.1: (a) Survey area showing location of IDDP-1 and KG-39 boreholes, the Krafla caldera and permanent seismic stations (yellow dots). (b) The blue and red stars represent DRG Krafla stations deployed in the recent ISOR/DRG/IMAGE experiment from which the data example in Figure 2.3 was drawn. Arrays in red are used in this study. The blue stations were deployed for VSP measurements during a recent IMAGE field campaign. Purple contours show estimated boundaries of magma chambers seen as S wave shadows during studies of the Krafla Fires (1975-1984) (Einarsson, 1978).

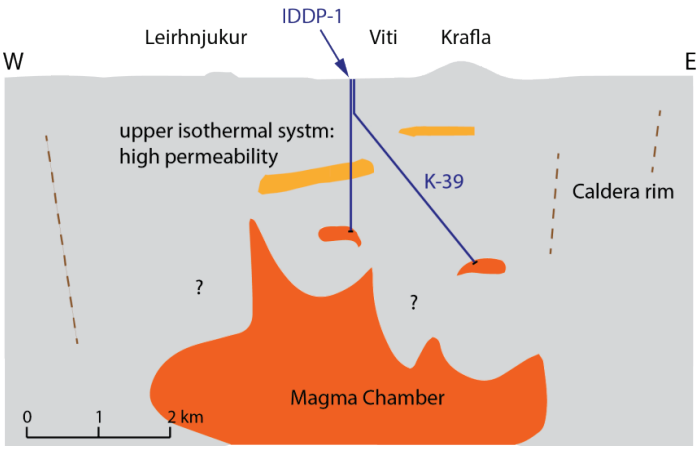

Figure 2.2: An east-west geologic model for the Krafla caldera. Modified from Ármannsson et al. (2014).

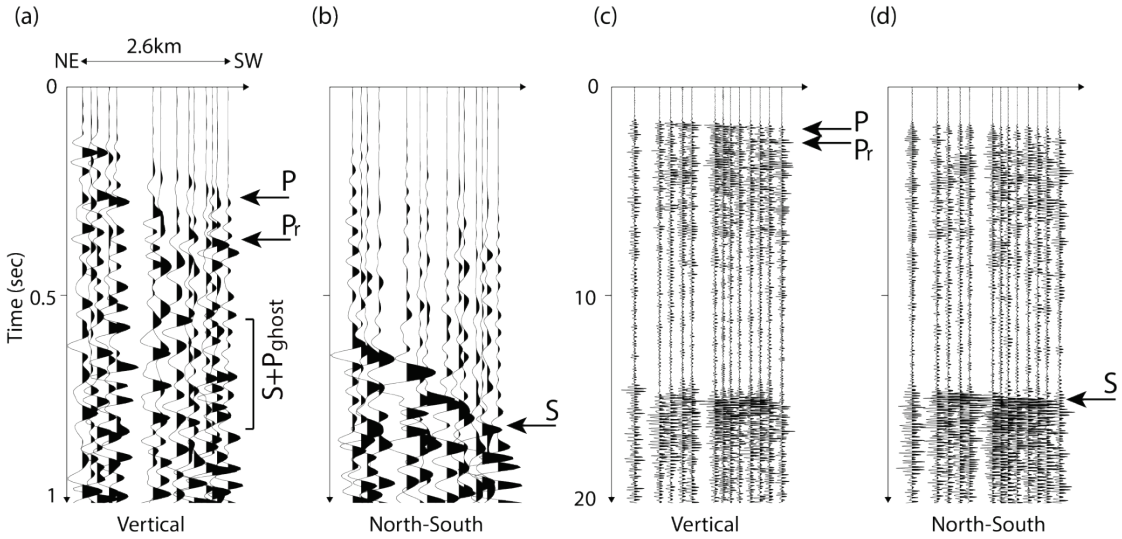

Figure 2.3: Sample recordings of microearthquakes used in this study. Note: t=0 s time is arbitrary, not the origin time of the earthquake. (a) Vertical component seismogram for earthquake within the seismic array. (b) North-south component of the same local earthquake. (c) Vertical component for an earthquake located at a greater distance and (d) its north-south component. Traces are depicted for stations extending from northeast to southwest (Array 1 in Figure 2.1). In addition to clear direct P and S arrivals, coherent arrivals are evident in the P wave coda (*e.g., Pr*).

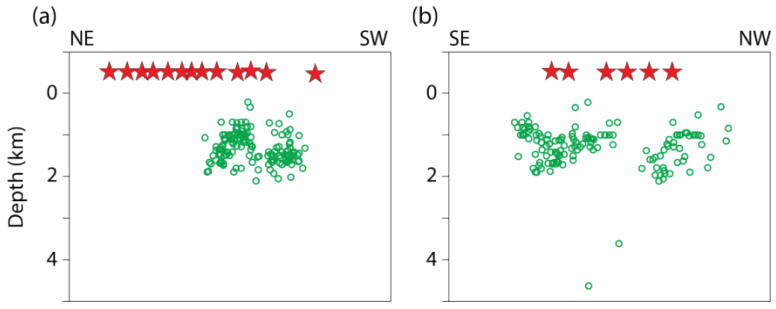

Figure 2.4: (a) Depth distribution of microearthquakes used in this analysis. Earthquake locations projected onto planes corresponding to the nominal azimuths of Array 1 and (b) Array 2.

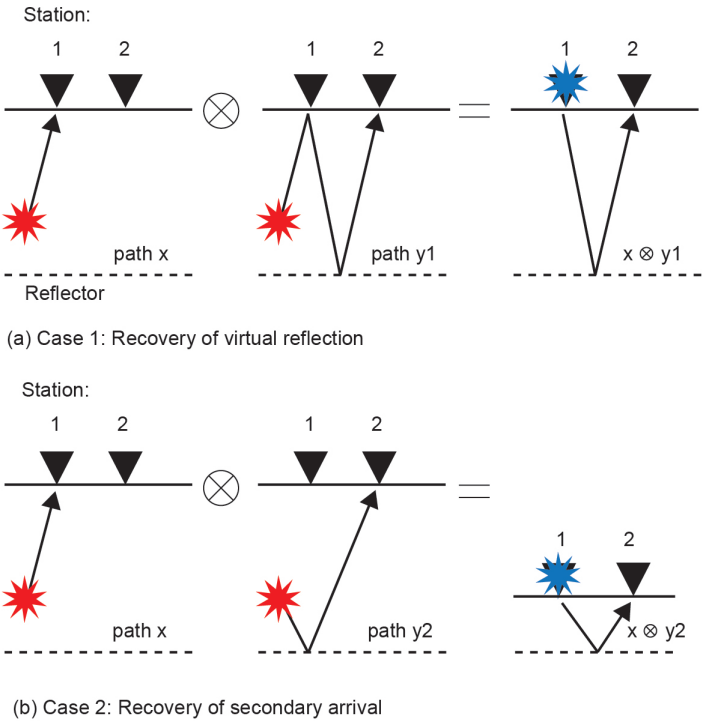

Figure 2.5: Virtual reflection profiling by re-datuming of deep sources. (a) Cross-correlation of the initially upward traveling energy recorded at station 1 with its subsurface reflections recorded by the remaining stations (*e.g.,* station 2) produces a virtual source gather corresponding to a virtual source located at station 1. (b) Cross-correlation of the reflection of the initially downward traveling energy recorded at station 1 with its subsurface reflections recorded by the remaining stations also produces a virtual source gather but one with the sources redatumed to the depth of the real source. After Schuster (2009).

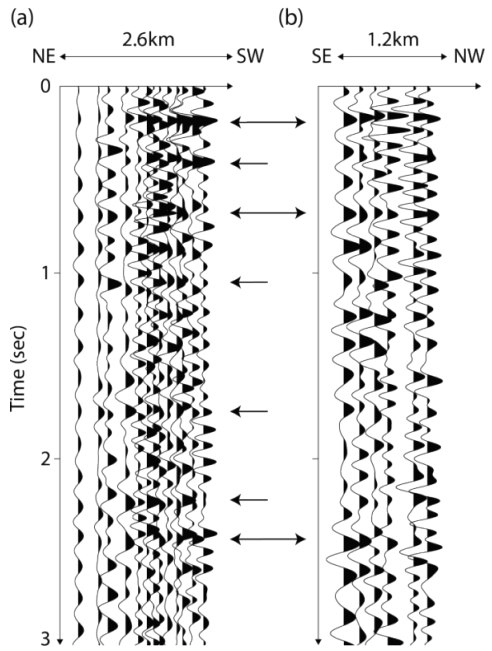

Figure 2.6: (a) Autocorrelation seismic reflection sections from Array 1 and (b) Array 2. Black arrows indicate coherent phases.

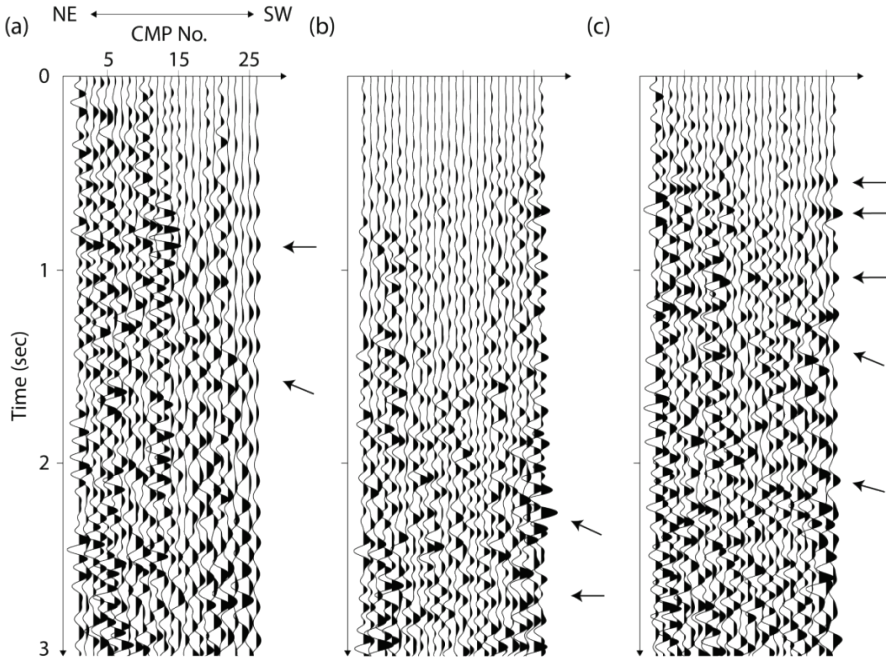

Figure 2.7: (a) CMP stacked seismic section treating all 989 events as random noise. (b) Stacked section using the P wave coda only for 124 selected regional earthquakes. (c) Same as (b) except for the use of 145 local microearthquakes. In both (b) and (c), multidimenstional deconvolution (MDD) was applied after cross-correlation. Arrows

indicate coherent phases that may correspond to reflections from physical interfaces at depth.

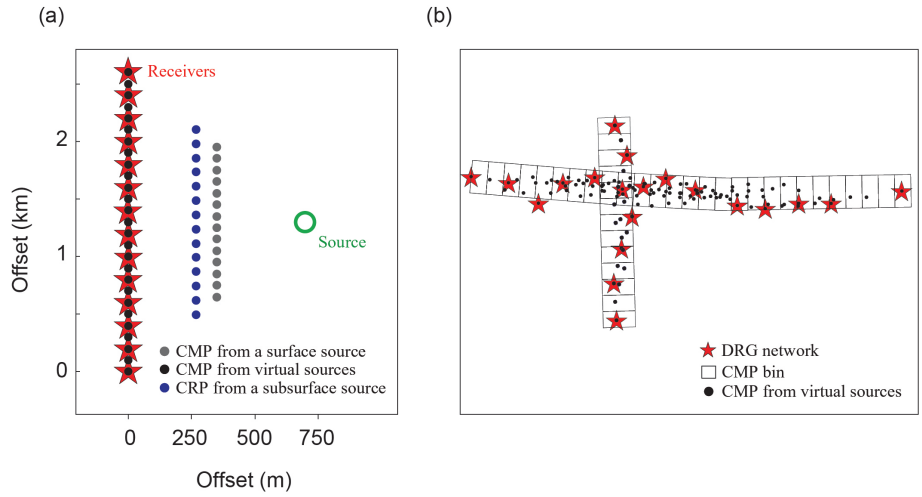

Figure 2.8: (a) Relative virtual reflection points associated with a source that is laterally displaced from an array. Note the spatial discrepancy between the expected Common Reflection Points (CRP, gray dots) from the conventional Common MidPoints (CMP, black dots). (b) CMP binning (100 x 100 m) for the DRG arrays.

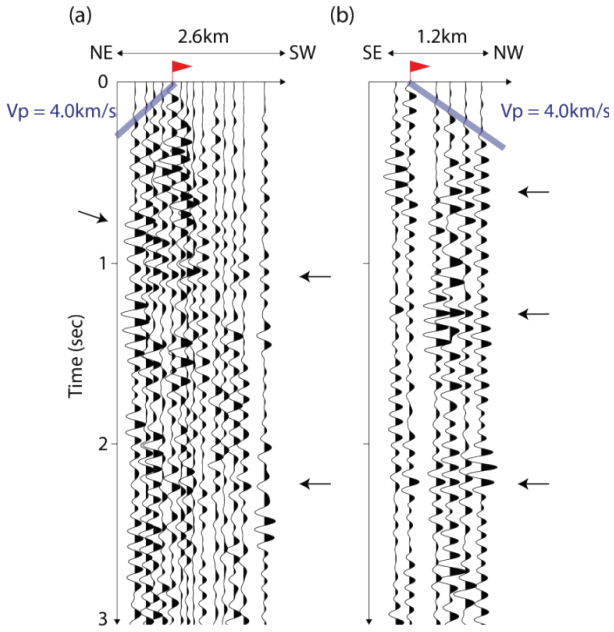

Figure 2.9: (a) Virtual source gathers for Array 1 and (b) Array 2 computed from selected earthquakes sources. Red flags represent the location of the virtual source. Blue line represents the linear energy, here interpreted as direct virtual P wave arrivals and their associated velocity of 4km/s. Black arrows indicate laterally coherent arrivals interpreted to be reflections from subsurface interfaces.

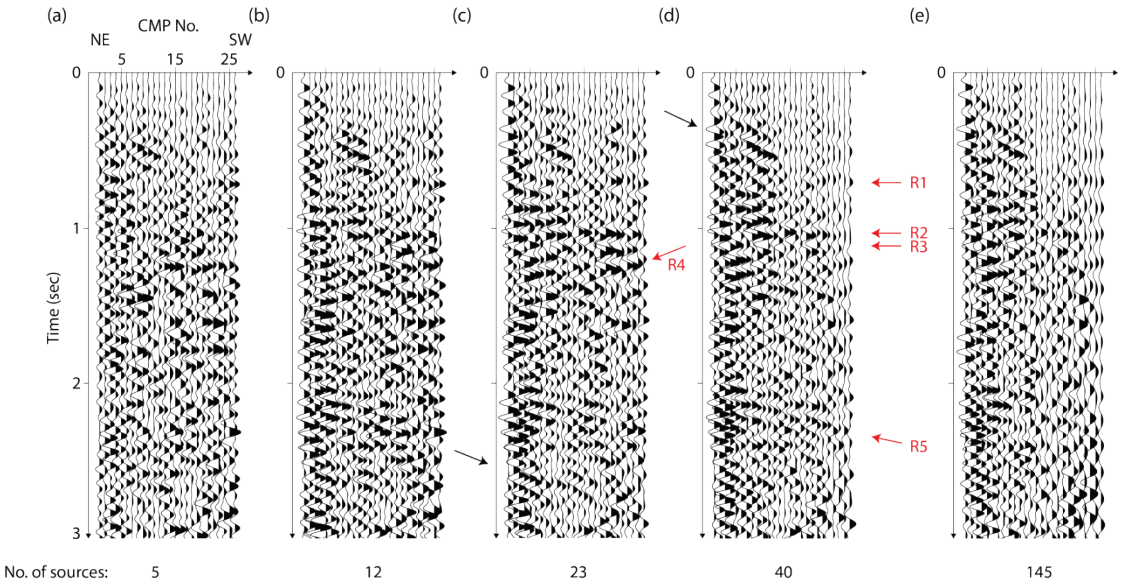

Figure 2.10: Partial stacks for Array 1 generated with selected earthquake subsets. The number of earthquakes used in each stack, indicated at the bottom of each panel, increases to the right. Increasing CMP No. corresponds to SW direction. R1-R5 indicate coherent reflections discussed in the text. Note R2 corresponds to depth where the magma was drilled. Other coherent phases are also indicated.

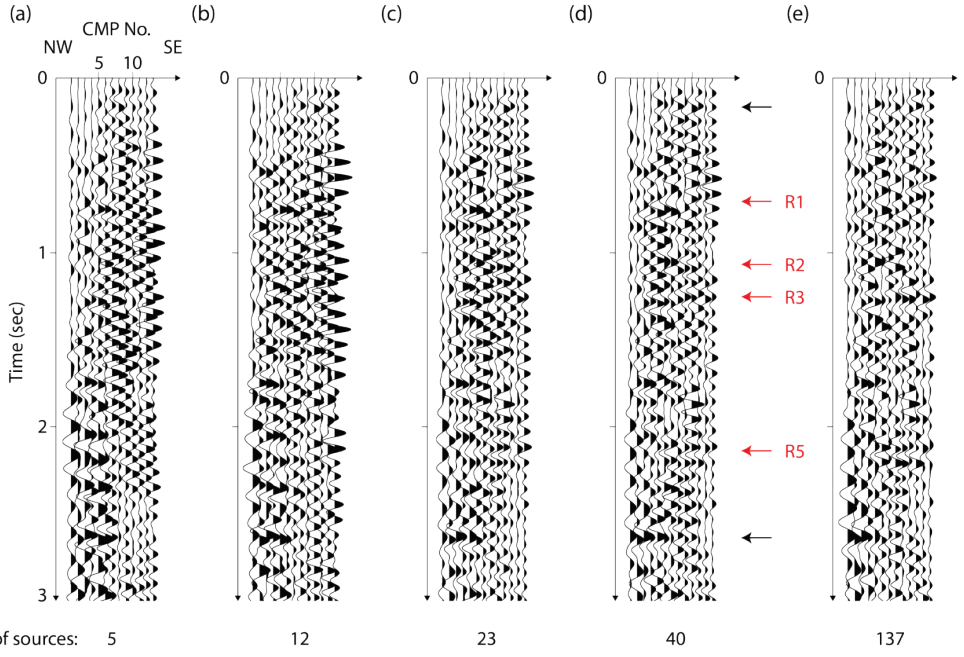

Figure 2.11: Partial stacked seismic sections for Array 2, generated with selected earthquakes. The number of sources used in each stack, indicated at the bottom of each panel, increases to the right. Increasing CMP No. corresponds to SE direction.

R1-R5 are coherent reflections beneath Array 2. Note R2 corresponds to depth where the magma was drilled. Other coherent phases are also indicated.

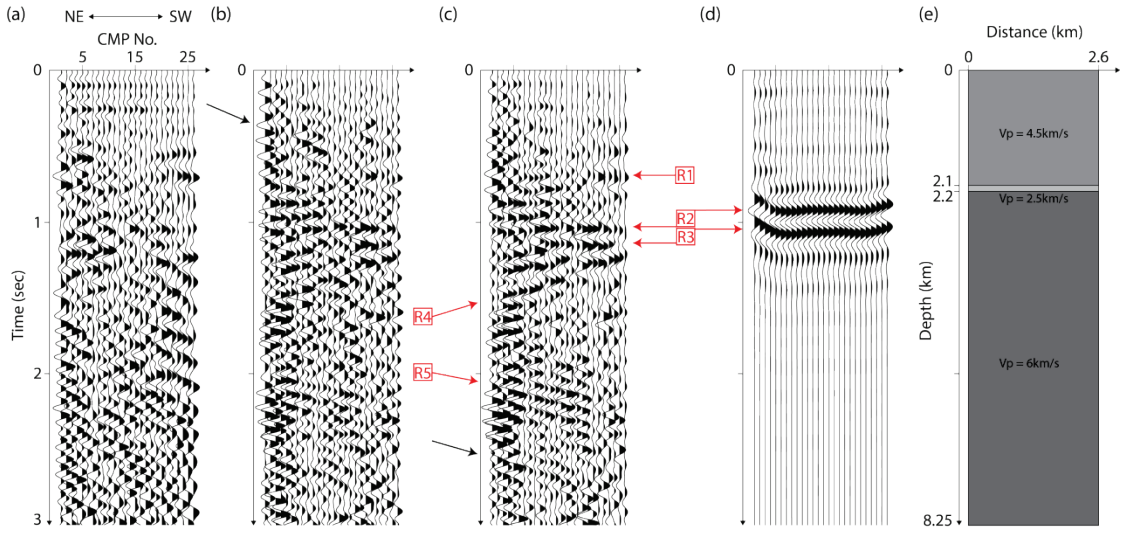

Figure 2.12: (a) Stacked section of Array1 from figure 2.7c enhanced by FX deconvolution (b) Stacked sections using 23 selected microearthquakes (Figure 2.8). (c) Stack of selected earthquakes enhanced by FX deconvolution. (d) Simulated VRSP image produced using synthetic virtual source gathers computed from the model in (e). (e) A simple velocity model of the upper crust at Krafla used to compute the synthetic in (d). A magma body was placed at a depth comparable to that at which magma was encountered by the Krafla boreholes with an assumed thickness of 100m. P wave velocity (2.5km/s) for the magma body based on lab measurements (Murase and Mcbirney, 1973). Increasing CMP No. corresponds to the SW direction. The synthetic section was computed using the same geometries of microearthquakes used in (b). See text for modeling details.

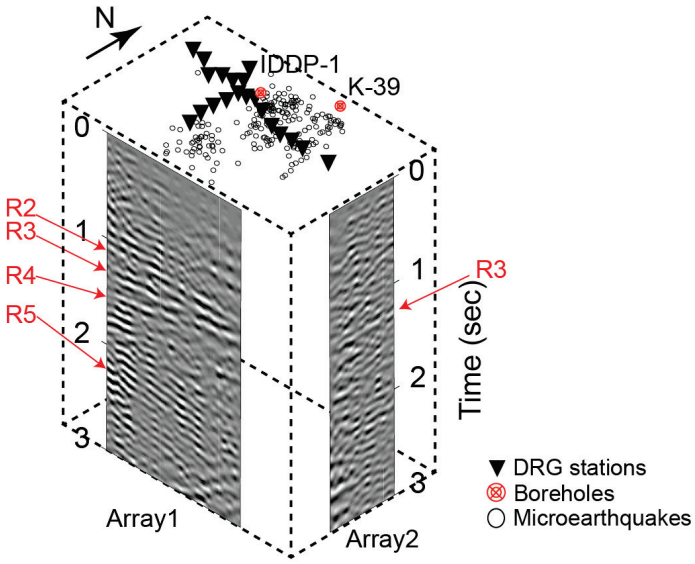

Figure 2.13: Reflection images of the Krafla subsurface in 3D fence display. The coherency enhanced reflection images from Array 1 and 2 are displayed here in raster format. The DRG network, microearthquakes source locations, and the two boreholes are also indicated at the top of the figure. R2-R5 are coherent reflections beneath Array 1 and 2. R2 corresponds to depth where the magma was encountered in boreholes.

REFERENCES

Ágústsson, K., Ó. G. Flóvenz, Á. Guḥmundsson, and S. Árnadóttir (2012), Induced seismicity in the Krafla high temperature field, GRC Transactions, 36(2012), 975–980.

Ármannsson, H., T. Fridriksson, G. H. Gudfinnsson, M. Ólafsson, F. Óskarsson, and D. Thorbjörnsson (2014), IDDP—The chemistry of the IDDP-01 well fluids in relation to the geochemistry of the Krafla geothermal system, Geothermics, 49, 66–75.

Árnason, K., A. M. Vilhjálmsson, and T. Björnsdóttir (2009), A study of the Krafla volcano using gravity, micro earthquake and MT data, Short Cource II on Surface Exploration for Geothermal Resources at Lake Naivasha, Kenya.

Arnott, S. K., and G. R. Foulger (1994), The Krafla spreading segment, Iceland: 1. Three-dimensional crustal structure and the spatial and temporal distribution of local earthquakes, Journal of Geophysical Research: Solid Earth, 99(B12), 23801–23825.

Benz, H. M., and R. B. Smith (1984), Simultaneous inversion for lateral velocity

variations and hypocenters in the Yellowstone region using earthquake and refraction data, Journal of Geophysical Research: Solid Earth, 89(B2), 1208–1220.

Blanck, H., K. Ágústsson, and K. Gunnarsson (2014), Seismic monitoring of Krafla: for the period November 2014 to November 2015, Iceland GeoSurvey (ISOR).

Brandsdóttir, B., and W. H. Menke (1992), Thin low-velocity zone within the krafla caldera, ne-Iceland attributed to a small magma chamber, Geophysical research letters, 19(24), 2381–2384.

Brandsdóttir, B., W. Menke, P. Einarsson, R. S. White, and R. K. Staples (1997), Färoe-Iceland Ridge Experiment 2. Crustal structure of the Krafla central volcano, Journal of Geophysical Research: Solid Earth, 102(B4), 7867–7886.

Brocher, T. M. (1981), Geometry and physical properties of the Socorro, New Mexico, magma bodies, Journal of Geophysical Research: Solid Earth, 86(B10), 9420–9432.

Brown, L. D., P. A. Krumhansl, C. E. Chapin, A. R. Sanford, F. A. Cook, S. Kaufman, J. E. Oliver, and F. S. Schilt (1979), COCORP seismic reflection studies of the Rio Grande rift, Rio Grande rift: Tectonics and magmatism, 169–184.

Brown, L. D., W. Zhao, K. D. Nelson, M. Hauck, D. Alsdorf, A. Ross, M. Cogan, M. Clark, X. Liu, and J. Che (1996), Bright spots, structure, and magmatism in southern Tibet from INDEPTH seismic reflection profiling, Science, 274(5293), 1688–1690.

Buck, W. R., P. Einarsson, and B. Brandsdóttir (2006), Tectonic stress and magma chamber size as controls on dike propagation: Constraints from the 1975–1984 Krafla rifting episode, Journal of Geophysical Research: Solid Earth, 111(B12).

Cabolova, (2015), Seismic investigation of deep 2D, 3D and 4D structures using body wave interferometry, computer simulations and semi-conventional processing, PhD Thesis, Cornell University.

Cassidy, J. F. (1992), Numerical experiments in broadband receiver function analysis, Bulletin of the Seismological Society of America, 82(3), 1453–1474.

Claerbout, J. F. (1968), Synthesis of a layered medium from its acoustic transmission response, Geophysics, 33(2), 264–269.

Corry, C. E. (1988), Laccoliths: mechanics of emplacement and growth, Geological Society of America.

Crisp, J. A. (1984), Rates of magma emplacement and volcanic output, Journal of Volcanology and Geothermal Research, 20(3), 177–211.

Darbyshire, F. A., K. F. Priestley, R. S. White, R. Stefánsson, G. B. Gudmundsson, and S. S. Jakobsdóttir (2000), Crustal structure of central and northern Iceland from analysis of teleseismic receiver functions, Geophysical Journal International, 143(1), 163–184.

Davenport, K. K., J. A. Hole, D. A. Quiros, L. D. Brown, M. C. Chapman, L. Han, and W. D. Mooney (2014), Aftershock imaging using a dense seismometer array (AIDA) after the 2011 Mineral, Virginia, earthquake, Geological Society of America Special Papers, 509, SPE509–15.

Draganov, D., K. Wapenaar, and J. Thorbecke (2004), Passive seismic imaging in the presence of white noise sources, The Leading Edge, 23(9), 889–892.

Draganov, D., K. Wapenaar, and J. Thorbecke (2006), Seismic interferometry: Reconstructing the earth's reflection response, Geophysics, 71(4), SI61–SI70.

Draganov, D., K. Wapenaar, W. Mulder, J. Singer, and A. Verdel (2007), Retrieval of reflections from seismic background-noise measurements, Geophys. Res. Lett., 34(4), L04305, doi:10.1029/2006GL028735.

Draganov, D., X. Campman, J. Thorbecke, A. Verdel, and K. Wapenaar (2009), Reflection images from ambient seismic noise, Geophysics, 74(5), A63–A67.

Draganov, D., X. Campman, J. Thorbecke, A. Verdel, and K. Wapenaar (2013), Seismic exploration-scale velocities and structure from ambient seismic noise (> 1 Hz), Journal of Geophysical Research: Solid Earth, 118(8), 4345–4360.

Einarsson, P. (1978), S-wave shadows in the Krafla caldera in NE-Iceland, evidence for a magma chamber in the crust, Bulletin Volcanologique, 41(3), 187–195.

Einarsson, P. (1991), The Krafla rifting episode 1975–1989, Náttúra Myvatns,(The Nature of Lake Myvatn), 97–139.

Elders, W. A., G. Friḥleifsson, and A. Albertsson (2014a), Drilling into magma and the implications of the Iceland Deep Drilling Project (IDDP) for high-temperature geothermal systems worldwide, Geothermics, 49, 111–118.

Elders, W. A., G. Ó. Friḥleifsson, and B. Pálsson (2014b), Iceland Deep Drilling Project: The first well, IDDP-1, drilled into magma, Geothermics, (49), 1.

Emerman, S. H., and R. Marrett (1990), Why dikes?, Geology, 18(3), 231–233.

Emoto, K., M. Campillo, F. Brenguier, X. Briand, and T. Takeda (2015), Asymmetry of coda cross-correlation function: Dependence of the epicentre location, Geophysical Journal International, 201(3), 1313–1323.

Gertisser, R. (2010), Eyjafjallajökull volcano causes widespread disruption to European air traffic, Geology Today, 26(3), 94–95.

Glazner, A. F., and W. Ussler (1988), Trapping of magma at midcrustal density discontinuities, Geophysical Research Letters, 15(7), 673–675.

Gorbatov, A., E. Saygin, and B. L. N. Kennett (2013), Crustal properties from seismic station autocorrelograms, Geophysical Journal International, 192(2), 861–870.

Gudmundsson, A. (2000), Dynamics of volcanic systems in Iceland: example of tectonism and volcanism at juxtaposed hot spot and mid-ocean ridge systems, Annual Review of Earth and Planetary Sciences, 28(1), 107–140.

Harris, A. J. L., J. B. Murray, S. E. Aries, M. A. Davies, L. P. Flynn, M. J. Wooster, R. Wright, and D. A. Rothery (2000), Effusion rate trends at Etna and Krafla and their implications for eruptive mechanisms, Journal of Volcanology and Geothermal Research, 102(3), 237–269.

Huang, H.-H., F.-C. Lin, B. Schmandt, J. Farrell, R. B. Smith, and V. C. Tsai (2015), The Yellowstone magmatic system from the mantle plume to the upper crust, Science, 348(6236), 773–776.

Inbal, A., R. W. Clayton, and J.-P. Ampuero (2015), Imaging widespread seismicity at midlower crustal depths beneath Long Beach, CA, with a dense seismic array: Evidence for a depth-dependent earthquake size distribution, Geophysical Research Letters, 42(15), 6314–6323.

Ishihara, K. (1990), Pressure sources and induced ground deformation associated with explosive eruptions at an andesitic volcano: Sakurajima volcano, Japan, Magma Transport and Storage, 335–356.

Iceland Geosurvey (2016), Active Seismic with VSP in Krafla, NE-Iceland, IMAGE – Summary report of Task 4.2.

Iyer, H. M., J. R. Evans, G. Zandt, R. M. Stewart, J. M. Coakley, and J. N. Roloff (1981), A deep low-velocity body under the Yellowstone caldera, Wyoming: delineation using teleseismic P-wave residuals and tectonic interpretation, Geological Society of America Bulletin, 92(11 Part II), 1471–1646.

Kennett, B. L. N. (2015), Lithosphere–asthenosphere P-wave reflectivity across Australia, Earth and Planetary Science Letters, 431, 225–235.

Kent, G. M. et al. (2000), Evidence from three-dimensional seismic reflectivity images for enhanced melt supply beneath mid-ocean-ridge discontinuities, Nature, 406(6796), 614–618.

Kim, D., L. D. Brown, D. Quiros, and others (2015), Body Wave Imaging with Interferometry of Aftershock Sources, in 2015 SEG Annual Meeting, Society of Exploration Geophysicists.

King, S., and A. Curtis (2012), Suppressing nonphysical reflections in Green's function estimates using source-receiver interferometry, Geophysics, 77(1), Q15–Q25.

Lees, J. M. (2007), Seismic tomography of magmatic systems, Journal of Volcanology and Geothermal Research, 167(1), 37–56.

Lin, F.-C., M. P. Moschetti, and M. H. Ritzwoller (2008), Surface wave tomography of the western United States from ambient seismic noise: Rayleigh and Love wave phase velocity maps, Geophysical Journal International, 173(1), 281–298.

Lin, F.-C., V. C. Tsai, B. Schmandt, Z. Duputel, and Z. Zhan (2013a), Extracting seismic core phases with array interferometry, Geophysical Research Letters, 40(6), 1049–1053.

Lin, F.-C., D. Li, R. W. Clayton, and D. Hollis (2013b), High-resolution 3D shallow crustal structure in Long Beach, California: Application of ambient noise tomography on a dense seismic array, Geophysics, 78(4), Q45–Q56.

Makovsky, Y., S. L. Klemperer, L. Ratschbacher, and D. Alsdorf (1999), Midcrustal reflector on INDEPTH wide-angle profiles: An ophiolitic slab beneath the India-Asia suture in southern Tibet?, Tectonics, 18(5), 793–808, doi:10.1029/1999TC900022.

Matsumoto, S., and A. Hasegawa (1996), Distinct S wave reflector in the midcrust beneath Nikko-Shirane volcano in the northeastern Japan arc, Journal of Geophysical Research: Solid Earth, 101(B2), 3067–3083.

Mortensen, A. K., K. Grönvold, A. Guḥmundsson, B. Steingrímsson, and T. Egilson (2010), Quenched silicic glass from well K-39 in Krafla, North-Eastern Iceland, in proceedings world geothermal congress, Bali, Indonesia.

Murase, T., and A. R. Mcbirney (1973), Properties of some common igneous rocks and their melts at high temperatures, Geological Society of America Bulletin, 84(11), 3563–3592.

Mutter, J. C., G. A. Barth, P. Buhl, R. S. Detrick, J. Orcutt, and A. Harding (1988),

Magma distribution across ridge-axis discontinuities on the East Pacific Rise from multichannel seismic images, Nature, 336(6195), 156–158, doi:10.1038/336156a0.

Nakata, N., R. Snieder, and M. Behm (2014), Body-wave interferometry using regional earthquakes with multidimensional deconvolution after wavefield decomposition at free surface, Geophysical Journal International, 199(2), 1125–1137.

Nelson, K. D. et al. (1996), Partially molten middle crust beneath southern Tibet: synthesis of project INDEPTH results, Science, 274(5293), 1684–1688.

Nishitsuji, Y., S. Minato, B. Boullenger, M. Gomez, K. Wapenaar, and D. Draganov (2016), Crustal-scale reflection imaging and interpretation by passive seismic interferometry using local earthquakes, Interpretation, SJ29-SJ53.

Polteau, S., A. Mazzini, O. Galland, S. Planke, and A. Malthe-Sørenssen (2008), Saucer-shaped intrusions: occurrences, emplacement and implications, Earth and Planetary Science Letters, 266(1), 195–204.

Quiros, D., L. D. Brown, A. Cabolova, C. Chen, K. Davenport, J. Hole, L. Han, M. C. Chapman, and W. Mooney (2015), Reflection Imaging using Earthquake Sources: A Novel Application of Reverse Vertical Seismic Profiling (RVSP), in 2015 SEG Annual Meeting, Society of Exploration Geophysicists.

Roux, P., K. G. Sabra, P. Gerstoft, W. A. Kuperman, and M. C. Fehler (2005), P-waves from cross-correlation of seismic noise, Geophysical Research Letters, 32(19).

Ruigrok, E., and K. Wapenaar (2012), Global-phase seismic interferometry unveils P-wave reflectivity below the Himalayas and Tibet, Geophysical Research Letters, 39(11).

Ryberg, T. (2011), Body wave observations from cross-correlations of ambient seismic noise: A case study from the Karoo, RSA, Geophysical Research Letters, 38(13).

Saemundsson, K. (1991), Geology of the Krafla system, The Natural History of Lake Myvatn, The Icelandic Natural History Society, Reykjavik, 24–95.

Sanford, A. R., and L. T. Long (1965), Microearthquake crustal reflections, Socorro, New Mexico, Bulletin of the Seismological Society of America, 55(3), 579–586.

Sanford, A. R., Ö. Alptekin, and T. R. Toppozada (1973), Use of reflection phases on microearthquake seismograms to map an unusual discontinuity beneath the Rio

Grande rift, Bulletin of the Seismological Society of America, 63(6–1), 2021–2034.

Sanford, A. R., R. P. Mott, P. J. Shuleski, E. J. Rinehart, F. J. Caravella, R. M. Ward, and T. C. Wallace (1977), Geophysical evidence for a magma body in the crust in the vicinity of Socorro, New Mexico, The Earth's Crust, 385–403.

Scarpa, R. (2001), Predicting volcanic eruptions, Science, 293(5530), 615–616.

Schuler, J., T. Greenfield, R. S. White, S. W. Roecker, B. Brandsdóttir, J. M. Stock, J. Tarasewicz, H. R. Martens, and D. Pugh (2015), Seismic imaging of the shallow crust beneath the Krafla central volcano, NE Iceland, Journal of Geophysical Research: Solid Earth, 120(10), 7156–7173.

Schuster, G. T., J. Yu, J. Sheng, and J. Rickett (2004), Interferometric/daylight seismic imaging, Geophysical Journal International, 157(2), 838–852.

Schuster, G. T. (2009), Seismic interferometry, Cambridge University Press Cambridge.

Shapiro, N. M., M. Campillo, L. Stehly, and M. H. Ritzwoller (2005), High-resolution surface-wave tomography from ambient seismic noise, Science, 307(5715), 1615–1618.

Sheetz, K. E., and J. W. Schlue (1992), Inferences for the Socorro magma body from teleseismic receiver functions, Geophysical research letters, 19(18), 1867–1870.

Spera, F. J. (1980), Aspects of magma transport, Physics of magmatic processes, 7.

Tibuleac, I. M., and D. von Seggern (2012), Crust-mantle boundary reflectors in Nevada from ambient seismic noise autocorrelations, Geophysical Journal International, 189(1), 493–500.

Torii, K. et al. (2007), Application seismic interferometry to natural earthquakes measured by small-scale array, in SEG Technical Program Expanded Abstracts 2007, pp. 1362–1366, Society of Exploration Geophysicists.

Tryggvason, E. (1984), Widening of the Krafla fissure swarm during the 1975–1981 volcano-tectonic episode, Bulletin volcanologique, 47(1), 47–69.

Van der Neut, J., E. Ruigrok, D. Draganov, and K. Wapenaar (2010), Retrieving the earth's reflection response by multi-dimensional deconvolution of ambient seismic noise, in 72nd EAGE Conference and Exhibition incorporating SPE EUROPEC 2010.

Voight, B., and R. R. Cornelius (1991), Prospects for eruption prediction in near real-

time, Nature, 350(6320), 695–698.

de Voogd, B., L. Serpa, L. Brown, E. Hauser, S. Kaufman, J. Oliver, B. W. Troxel, J. Willemin, and L. A. Wright (1986), Death Valley bright spot: A midcrustal magma body in the southern Great Basin, California?, Geology, 14(1), 64–67.

Wapenaar, K., and J. Fokkema (2006), Green's function representations for seismic interferometry, Geophysics, 71(4), SI33–SI46.

Wapenaar, K., J. van der Neut, and E. Ruigrok (2008), Passive seismic interferometry by multidimensional deconvolution, Geophysics, 73(6), A51–A56.

Ward, K. M., G. Zandt, S. L. Beck, D. H. Christensen, and H. McFarlin (2014), Seismic imaging of the magmatic underpinnings beneath the Altiplano-Puna volcanic complex from the joint inversion of surface wave dispersion and receiver functions, Earth and Planetary Science Letters, 404, 43–53.

Weaver, R. L. (2005), Information from Seismic Noise, Science, 307(5715), 1568–1569, doi:10.1126/science.1109834.

Wei, W. et al. (2001), Detection of widespread fluids in the Tibetan crust by magnetotelluric studies, Science, 292(5517), 716–719.

Yilmaz, Ö., 2001, Seismic Data Analysis: Society of Exploration Geophysicists.

Yu, J., and G. T. Schuster (2001), Crosscorrelogram migration of IVSPWD data, in SEG Technical Program Expanded Abstracts 2001, pp. 456–459, Society of Exploration Geophysicists.

Zandt, G., M. Leidig, J. Chmielowski, D. Baumont, and X. Yuan (2003), Seismic detection and characterization of the Altiplano-Puna magma body, central Andes, Pure and Applied Geophysics, 160(3–4), 789–807.

Ziolkowski, A., P. Hanssen, R. Gatliff, H. Jakubowicz, A. Dobson, G. Hampson, X.-Y. Li, and E. Liu (2003), Use of low frequencies for sub-basalt imaging, Geophysical Prospecting, 51(3), 169–182.

CHAPTER 3

MAGMA "BRIGHT SPOTS" MAPPED BENEATH KRAFLA, ICELAND, USING RVSP IMAGING OF REFLECTED WAVES FROM MICROEARTHQUAKES

3.1 Abstract

The geometry and distribution of magma in the crust remain controversial topics with recent studies questioning the role of large magma chambers. In this investigation, high-resolution 3D reflection images of crustal discontinuities beneath the Krafla geothermal field in northern Iceland were generated by applying Vertical Seismic Profiling (VSP) techniques adapted from reflection seismology to microearthquake data. Exceptionally large amplitude reflections (bright spots) at a depth of 2.1 km correlate with rhyolitic magma encountered in the IDDP-1 borehole. Although similarly bright reflectors at about 4 km correspond in depth to the top of an inferred magma chamber from previous seismic studies, the scattered reflectivity that persists beneath this deeper reflector argues for a distributed magma system rather than a large feeder chamber.

3.2 Introduction

The Krafla volcano hosts a large geothermal system that is one of the most studied energy fields in Iceland, with geothermal exploration dating back to the early 1970's (Sveinbjornsdottir et al., 1986). Krafla sits in the Northern Volcanic Zone of Iceland and the historical record includes episodic rifting events in the region every 100-150 years (Björnsson and Saemundsson, 1977). The most recent such rifting event documented in the region is during the Krafla-Fires 1975-1984 (Einarsson, 1991). Krafla's magmatic plumbing regained its attention in 2009 when two geothermal boreholes, KG-39 and IDDP-1 (Figure 3.1) unexpectedly encountered magma at depths of 2062 m and 2104 m, respectively, a rare event in drilling history (Mortensen

The material in Chapter 3 has been published under Kim et al., Magma "bright spots" mapped beneath Krafla, Iceland, using reflected waves from microearthquakes.
Journal of Volcanology and Geothermal Research (2018)
doi:10.1016/j.jvolgeores.2018.04.022

et al., 2010; Elders et al., 2014b). These boreholes have received substantial attention as a model for superheated geothermal power generations (Elders et al., 2014a).

A number of geophysical techniques, especially magnetotelluric (MT) and seismic, have been widely used to detect and delineate magma at depth. Examples of recent MT efforts in Iceland have shown the inferred magma body beneath Hengill and Krafla geothermal area (Árnason et al., 2009; 2010). Other studies elsewhere to image magma include the detection of extensive fluid distribution beneath the Tibetan Plateau (Wei et al., 2001; Unsworth et al., 2005), and the combination of partial melt and fluids of Altiplano-Puna magma body (Comeau et al., 2015). Both natural and artificial seismic sources have been used to image magma. Tomographic imaging using both local earthquakes and teleseismic sources are probably the best known (e.g., Lees, 2007). Ambient noise techniques have also been applied to map magma at depth, including attempts to detect temporal variations in the seismic velocity within magma systems (*e.g.,* Brenguier et al., 2007; Jaxybulatov et al., 2014). Another widely used passive seismic technique, receiver function mapping of intracrustal convertors, has also been used to detect and map crustal magma (*e.g.,* Sheetz and Schlue, 1992; Zandt et al, 2003; Wilson et al., 2005). However the highest resolution images interpreted to be of magma come from controlled source reflection surveys (*e.g.,* Brown et al., 1979; de Voogd et al., 1986; Brown et al., 1996; Kent et al., 2000). A drawback of controlled source reflection imaging is the relatively high cost of artificial sources. Conversely, conventional passive methods that rely upon teleseismic sources lack resolution at intracrustal scales (Cassidy, 1992). Here, we apply a technique normally used with controlled sources to obtain high resolution seismic imaging using natural sources, in this case crustal microearthquakes.

Of particular relevance to this study are previous efforts to detect magma using reflected waves from earthquake sources. Sanford and Long (1965) reported an

anomalously strong, late arriving S wave from the midcrust on microearthquake records near Socorro, New Mexico. These phases were subsequently interpreted as the reflected SxS and PxS waves from an extensive magma layer beneath the Rio Grande Rift, now commonly referred to as the Socorro Magma Body (SMB; *e.g.,* Sanford et al., 1973; Balch et al., 1997). This work inspired the interpretation of similar anomalous S waves on microearthquake records in Japan as reflections from magma beneath several volcanic systems. (Hasegawa and Yamamoto, 1994; Matsumoto and Hasegawa, 1996). Byerly et al. (2010) also used microearthquakes to search for magma beneath Montserrat in the Caribbean.

Inamori et al. (1992) were the first to correct the reflection times of anomalous midcrustal reflected S waves for the depth of the source, in this case for the western Nagano Prefecture in Japan. Here, the proper travel time and lateral position corrections are equivalent to those inherent in Vertical Seismic Profiling (VSP), a technique widely used in the oil exploration industry for imaging sedimentary strata using sources or receivers in boreholes. Quiros et al. (2017) first applied VSP processing to aftershock recordings of the August 23 2011, 5.8 Mineral Virginia earthquake to produce high resolution 3D images of crustal structure in the hypocentral region of that event. In this study, we apply similar VSP approach to reflected phases on recordings of microearthquakes generated by geothermal activities near Krafla, Iceland, to image the underlying volcanic-geothermal system.

3.3 Data and Methods

Although Krafla has been the subject of a number of geophysical studies (e.g., Brandsdóttir and Menke 1992; Arnott and Foulger 1994; Darbyshire et al., 2000; Arnason et al., 2009), none detected the magma that was encountered during drilling. However, recently Kim et al., (2017) used microearthquake seismograms collected by a dense temporary array, deployed within a project named Deep Roots of Geothermal

systems (DRG) (Figure 3.2), to image the upper crust using seismic interferometry. This technique was based on redatuming surface ghost reflections from upgiong waves from microearthquakes to simulate surface source Common MidPoint (CMP) reflection profiles. Virtual reflection profiles produced seismic sections with reflections, some of which correspond to the position of the magma encountered in IDDP-1. Here we use the same dataset to produce 3D reflection images of the subsurface by applying the VSP methodology to seismic waves initially propagating downward from the microearthquake sources.

The DRG network consists of 20 three-component seismometers with Lennartz 0.2 Hz sensors installed on two profiles, one passing close to IDDP-1 (Figure 3.2a). Station spacing was 200 m and the data were sampled at 200 Hz (Figure 3.2a). The data were acquired over a two-month period (July to August) in 2014. Relatively continuous seismic activity was observed with average focal depths of about 2km. A total of 989 microearthquakes (magnitude M_L <2) were located using both temporary and permanent seismic stations (ISOR, 2014). A simple least-square-inversion based algorithm (Bratt and Bache, 1988) was applied with a prioiri velocity model from a refraction profile within and close to the caldera (blue, Figure 3.5d). We visually examined and selected the records of 120 events that showed clear coherent phases between the direct P and S wave arrivals (*e.g.,* Figure 3.2b). The horizontal and vertical uncertainties of locations of these events are on the order of 500m and 1km, respectively (personal communication, ISOR).

In order to minimize possible complications (*e.g.,* polarity changes) due to variations in focal mechanisms of the microearthquakes, we only included records in which the polarity of the prominent reflected phases was consistent among events. The selected recordings were then band-pass filtered between 2 and 16 Hz to emphasize body waves and normalized by the root-mean-square amplitude for each

microearthquake. Incorporation of higher frequencies resulted in traces too noisy to be useful in our analysis. The example shown in Figure 3.2b exhibits a strong coherent phase that arrives shortly after the direct P wave. As implied by its *PzP* label, we interpret this arrival as a reflection of downgoing energy from an interface beneath the hypocenter (Figure 3.3b). Here, we used vertical component records to minimize contributions from S wave energy, and leave similar treatment of S waves for future analysis.

The VSP technique has a long history in the oil exploration industry (Hardage, 2000). It is widely used to tie surface reflection profiles to lithology (Balch and Lee, 1984). It is usually done with sources at the surface and receivers in a borehole (Figure 3.3a). Alternatively, receivers can be placed at the surface and the sources placed in the borehole (reverse VSP or RVSP). If surface sources or receiver arrays extend away from the borehole, 2D and 3D reflection images can be made of the volume between them (Dillon and Thompson, 1984).

When multiple sources and/or multiple receivers are available, signal stacking can be applied. This is the basis of the well-known CMP reflection technique (Figure 3.3c) routinely applied to multichannel recordings of surface sources (Yilmaz, 2001). However, the raypaths associated with subsurface sources are more complex. The CMP assumption for reflection points is no longer valid and a more complicated Common Reflection Point (CRP) treatment is needed for effective signal stacking. Reflected energy from the subsurface source must be mapped into its correct reflection point in both space and time (*i.e.,* depth). For a constant velocity medium with horizontal interfaces (*e.g.,* Figure 3.3b), the following equations 3.1 and 3.2 define the mapped CRP location of x_i and z_i, respectively with a given time sample, t_i:

$$x_i = \frac{X_0}{2}\left(1 - \frac{d}{\sqrt{(t_i v)^2 - {X_0}^2}}\right) \tag{3.1}$$

$$z_i = \frac{1}{2}\left(\sqrt{(t_i v)^2 - {X_0}^2} + d\right) \tag{3.2}$$

where $\boldsymbol{X_0}$ is the lateral offset, $\boldsymbol{v}$, the velocity of a layer, and $\boldsymbol{d}$, depth of the source (Dillon and Thomson, 1984). The reflected energy in the RVSP geometry will map onto a curved path in 3D space. The blue curves in Figure 3.3 illustrate the mapping of reflection points from a source at depth (Figure 3.3a-b) as compared with the conventional CMP mapping for surface sources (Figure 3.3c). Energy from different sources (earthquakes) illuminating a given CRP can then be summed. Note that the CRP path for the RVSP geometry approaches that of the CMP as the depth of the reflecting interface increases.

We initially computed RVSP images using individual microearthquakes that show clear reflection phases. The reflection phases (*e.g., PzP*) of these microearthquakes were mapped into three dimensional CRP bins using a simplified 1D velocity model (Figure 3.5d) derived from a previous active source VSP survey (IMAGE, 2016) and stacked. The data were insufficient to robustly define a more complex 3D velocity model.

4.4 Results and discussion

Figure 3.4 shows examples of individual (single fold) images after application of RVSP moveout. These images represent the moveout-corrected traces of the subsection of the in-line and the cross-line profiles that are highlighted on the map view. The most prominent feature of these sections is a persistent, strong, subhorizontal reflector at a depth of about 2.4 km in the vicinity of the IDDP-1, slightly deeper than the depth of the magma encountered in the borehole (2.1 km). The apparent difference in depth (Figure 3.5a) is on the order of those expected from

uncertainties from earthquake locations and/or the velocity model used to convert time-to-depth. For example, a simple shift made to the location of earthquake #1 in Figure 3.5a would easily make a very close correspondence between the depth of the reflector and the depth at which magma was encountered in the IDDP-1 borehole (Figure 3.5b). Likewise, uncertainties in the appropriate velocity structure in the area will result in corresponding uncertainties in the depth of any reflector (Figure 3.5c). Given these uncertainties, it is reasonable to infer that the bright reflection appearing at 2.4 km on the RVSP image is from the same magmatic body encountered by IDDP-1 borehole. The data show that the reflector continues at least 1km westward from the well at roughly the same depth (Figure 3.4a). The magma interpretation is supported by the anomalous amplitude of this reflector (right-most panel in Figure 3.4). Local occurrences of unusually large reflection amplitudes are often referred to as "bright spots". Such bright spots were first associated with gas pockets in hydrocarbon reservoirs (*e.g.,* Sheriff, 1975) but the terminology has also been applied to anomalous reflections interpreted to be from magma bodies or magma related fluids (Brown et al., 1979; de Voogd et al., 1986; Brown et al., 1996; Kent et al., 2000). The high amplitudes in this case cannot be attributed to critical reflection as the angles of incidence involved are less than 20˚. Reflection polarity can sometimes be useful for discriminating a solid-liquid interface (*e.g.,* magma or brines) from a solid-solid interface with an unusually large seismic impedance contrast (Brown et al., 1996). A polarity reversal (*e.g.,* from positive to negative) is expected for a simple transition from solid to liquid. However, using polarity as a discriminant is in general difficult due to complicating factors such as interference of reflections from multiple interfaces, geometrical focusing, lateral velocity heterogeneity and source radiation patterns (*e.g.,* focal mechanisms). In this case, we found the polarity variations to be inconclusive.

Another prominent reflector is seen on the profiles in Figure 3.4b at a depth of

3.9km, well beneath the bottom of the boreholes. Again, the strong amplitude of this deep event is consistent with, if not confirmation of, a fluid reflector (e.g., magma, entrapped brines, steam, CO2, or SO2). This reflector lies near the edge of the attenuating body mapped during 1975-1984 Krafla rifting events (Eniarsson, 1978) as shown by purple lines in Figure 3.4. Other observations have been interpreted to suggest the existence of a simple magma chamber with its top near 3 km depth (*e.g.,* Brandsdóttir and Menke, 1992; Arnott and Foulger, 1994; Brandsdóttir et al., 1997). A recent MT and microseismic study also indicates the presence of magma chamber at similar depth (Friðleifsson et al., 2014). Furthermore, P wave reflections observed from the recent IMAGE VSP field campaign suggest the presence of magma at a depth of about 3.5 km. These observations thus support an interpretation of our 4 km reflector as the top of a magma accumulation. However, little apparent energy is shown at this depth on the profiles in Figure 3.4a. This suggests that whatever the reflector, it has piecemeal lateral continuity, inconsistent with a single, laterally extensive magma chamber.

CRP binning (50 x 50 m) of data from 120 selected microearthquakes was used to produce a stacked, 3D seismic volume (Figure 3.7). The bright reflector at 2.4 km is still prominent on the cross-line section, but less continuous on the in-line section than on the single fold sections. Optimal 3D reflection imaging requires recording of multiple sources with a dense 2D surface array to achieve adequate redundancy and uniform subsurface sampling (*e.g.,* Brown, 2011). However, we only have a pair of 2D recording profiles available. Since relatively few seismic stations were deployed along the in-line direction, the resulting images of the cross-line sections are generally higher quality than in-line sections. Reflections from 4 to 8 km depth are generally discontinuous and reverberatory. The reverberatory character could be due, at least in part, to errors in the earthquake source locations blurring the stacked image (*e.g.,*

Figure 3.5a-b), or perhaps to S wave contamination (*e.g.,* S-to-P converted phases). However, the 3D control provided by the crossing 2D lines argues against "sidewipe" (out of plane arrivals) as a major contributing factor. Note that the free-surface multiple (ghost) from the reflector at 2.1 km depth, which was used by Kim et al. (2017) for imaging via interferometry, would be expected to arrive at about 6km depth. However, no prominent event is evident at this depth, consistent with our expectation that while multiple energy might be present on the single fold sections, it should be degraded by the stacking process. We interpret the laterally discontinuous nature of the deeper reflections to be direct evidence of the discontinuous nature of the reflecting bodies themselves.

We interpret that the strongest reflections correspond to the large change in acoustic impedance that would be expected at a solid-to-fluid interface. The identity of the fluid is open to speculation. Magma is the most obvious candidate, but other magma related fluids (e.g. brines, steam, CO2, or SO2) could also be a factor (Makovsky et al., 1999). There is no clear evidence of a distinct "bottom" bright spot corresponding to any of these events. These could simply mean that the base of each fluid accumulation is too gradual to give rise to a reflection at these wavelengths. Alternatively, the fluid bodies may be thin, with the observed reflections being composites from the top and bottom of the unit. This latter interpretation is supported by the modeling of the seismic waveform shown in Figure 3.6, where an averaged trace of an earthquake cluster recorded by a single DRG station is compared with synthetic records generated by the SPECFEM2D code (Tromp et al., 2008). We modeled the reflection waveforms at the drilled magma depth with thickness varying from 25 to 1000 m (highlighted zone, Figure 3.6b). A distinct top and bottom (circled in blue) reflection is evident in the synthetics for the thicker magma layer models (*e.g.,* 100, 500 and 1000m). For smaller thicknesses, a composite waveform marks the

magma layer. Comparison of the observed seismic trace in Figure 3.6a with the synthetics in 3.6b suggests a) that p wave reflections from the bottom of a thick magma layer could be obscured by S waves, and b) that observed reflection which we interpret to be from the magma layer is a poor match to the synthetics for a composite layer if P waves alone are used. A better match is seen between the observed average trace in Figure 3.6a with the synthetic in Figure 3.6c, which includes converted phases from the two layers.

The stacked seismic sections (*e.g.,* Figure 3.7) indicate that the crust is characterized by a suite of strong, short reflectors, with no clear correlation to the overlying shallow bright spot that we associated with the drilled magma. A thick magma layer, whether shallow or deep, would be expected to strongly attenuate any through-going seismic waves, making observation of reflections, P or S, from either its base or underlying magma bodies problematic. We therefore speculate that the prominent, albeit discontinuous, reflectivity between 3 and 6 km on the stacked sections (Figure 3.7a) is evidence of a distributed magma system, rather than a simple large, upper crustal magma chamber at these depths beneath Krafla. The rift context, not to mention linear eruptive geometries like the Krafla-Fires, would suggest dikes as a major mode of emplacement. However, if these reflections were from the top of dikes, we might expect some indication of enhanced attenuation below and perhaps diffractions from the top "edges". These observed reflection segments instead suggest a series of sill-like, intermittent magma lenses at various depths (Figure 3.7d). 3D reflection depth slices could perhaps distinguish sill vs. dike geometries that may not be apparent in our 2D images. However, the uneven spatial coverage associated with the irregular source distribution coupled with the linear DRG profiles does not provide sufficient crossline coverage to clarify this issue. Of course a suite of sills on the reflection image implies a corresponding, and perhaps less seismically visible, set of

feeder dikes (*e.g.,* Figure 3.7d).

Distributed magma rather than large magma chambers has also been argued from seismic tomography (Tarazewicz et al., 2012; Jeddi et al., 2016), and microseismicity (Greenfield and White 2015). Cooper et al. (2016) interpreted petrological data from the 1975-1984 Krafla rifting events as not being products of crystallization from a large, single host liquid, but from diverse magma sources within the crust. As discussed by Cashman et al. (2017), the details of a distributed magma system may simply be too small to be resolved by many of the geophysical methods previously used to image the velocity and conductivity anomalies expected from such a distribution. Marjanovic et al. (2014) have likewise argued that the concept of a "mush" volume at fast and intermediate spreading-rate ridges (Detrick et al., 1987; Kent and Orcutt, 1993) has been challenged both by newer, high resolution seismic reflection data as well as analogy to mapping of exposed sections of former oceanic crust, both of which indicates the "mush zone" is a complex suite of sill-like magma lenses.

As described earlier, the seismometer array used in this experiment is not a true 3D recording deployment, which would involve an areal grid of instruments at comparably dense spacing in both dimensions (*e.g.,* Walton, 1972). Our images do not uniformly sample the subsurface in 3D space. Such a restricted surface coverage undoubtedly limits the quality of the resulting image and introduces ambiguity in interpretation of structural details. An adequate areal array would require the deployment of hundreds of seismometers. Such a "large N" array for passive recording has recently become more feasible by the development of nodal recordings systems by the oil exploration industry (*e.g.,* Lin et al., 2013).

Other factors may further limit the image quality. For example, the RVSP technique requires accurate knowledge of earthquake location and origin time. Source location

errors may blur reflections on stacked images (Figure 3.7). We note that "large N" arrays would also provide more precise determination of both subsurface velocity variations (Davenport et al, 2015) and hypocentral locations (e.g. Quiros et al., 2015).Variations in amplitude of the downgoing waves due to variations in the source magnitude and focal mechanism can cause destructive or constructive interference when stacked. Contributions from S or converted phases, if present, could obscure or masquerade as P wave reflection energy. However, the near vertical geometry of reflection raypaths from the earthquakes to the DRG stations argues against significant *SzS* or mode converted reflections. Complications due to variations in the source function (rupture history) are likely to be minimal since the magnitude of the microearthquakes is quite small.

3.5 Conclusions

We adapt conventional VSP techniques to image reflectors beneath the Krafla geothermal field using microearthquakes associated with geothermal activity in the upper crust. An unusually strong reflector is mapped at the depth corresponding to the magma encountered by the by IDDP-1 drillhole. Similar strong coherent reflectors at depths ranging from 4 to 6 km are likewise interpreted as magma bodies. Although 4 km corresponds to the top of a magma reservoir previously inferred from lower resolution geophysics, the reflection image indicates a distributed system of smaller magma sills rather than a large pervasively molten feeder chamber. Exploiting earthquakes as sources in RVSP imaging is attractive because it can yield resolution comparable to controlled source CMP reflection imaging without the cost or limitations of artificial sources. Lower cost may also translate into feasibility of time lapse reflection imaging with special relevance to monitoring active subsurface processes such as magma movement and volcanism. The availability of new "large N"

passive seismic array technology makes this technique a powerful new tool for imaging geothermal systems.

3.6 Figures

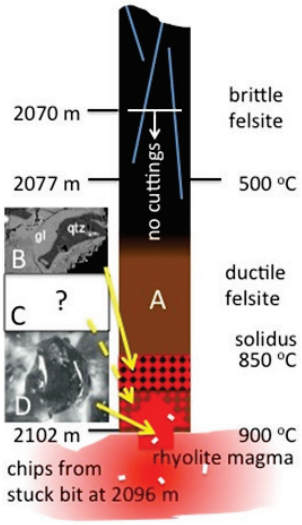

Figure 3.1: Lithologic zones of the magma body encountered by IDDP-1. Expected sequence of roof (A), melting roof (B), crystallizing magma (C), and uncooled magma (D). Pieces of B fell onto drill bit and D flowed around bit when stuck at depth of 2096 m. Note C was missed because it was below the bit. Figure courtesy of John Eichelberger, University of Alaska Fairbanks

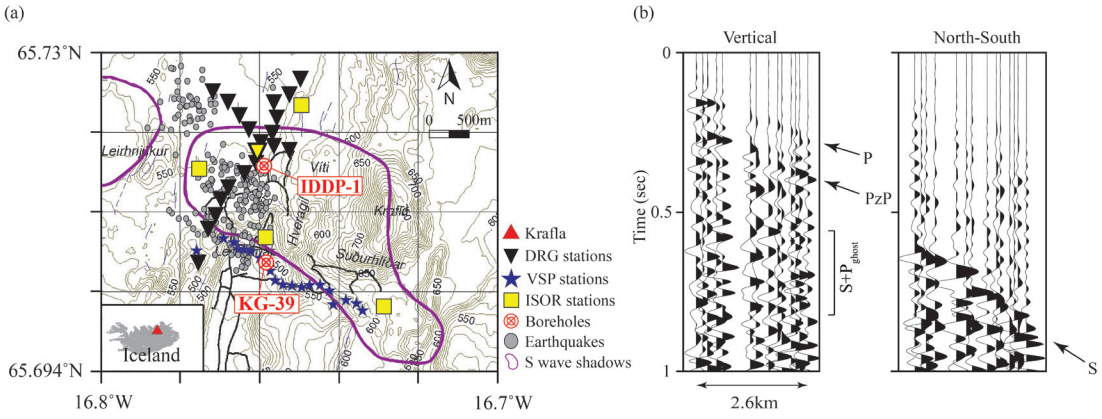

Figure 3.2. (a) Study area in the Krafla geothermal field showing the locations of the IDDP-1 and KG-39 boreholes (red circles) within the DRG seismic network (black triangles). Note VSP stations used in the IMAGE field campaign (blue stars) and permanent ISOR stations (yellow squares). Microearthquakes discussed in the main

text are illustrated with gray circles. Purple lines indicate boundaries of regions where high S wave attenuation was mapped during 1975-1984 Krafla rifting events (Eniarsson, 1978). The DRG station highlighted in yellow was used for the waveform analysis in Figure 3.6. (b) A sample microearthquake recording from DRG network. A reflected phase (*PzP*) is evident between P and S wave.

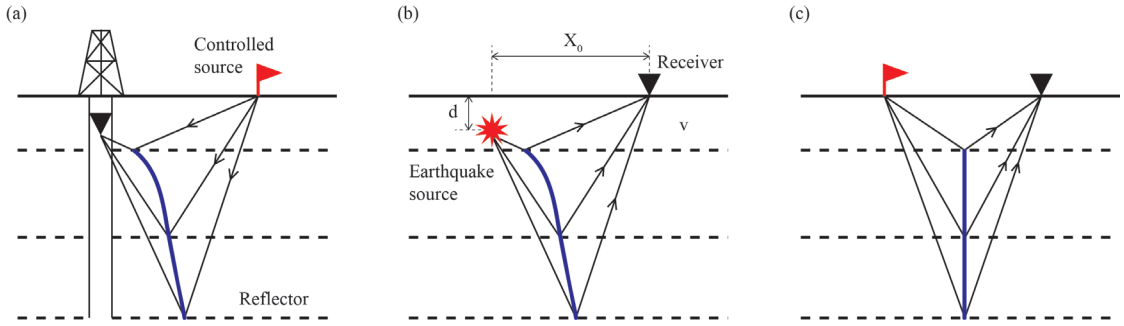

Figure 3.3. (a) Representative raypath geometry for conventional VSP survey, (b) RVSP using earthquake as a source, and (c) conventional surface source (CMP) seismic reflection survey.

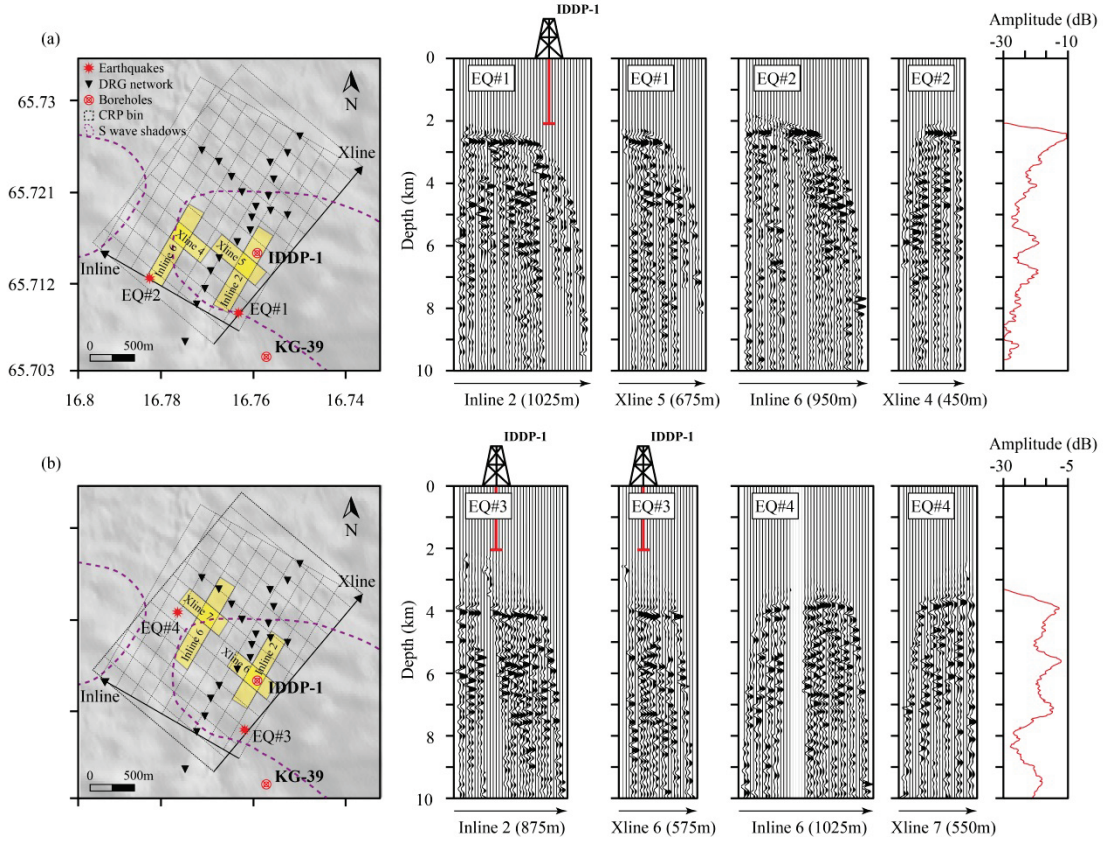

Figure 3.4. RVSP images using individual microearthquakes. Seismic traces correspond to the highlighted CRP bins on the map. To maximize stacking fold within the bins, two separate grids are made that are parallel to the seismic arrays. Red

vertical lines displayed on RVSP images represent the depth of the drilled magma by IDDP-1 borehole. Two distinct reflectors are evident: (a) a reflector at 2.4km depth where magma was encountered by IDDP-1 and (b) a deeper reflector at a depth of about 3.9km. The seismic sections are displayed with horizontal exaggeration of 4 to 1. Amplitude decay curves at right were computed as $20log_{10}(amplitude)$ of the average trace.

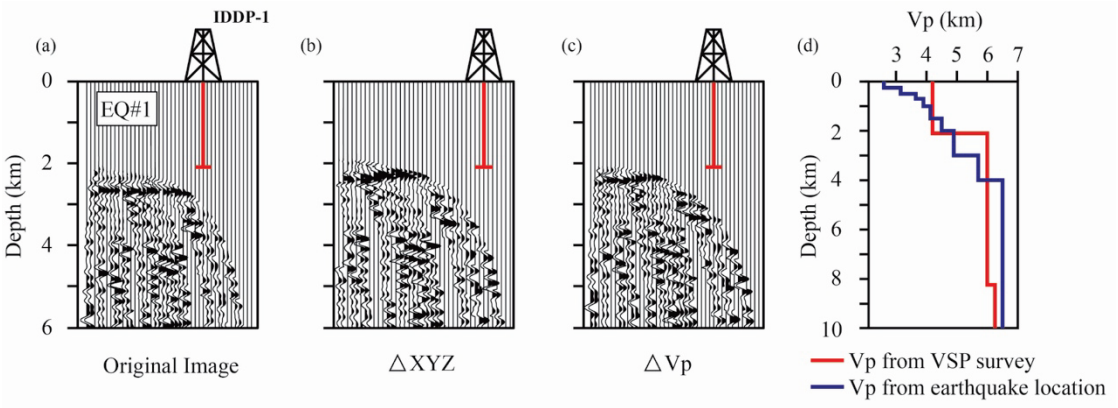

Figure 3.5. Correlation of seismic image with IDDP-1 borehole position of known magma. Red vertical lines displayed in (a)-(c) represent the depth of the drilled magma by IDDP-1 borehole. (a) RVSP image using reported hypocenter of earthquake #1 as shown in Figure 3a. (b) RVSP image after shifting the location of earthquake #1 by 250m, 180m, and 330m in latitude, longitude and depth, corresponding to the reported position uncertainties for this event, respectively. (c) RVSP image produced by the velocity model indicated in blue instead of that derived from the VSP survey (d). (d) Velocity variations derived from the local VSP survey (red) compared with those used for inverting the microearthquake locations (blue).

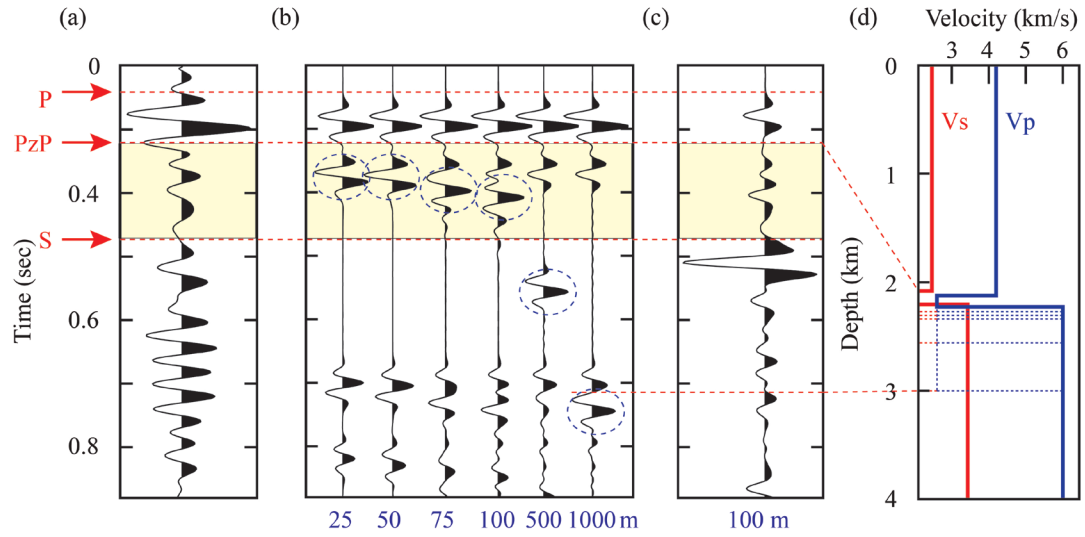

Figure 3.6. Comparison of the observed bright spot reflection from shallow (ca 2 km)

feature in data with synthetic responses from a simple magma layer. (a) The average amplitude of recordings from five adjacent earthquakes as recorded by a single DRG station (yellow triangle, Figure 1a). This average trace has been filtered by the same 2-16 Hz filter used in our previous described analyses. Note that the amplitude of the S wave is subdued by destructive interference from stacking. (b) Synthetic seismograms produced by a 10 Hz Ricker wavelet propagating through the acoustic model shown as blue line in (d). Blue circles indicate P wave reflections from the base of magma layer on the synthetic traces. (c) Same as a 100m thick magma layer in (b) with full waveforms containing both P and S waves. The highlighted zone is bounded by the theoretical arrival times of *PzP* and S wave in the model. (d) Velocity models used in (b) and (c). Dotted lines correspond to different thickness of the low velocity layered used in (b) and (c), as shown at the bottom of each trace. The assumed P wave velocity for the magma body is based on the lab measurements of Murase and Mcbirney, 1973.

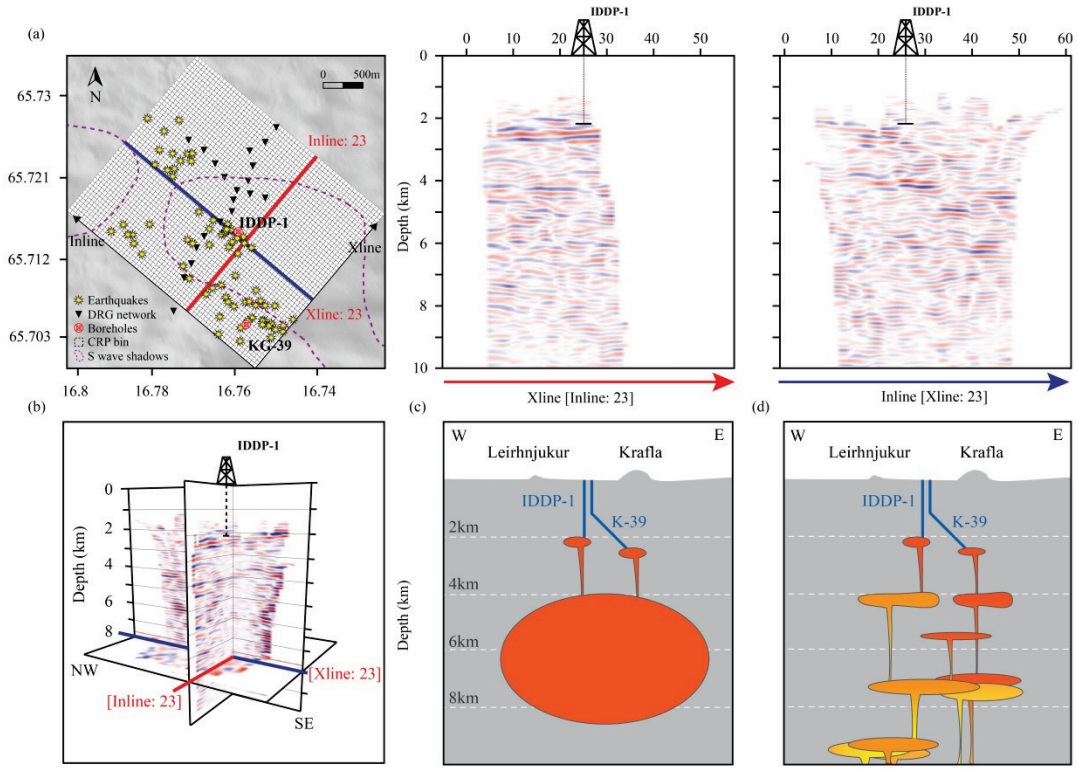

Figure 3.7. (a) 3D RVSP stack using 120 earthquakes. Red and blue lines on map to the left indicate the layout of the vertical seismic sections to the right. Earthquake locations are indicated with yellow stars. The seismic sections are displayed with horizontal exaggeration of 3 to 1. (b) 3D fence display of the images in 3.7a. (c) and (d) Two contrasting concepts of magma beneath Krafla: a large volume of pervasively molten magma vs. a distributed suite of smaller magma accumulations. The different colors are intended to suggest different generations of intrusion.

REFERENCES

Árnason, K., Vilhjálmsson, A.M., Björnsdóttir, Þ., 2009. A Study of the Krafla Volcano Using Gravity, Micro Earthquake and MT Data. Iceland GeoSurvey Report ÍSOR-2009/067, Reykjavik, Iceland, 66 pp.

Árnason, K., Eysteinsson, H., & Hersir, G. P. (2010). Joint 1D inversion of TEM and MT data and 3D inversion of MT data in the Hengill area, SW Iceland. Geothermics, 39(1), 13–34.

Arnott, S. K., and G. R. Foulger (1994), The Krafla spreading segment, Iceland: 1. Three-dimensional crustal structure and the spatial and temporal distribution of local earthquakes, Journal of Geophysical Research: Solid Earth, 99(B12), 23801–23825.

Balch, A. H., & Lee, M. W. (1984). Vertical seismic profiling: Technique, applications, and case histories. IHRDC Press, Boston, MA,

Balch, R. S., Hartse, H. E., Sanford, A. R., & Lin, K. (1997). A new map of the geographic extent of the Socorro mid-crustal magma body. Bulletin of the Seismological Society of America, 87(1), 174–182.

Björnsson, A., & Saemundsson, K. (1977). Current rifting episode in north Iceland. Nature, 266, 318–323.

Brandsdóttir, B., and W. H. Menke (1992), Thin low-velocity zone within the krafla caldera, ne-Iceland attributed to a small magma chamber, Geophysical research letters, 19(24), 2381–2384.

Brandsdóttir, B., W. Menke, P. Einarsson, R. S. White, and R. K. Staples (1997), Färoe-Iceland Ridge Experiment 2. Crustal structure of the Krafla central volcano, Journal of Geophysical Research: Solid Earth, 102(B4), 7867–7886.

Brenguier, F., Shapiro, N. M., Campillo, M., Nercessian, A., & Ferrazzini, V. (2007). 3-D surface wave tomography of the Piton de la Fournaise volcano using seismic noise correlations. Geophysical Research Letters, 34(2).

Brown, A. R. (2011). Interpretation of three-dimensional seismic data. Society of Exploration Geophysicists and American Association of Petroleum Geologists. Retrieved from http://library.seg.org/doi/pdf/10.1190/1.9781560802884.index

Brown, L. D., P. A. Krumhansl, C. E. Chapin, A. R. Sanford, F. A. Cook, S. Kaufman, J. E. Oliver, and F. S. Schilt (1979), COCORP seismic reflection studies of the Rio Grande rift, Rio Grande rift: Tectonics and magmatism, 169–184.

Brown, L. D., W. Zhao, K. D. Nelson, M. Hauck, D. Alsdorf, A. Ross, M. Cogan, M.

Clark, X. Liu, and J. Che (1996), Bright spots, structure, and magmatism in southern Tibet from INDEPTH seismic reflection profiling, Science, 274(5293), 1688–1690.

Byerly, K., Brown, L., Voight, B., & Miller, V. (2010). Reflection imaging of deep structure beneath Montserrat using microearthquake sources. Geophysical Research Letters, 37(19).

Cashman, K. V., Sparks, R. S. J., & Blundy, J. D. (2017). Vertically extensive and unstable magmatic systems: A unified view of igneous processes. Science, 355(6331), eaag3055.

Cassidy, J. F. (1992). Numerical experiments in broadband receiver function analysis. Bulletin of the Seismological Society of America, 82(3), 1453–1474.

Comeau, M. J., Unsworth, M. J., Ticona, F., & Sunagua, M. (2015). Magnetotelluric images of magma distribution beneath Volcán Uturuncu, Bolivia: Implications for magma dynamics. Geology, 43(3), 243–246.

Cooper, K. M., Sims, K. W., Eiler, J. M., & Banerjee, N. (2016). Timescales of storage and recycling of crystal mush at Krafla Volcano, Iceland. Contributions to Mineralogy and Petrology, 171(6), 54.

Darbyshire, F. A., K. F. Priestley, R. S. White, R. Stefánsson, G. B. Gudmundsson, and S. S. Jakobsdóttir (2000), Crustal structure of central and northern Iceland from analysis of teleseismic receiver functions, Geophysical Journal International, 143(1), 163–184.

Davenport, K. K., Hole, J. A., Quiros, D. A., Brown, L. D., Chapman, M. C., Han, L., & Mooney, W. D. (2014). Aftershock imaging using a dense seismometer array (AIDA) after the 2011 Mineral, Virginia, earthquake. Geological Society of America Special Papers, 509, SPE509–15.

Detrick, R. S., Buhl, P., Vera, E., Mutter, J., Orcutt, J., Madsen, J., & Brocher, T. (1987). Multi-channel seismic imaging of a crustal magma chamber along the East Pacific Rise. Nature, 326(6108), 35–41.

Dillon, P. B., and R. C. Thomson (1984), Offset source VSP surveys and their image reconstruction, Geophys. Prospect., 32(5), 790–811.

Einarsson, P. (1978), S-wave shadows in the Krafla caldera in NE-Iceland, evidence for a magma chamber in the crust, Bull. Volcanol., 41(3), 187–195.

Einarsson, P. (1991). The Krafla rifting episode 1975–1989. Náttúra Myvatns,(The Nature of Lake Myvatn), 97–139.

Elders, W. A., Friḥleifsson, G., & Albertsson, A. (2014a). Drilling into magma and the implications of the Iceland Deep Drilling Project (IDDP) for high-temperature geothermal systems worldwide. Geothermics, 49, 111–118.

Elders, W. A., G. Ó. Friḥleifsson, and B. Pálsson (2014b), Iceland Deep Drilling Project: The first well, IDDP-1, drilled into magma, Geothermics, (49), 1.

Friðleifsson, G. Ó., Ármannsson, H., Guðmundsson, Á., Árnason, K., Mortensen, A. K., Pálsson, B., & Einarsson, G. M. (2014). Site selection for the well IDDP-1 at Krafla. Geothermics, 49(Supplement C), 9–15.

Greenfield, T., & White, R. S. (2015). Building icelandic igneous crust by repeated melt injections. Journal of Geophysical Research: Solid Earth, 120(11), 7771–7788.

Hardage, B. A. (2000), Vertical Seismic Profiling: Principles, Handbook of Geophysical Exploration: Seismic Exploration, 3rd ed., edited by K. Helbigand S. Treitel, Elsevier Science, Oxford, U. K.

Hasegawa, A., & Yamamoto, A. (1994). Deep, low-frequency microearthquakes in or around seismic low-velocity zones beneath active volcanoes in northeastern Japan. Tectonophysics, 233(3), 233–252.

ISOR (2014), Seismic Monitoring at Krafla: For the Period of October 2013 to October 2014, Project no: 14-0089.

IMAGE (2016), IMAGE-D4.02 – Summary report of WP 4.02: Active Seismic with VSP.

Inamori, T., Horiuchi, S., & Hasegawa, A. (1992). Location of mid-crustal reflectors by a reflection method using aftershock waveform data in the focal area of the 1984 Western Nagano Prefecture Earthquake. Journal of Physics of the Earth, 40(2), 379–393.

Inbal, A., R. W. Clayton, and J.-P. Ampuero (2015), Imaging widespread seismicity at midlower crustal depths beneath Long Beach, CA, with a dense seismic array: Evidence for a depth-dependent earthquake size distribution, Geophysical Research Letters, 42(15), 6314–6323.

Jaxybulatov, K., Shapiro, N. M., Koulakov, I., Mordret, A., Landès, M., & Sens-Schönfelder, C. (2014). A large magmatic sill complex beneath the Toba caldera. Science, 346(6209), 617–619. https://doi.org/10.1126/science.1258582

Jeddi, Z., Tryggvason, A., & Gudmundsson, Ó. (2016). The Katla volcanic system

imaged using local earthquakes recorded with a temporary seismic network. Journal of Geophysical Research: Solid Earth, 121(10), 2016JB013044. https://doi.org/10.1002/2016JB013044

Kent, G. M., Harding, A. J., & Orcutt, J. A. (1993). Distribution of magma beneath the East Pacific Rise between the Clipperton transform and the 9 17′ N deval from forward modeling of common depth point data. Journal of Geophysical Research: Solid Earth, 98(B8), 13945–13969.

Kent, G. M. et al. (2000), Evidence from three-dimensional seismic reflectivity images for enhanced melt supply beneath mid-ocean-ridge discontinuities, Nature, 406(6796), 614–618.

Kim, D., Brown, L. D., Árnason, K., Águstsson, K., and Blanck, H. (2017). Magma reflection imaging in Krafla, Iceland, using microearthquake sources. Journal of Geophysical Research: Solid Earth, 122, 5228–5242.

Lees, J. M. (2007). Seismic tomography of magmatic systems. Journal of Volcanology and Geothermal Research, 167(1), 37–56.

Lin, F.-C., D. Li, R. W. Clayton, and D. Hollis (2013), High-resolution 3D shallow crustal structure in Long Beach, California: Application of ambient noise tomography on a dense seismic array, Geophysics, 78(4), Q45–Q56.

Makovsky, Y., Klemperer, S. L., Ratschbacher, L., & Alsdorf, D. (1999). Midcrustal reflector on INDEPTH wide-angle profiles: An ophiolitic slab beneath the India-Asia suture in southern Tibet? Tectonics, 18(5), 793–808.

Marjanović, M., Carbotte, S. M., Carton, H., Nedimović, M. R., Mutter, J. C., & Canales, J. P. (2014). A multi-sill magma plumbing system beneath the axis of the East Pacific Rise. Nature Geoscience, 7(11), 825–829.

Matsumoto, S., and A. Hasegawa (1996), Distinct S wave reflector in the midcrust beneath Nikko-Shirane volcano in the northeastern Japan arc, Journal of Geophysical Research: Solid Earth, 101(B2), 3067–3083.

Mortensen, A. K., Grönvold, K., Guḥmundsson, A., Steingrímsson, B., & Egilson, T. (2010). Quenched silicic glass from well K-39 in Krafla, North-Eastern Iceland. In proceedings world geothermal congress, Bali, Indonesia.

Sanford, A. R., and L. T. Long (1965), Microearthquake crustal reflections, Socorro, New Mexico, Bulletin of the Seismological Society of America, 55(3), 579–586.

Sanford, A. R., Ö. Alptekin, and T. R. Toppozada (1973), Use of reflection phases on microearthquake seismograms to map an unusual discontinuity beneath the Rio

Grande rift, Bulletin of the Seismological Society of America, 63(6–1), 2021–2034.

Schuler, J., Greenfield, T., White, R. S., Roecker, S. W., Brandsdóttir, B., Stock, J. M., … Pugh, D. (2015). Seismic imaging of the shallow crust beneath the Krafla central volcano, NE Iceland. Journal of Geophysical Research: Solid Earth, 120(10), 7156–7173.

Sheetz, K. E., & Schlue, J. W. (1992). Inferences for the Socorro magma body from teleseismic receiver functions. Geophysical Research Letters, 19(18), 1867–1870.

Sheriff, R. E. (1975). Factors affecting seismic amplitudes. Geophysical Prospecting, 23(1), 125–138.

Sparks, R. S. J., & Cashman, K. V. (2017). Dynamic Magma Systems: Implications for Forecasting Volcanic Activity. Elements, 13(1), 35–40.

Sveinbjornsdottir, A. E., Coleman, M. L., & Yardley, B. W. D. (1986). Origin and history of hydrothermal fluids of the Reykjanes and Krafla geothermal fields, Iceland. Contributions to Mineralogy and Petrology, 94(1), 99–109.

Quiros, D., Brown, L. D., Cabolova, A., Chen, C., Davenport, K., Hole, J., … Mooney, W. (2015). Reflection imaging using earthquake sources: A novel application of reverse vertical seismic profiling (RVSP). In SEG Technical Program Expanded Abstracts 2015 (pp. 5565–5569). Society of Exploration Geophysicists.

Quiros, D. A., Brown, L. D., Davenport, K. K., Hole, J. A., Cabolova, A., Chen, C., … Mooney, W. D. (2017). Reflection imaging with earthquake sources and dense arrays. Journal of Geophysical Research: Solid Earth, 122(4), 2016JB013677. https://doi.org/10.1002/2016JB013677

Unsworth, M. J., Jones, A. G., Wei, W., Marquis, G., Gokarn, S. G., Spratt, J. E., … others. (2005). Crustal rheology of the Himalaya and Southern Tibet inferred from magnetotelluric data. Nature, 438(7064), 78–81.

de Voogd, B., L. Serpa, L. Brown, E. Hauser, S. Kaufman, J. Oliver, B. W. Troxel, J. Willemin, and L. A. Wright (1986), Death Valley bright spot: A midcrustal magma body in the southern Great Basin, California?, Geology, 14(1), 64–67.

Waite, G. P., Smith, R. B., & Allen, R. M. (2006). VP and VS structure of the Yellowstone hot spot from teleseismic tomography: Evidence for an upper mantle plume. Journal of Geophysical Research: Solid Earth, 111(B4).

Walton, G. G. (1972). Three-dimensional seismic method. Geophysics, 37(3), 417–430.

Wei, W., Unsworth, M., Jones, A., Booker, J., Tan, H., Nelson, D., Chen, L., Li, S., Solon, K., Bedrosian, P., Jin, S., Deng, M., Ledo, J., Kay, D., and B. Roberts (2001). Detection of widespread fluids in the Tibetan crust by magnetotelluric studies. Science, 292(5517), 716–719.

Wilson, D., Aster, R., West, M., Ni, J., & others. (2005). Lithospheric structure of the Rio Grande rift. Nature, 433(7028), 851.

Yilmaz, Ö. (2001) Seismic Data Analysis: Society of Exploration Geophysicists.

Zandt, G., M. Leidig, J. Chmielowski, D. Baumont, and X. Yuan (2003), Seismic detection and characterization of the Altiplano-Puna magma body, central Andes, Pure and Applied Geophysics, 160(3–4), 789–807.

Zierenberg, R. A., Schiffman, P., Barfod, G. H., Lesher, C. E., Marks, N. E., Lowenstern, J. B., … others. (2013). Composition and origin of rhyolite melt intersected by drilling in the Krafla geothermal field, Iceland. Contributions to Mineralogy and Petrology, 165(2), 327–347.

CHAPTER 4

ENHANCED RESOLUTION OF THE SUBDUCTING PLATE INTERFACE IN CENTRAL ALASKA FROM AUTOCORRELATION OF LOCAL EARTHQUAKE CODA

4.1 Abstract

The physical properties of subduction interfaces at convergent plate boundaries impact megathrust seismicity and arc volcanism, but remain incompletely understood. Slabs below 10 km depth are primarily imaged using phases from teleseismic earthquakes below 1 Hz, resulting in low-resolution images compared to observed fault-zone scales. Here we image the subducting Yakutat oceanic plateau in Alaska using scattered body wave arrivals in local earthquake coda and produce a higher frequency image of the slab. Though both autocorrelation and teleseismic receiver functions image interfaces that we associate with a low-velocity zone atop the subducting oceanic plate, the autocorrelation results suggest that seismic velocity decreases within the low-velocity zone. Our results, though limited in resolution by station spacing, provide one of the first coherent structural images of the mantle using scattered local body waves. Similar methodologies using dense stations could provide higher resolution images and advance characterization of subduction plate boundaries globally.

4.2 Introduction

The association of great earthquakes and thrust faulting along megathrust plate boundaries is well established (Dixon and Moore, 2007). However, key questions regarding the processes that control rupture initiation, propagation and termination remain unanswered. Improving the resolution of seismic imaging at depths of several tens of kilometers could significantly advance knowledge of controls on tectonic

The material in Chapter 4 will shortly be submitted under Kim et al., Enhanced resolution of the subducting plate interface in central Alaska from autocorrelation of local earthquake coda. *Geophysical Research Letters (2018)*

process by improving our knowledge of the thrust zone and physical properties at plate boundaries, particularly the downdip end of the megathrust where great earthquakes nucleate and tremor occurs (*e.g.,* Schwartz and Rokosky, 2007; Lay et al., 2012). As an example, fault damage zones mapped in the field from exhumed megathrusts are on the order of hundreds of meters thick (Rowe et al., 2013), but receiver functions image channels of a few kilometers in thickness at the plate boundary (Audet et al., 2009). Active-source seismic methods are able to image plate boundaries in high resolution and define structures within the shallow part of the seismogenic zone on scales of tens of meters (*e.g.,* Li et al., 2015; Bécel et al., 2017), but signal penetration and streamer length often limit controlled-source techniques at greater depth in subduction zones. The relationship between the thinner, exhumed damage zone and the thicker seismically imaged channel, and how each impacts seismogenesis, is not understood.

Seismic images of the subduction interface are commonly created using using teleseismic conversions from boundaries, commonly known as "receiver functions" (*e.g.,* Burdick and Langston, 1977). Receiver functions in Alaska delineate the subducted plate and the upper plate (*e.g.,* Ferris et al., 2003; Kim et al., 2014), and show a 2-5 km thick low-velocity zone (LVZ) at the top of subducting crust. Receiver functions in northern Cascadia also indicate a LVZ, 3.4 ± 1.0 km thick with high Vp/Vs ratios (>2.0) immediately above subducting crust (Audet et al., 2009; Hansen et al., 2012), interpreted as an over-pressured channel at the subducting plate interface. Receiver function images elsewhere show subducting crust as a low velocity layer but do not always resolve an overlying LVZ (see compilation of Bostock, 2013). Teleseismic P-wave energy used in these studies is dominantly at frequencies < 1 Hz with corresponding wavelengths > 5-10 km, so receiver functions are not capable of resolving thin layers. Using free-surface multiples can improve resolution by a factor of 3-5 (Rondenay, 2001) but typical signals still cannot resolve structures smaller than

~2 kilometers. Other methods to image slabs, such as seismic tomography, are limited in resolution and features smaller than ~10 km cannot be resolved even with dense networks (*e.g.,* Tsuji et al., 2008; Kato et al., 2010). Seismic interferometric methods, using cross-correlations of seismic traces between station pairs, have been used in subduction zones using regional (Ito and Shiomi, 2012) and teleseismic earthquakes (Ruigrok and Wapenaar, 2012) or from ambient noise (Nishitsuji et al., 2016), but the results have been challenging to interpret unequivocally.

Given these limitations, local earthquake sources with frequencies 10 Hz and greater energy than active sources provide a potential means to image small-scale slab structure at high resolution to depths through the seismogenic zone. In this study, we show that reflected and converted seismic waves within the coda of local earthquakes are capable of mapping slab structure in higher resolution than receiver functions. We use data from the 2007-2008 MOOS network (Multidisciplinary Observations of Subduction; Figure. 4.1a) in central Alaska, selecting local earthquakes (Li et al., 2013) with near-vertical raypaths. We successfully show that autocorrelation of scattered energy within local earthquake coda provides higher-resolution images of the subducting Yakutat slab in central Alaska as compared to receiver functions, beginning to bridge the gap towards passive imaging of features at the scale of damage zones along plate boundaries. We generate synthetic autocorrelation data, using the SPECFEM2D finite difference code (Tromp et al., 2008), to demonstrate the ability of the method to image higher-resolution structure of subsurface interfaces beneath dense arrays. Improving our imaging and understanding of the subducting interface will better establish physical models of megathrusts.

4.3 Background

4.3.1 Study Area

The central Alaska subduction zone hosted one of the world's largest recorded earthquakes, the 1964 Prince William Sound Mw9.2 earthquake (Ichinose et al., 2007). The shallow dip of the subducting Pacific plate in this region creates an interplate coupled zone up to 250 km wide (e.g., Plafker, 1965), and a portion of the slip area of the 1964 earthquake is below land (Figure. 4.1a). In the region of low plate dip, the buoyant and thick crust of the Yakutat terrane subducts, an oceanic plateau (*e.g.,* Plafker et al., 1994; Christeson et al., 2010; Worthington et al., 2012). At the subduction interface in central Alaska, a LVZ has been imaged using receiver function migration from the MOOS data (Kim et al., 2014), constrained to be 2-5 km thick. The LVZ is suggested to represent either marine sediment transported into the subduction system (*e.g.,* von Huene and Weinrebe, 2012), a zone of high fluid pressure at the top of subducting crust (*e.g.,* Christensen, 1996), or another manifestation of the megathrust fault zone (*e.g.,* Nedimović et al., 2003). The thickness of this LVZ is an order of magnitude greater than the damage zone observed in the geological record within exhumed megathrusts nearby in Alaska, on the order of hundreds of meters thick (Rowe et al., 2013).

4.3.2 Extraction of Body Waves Using Seismic Interferometry

In recent years, methods of seismic interferometry have developed, cross-correlating seismic traces between two independent stations. Studies using interferometry now routinely extract surface waves from ambient microseismic noise (*e.g.,* Shapiro et al., 2005; Lin et al., 2008), commonly for seismic tomography. Interferometry has also been applied in attempts to extract body waves from ambient noise (*e.g.,* Roux et al., 2005; Draganov et al., 2009; Zhan et al., 2010; Ryberg, 2011; Lin et al., 2013), and from discrete sources including in exploration seismology (*e.g.,* Wapenaar et al., 2008; Schuster, 2009) and in studies using local or teleseismic earthquakes (*e.g.,* Ruigrok and Wapenaar 2012; Nakata et al., 2014; Kim et al., 2017).

However, distinct boundaries have commonly been difficult to image in results of interferometric studies, particularly within the mantle, and the method is not commonly used for structural imaging.

4.4 Data

We use seismic data from 16 stations within the MOOS network (Li et al., 2013) and AK network station RCO1 (Alaska Earthquake Center, 1987), forming an approximately north-south transect at ~10-15 km spacing over the shallowly dipping slab (Figure. 4.1a). MOOS data were acquired using broadband seismometers for 13 months from August 2007 to August 2008 with a sample rate of 50 sps. Local and teleseismic earthquakes recorded by stations on this transect are used for autocorrelation and receiver function analyses, respectively.

For autocorrelation, we use local earthquakes from the double-difference catalog of Li et al. (2013). We subset the catalog to 1542 of 8308 earthquakes by choosing events with epicenters within 20 km of a station, to limit raypaths to those with energy scattered from boundaries nearly-vertically beneath each station. We further subset the earthquakes based on the quality of the autocorrelation result, using 763 earthquakes in our final result (Figure. 4.1d), ranging in depth from 5 to 80 km (Figure 4.2). Magnitudes (M_L) range from -0.16-4.1. For autocorrelation of noise, we use time windows directly before each local earthquake. Unfiltered data from time windows with local earthquakes have two distinct peaks in power, at ~0.2 Hz and at ~7 Hz; data from the noise windows have one distinct peak in power at ~0.2 Hz (Figure. 4.1c). For receiver functions, we selected teleseismic earthquakes of magnitude greater than M_b 6.0 within epicentral distances of 30˚ to 90˚, a total of 80 earthquakes (Inset, Figure. 4.1a).

4.5 Methods

4.5.1 Autocorrelation of Local Earthquake Recordings from MOOS data

Local earthquakes provide discrete sources of energy and create direct arrivals and reflections, conversions, and reverberations from subsurface boundaries either above or below the source (Figure 4.3a-b). The timing of reverberations within the earthquake coda is a function of boundary depth and seismic wavespeed, as in surface seismic reflection data, and thus contains similar information on subsurface boundary structure (*e.g.,* Claerbout, 1968). The reverberations are weak in amplitude and coherent signals are masked by noise, however, variability in earthquake location and depth, and variable source signatures preclude direct stacking of local earthquake traces (Figure 4.3d-e). Autocorrelation of local earthquake data facilitates stacking by removing the source signature and by aligning traces on the direct arrival from each source, temporally aligning later reverberations for rays with similar incidence angle (Figure 4.3c), and allowing stacking of earthquake coda (Figure 4.3f).

To create autocorrelation traces of local earthquakes in our study, we extract traces beginning 20 seconds before and ending 100 seconds after the predicted P arrival for each selected earthquake at each station. This time window encompasses the direct P- and S-waves and later reverberations from the boundaries of interest above and below the subducting crust. We separately analyze the vertical (Z), north (N), and east (E) components. Prior to autocorrelation, we remove the mean and the trend from each trace and apply a bandpass filter from 0.05 to 1 Hz. Though the higher dominant frequency of the local earthquake energy includes energy at 10 Hz (*e.g.,* Figure 4.1c), these frequencies are spatially aliased at our station spacing of 10-15 km (Figure 4.6d-e). For our analysis, we thus utilize the energy within the lower spectral peak; the relationship between station spacing, frequency, and resolution is covered in the discussion. One-bit normalization of traces before autocorrelation is not required in our dataset to see primary arrivals but enhances the phases and was thus applied in our processing flow. Traces from each earthquake-station combination are

autocorrelated using a 60-second time window. Following autocorrelation, the traces were visually inspected at each station to eliminate those dominated by ringing of the autocorrelation or other noise. After removing low signal-to-noise traces, we apply an automatic-gain-control (AGC) function with a time window of 8.0 s to increase the relative amplitude of later phases. The resulting traces at each station are then linearly stacked to enhance coherent reverberations, and to suppress energy from depth phases which vary in timing between events (Figure 4.3). The number of earthquake sources used per station stack ranged from 13 to 152 (Table 4.1). Finally, we correct for the polarity reversal caused by the free-surface reflection by reversing the polarity of each stacked trace. Results are displayed as a record section along our north-south MOOS transect (Figure 4.5).

For the noise processing, we extract data from 130 to 10 seconds before the P arrival for each earthquake. We follow all other processing steps used in the processing of the earthquake coda, although we stack all waveforms rather than inspect each trace.

4.5.2 Synthetic Record Section Using Autocorrelation of Modeled Local Earthquakes

We use the SPECFEM2D code (Tromp et al., 2008) and available a priori structural information from earlier MOOS results (Li et al., 2013; Kim et al., 2014, Figure 4.1b) to model synthetic local earthquake waveforms from 38 hypocentral locations, one above and one below the LVZ for each station (Figure 41d). The input 2D velocity model (Figure 4.1d) includes, notably, the 5-km thick LVZ suggested by receiver function modeling (Kim et al., 2014). Beneath the LVZ are subducting Yakutat crust (15 km thick) and upper mantle. We also test the effects of velocity variability within the LVZ using two additional velocity models, one with increasing velocity with depth within the LVZ and one with decreasing velocity with depth within the LVZ (Figure 4.9a).

Synthetic seismograms computations use a double-couple moment tensor source with a Gaussian pulse, with a central frequency of 0.2 Hz to match the peak frequency of the filtered data. The grid spacing is ~1 km, with a model width of 309 km and depth of 110 km, and we use a time step of 0.002 seconds. The model is padded on either end of the transect by 40 km. To simulate realistic coda energy (Figure 4.4), we randomly superimposed ~2 km scatterers within the crustal layer, with randomly assigned velocity variations of up to ±5% of the P- and S-wave velocity. We use the same processing steps as for the real data to generate synthetic autocorrelation traces, and stack to create a synthetic record section (Figure 4.5).

In addition to the transect created using the actual station locations with 10-15 km spacing, we model hypothetical stations at 100 m spacing (Figure 4.10) to investigate the effects of station spacing on spatial aliasing and maximum usable frequency. For these simulations, we use additional central frequencies of 1, 2, 5, and 10 Hz, decreasing the grid spacing to 100 meters and the time step to 0.001 seconds. The size of the scatterers decreased with the central frequency such that the scatterer size was less than the dominant wavelength (e.g., Frankel and Clayton, 1986).

4.5.3 Receiver Functions

We computed receiver functions at each MOOS station along the N-S transect initially using 80 teleseismic earthquakes, a greater number of earthquakes than earlier results (Kim et al., 2014). We filter data between 0.03–1 Hz. We use an array-based deconvolution method to reduce noise (Rondenay et al., 2009), deconvolving an estimated incident wavefield arriving at all stations rather than an individual wavefield incident unique to each station (Bostock and Rondenay, 1999). We visually inspect each receiver function, and choose those with high signal-to-noise ratio and low energy on the transverse component. After this step, each station has 54-80 individual receiver functions. For each station, we stack receiver functions from a limited back-

azimuthal range of 260˚–360˚ to avoid smearing dipping structures, applying a phase-weighted stacking method (Schimmel and Paulssen, 1997) after outlier removal. For comparison to autocorrelation data, we take the uncommon step of converting the lag-time of each receiver function to an equivalent two-way S-wave travel time (Figure 4.5e-f), computed from the depth-averaged P- and S- velocities assuming a constant ray parameter of zero (*e.g.,* vertical arrivals). We calculated synthetic receiver functions using the RAYSUM code (Frederiksen and Bostock, 2000) and the same forward model used in synthetic autocorrelations. The central frequency and the back azimuth of the modeled receiver functions are set to 0.5 Hz and 270˚, respectively.

4.6 Results

4.6.1 Autocorrelation of Local Earthquake Coda

Autocorrelation traces using windows around local earthquakes have the strongest coherent energy on the E-W horizontal component (Figure 4.5c); less coherence is visible on the vertical component (Figure 4.6b). On the E-W component, distinct phases appear on traces at each station with coherence across the full N-S section. The first phase in time, a positive peak, has strong coherence from station to station and consistently arrives before 5 seconds across the transect. This first peak appear at the expected times for autocorrelation peaks from the strongly band-limited data (Figure 4.7) even in the absence of structure or reverberations; and are not representative of subsurface structure. Below the flat arrivals, dipping coherent energy is visible, beginning with a peak-trough pair arriving after ~15 seconds on the southern end of the line and increasing in time to ~25 seconds at the northern end above the deeper slab (Figure 4.5c). A second package of dipping arrivals begins at ~27 seconds on the southern end of the line, increasing to ~35 seconds on the northern end (Figure 4.5c).

In the autocorrelation section using noise (Figure 4.6c), the earlier ~2-3 second arrivals is also visible, corresponding to the peaks created by the band-limited nature of the data. The later, dipping phases observed in the local earthquake autocorrelation traces are not evident or are only weakly visible in the noise autocorrelation result.

4.6.2 Synthetic Autocorrelation Results

Our synthetic autocorrelation traces provide the seismic section that would be expected based on the SPECFEM2D modeled earthquake sources and the a priori structural model (Figure 4.1d; Li et al., 2013; Kim et al., 2014). The traces include reflections from the primary boundaries, including the top and bottom of the LVZ and the bottom of the crust, and arrivals from peg-leg reverberations within layers. On the horizontal component (Figure 4.5c), a strong, flat arrival is visible at ~2-3 seconds, followed by subhorizontal arrivals at ~5-6 seconds which resulted from the uppermost boundary in the velocity model used (Figure 4.1d). Arrivals from the top of the LVZ are distinct in synthetic data, beginning at ~15 seconds of two-way-travel-time (TWTT) on the southern end of the transect and increase in time to ~25 seconds on the northern end of the line, where the slab is deeper. Arrivals from the bottom of the LVZ are also distinctly visible from ~18 seconds to ~28 seconds TWTT, increasing in time from south to north. The arrival from the bottom of the Yakutat crust arrives at ~28 seconds on the southern end, increasing to ~33 seconds on the northern end. The phases arriving before the arrival from the top of the LVZ are partially caused by peg-leg arrivals, expected at ~3 seconds (reverberations within the LVZ), at ~9 seconds (reverberations within the Yakutat crust), and at ~12 seconds (reverberations within both). Additionally, depth phases of each earthquake create arrivals at variable times depending on earthquake depth; these depth phases destructively interfere if enough earthquakes occurring at different depths are stacked together but are not fully suppressed.

Of primary importance, each major interface in the a priori velocity model appears as a distinct arrival in the synthetic autocorrelogram sections.

4.6.3 Receiver Function Results

Receiver functions are commonly displayed as a function of the lag time, the differential time between the direct P wave and the converted S-wave from an interface. In our results, we convert this lag time to the equivalent travel time required for S-waves to travel from the surface to the interface and back at vertical incidence, TWTT (see Methods section), We do this comparison to directly compare receiver function phases to autocorrelation results. In our receiver function section, the primary visible phase, a negative trough followed by a less coherent peak, begins at ~15 seconds equivalent TWTT on the southern end of the line, and increases to >25 seconds on the northern end. A second dipping phase, a positive peak, is weakly visible from ~30 seconds equivalent TWTT in the south to ~40 seconds in the north. Synthetic receiver functions indicate that these phases correspond to the top of the LVZ and the Yakutat Moho (Figure 4.5f). Though the receiver functions have a central frequency of ~0.5 Hz, the dominant wavelength of each receiver function is effectively longer than for autocorrelation traces which spend greater time within each layer, and thus receiver functions provide lower-resolution with respect to the separation of subsurface boundaries

4.6.4 Velocity Model Variations

For autocorrelation data, the results from variations in velocity models within the LVZ indicate that autocorrelation traces are strongly dependent upon the details of wavespeed within this layer (Figure 4.9). For constant velocity, both top and bottom interface are visible in autocorrelation synthetics. In contrast, for the increasing and decreasing velocity cases, only the top or bottom interfaces are clearly visible, respectively. For receiver functions, details of the wavespeed structure within the LVZ

have little impact on modeled waveforms (Figure 4.9).

4.6 Discussion and Interpretation

4.6.1 Autocorrelation Imaging Using Earthquake Coda

The horizontal autocorrelation results, using windows around local earthquakes, clearly image a distinct dipping boundary at the expected arrival time of the bottom of the proposed low-velocity zone (Figure 4.5c). A second dipping phase coincides with the expected arrival from the bottom of the Yakutat crust between 27 to 35 seconds TWTT, and later arrivals are likely multiples of these boundaries (*e.g.,* Figure 4.5b). These primary arrivals correspond closely to arrivals visible in the receiver function image and synthetics (Figure 4.5e-f), providing confidence that the dipping arrivals are from the primary structural boundaries of the subduction system.

Unlike the arrival from the bottom of the LVZ, the arrival from the top of the LVZ is not well-imaged in our autocorrelation result (Figure 4.5c). Modeling indicates that a wavespeed decrease within the LVZ (Figure 4.9), toward the top of oceanic crust, results in a weak top and strong bottom arrival, possibly suggesting an increase in fracture permeability approaching the main plate interface. The longer-wavelength receiver functions are not sensitive to structure at this scale (Figure 4.5); hence the higher resolution of the autocorrelation traces provides information on the nature of the subducting interface not previously available. The bottom of the Yakutat crust is also more clearly visible in our autocorrelation section than in our receiver function result (Figure 4.5e) or in previous results (Kim et al., 2014).

In the vertical autocorrelation section, no coherent dipping arrivals are visible, though such arrivals are expected based on synthetic models (Figure 4.6b). In part this may result from lack of the low frequency energy for P-wave in contrast to S-wave arrivals (Figure 4.1c). The lower radiated p-wave energy compared to s-wave energy, and the resulting decrease in the amplitude of p-wave reflections, may also cause p-

wave energy to be insufficient to stack coherently above the noise.

Autocorrelation imaging using the noise windows does not clearly show dipping structure, though the frequency band used in noise windows is similar to the frequency band used in the earthquake windows (Figure 4.8). This result suggests that earthquake coda are present within this lower spectral peak, generally thought to consist of primarily ambient noise, and that this lower frequency earthquake energy is coherently stacking for the earthquake windows. In our study, we did not attempt to migrate the imaged arrivals from the dipping layers. For dense arrays, migration would allow the inclusion of earthquakes at greater incidence angels.

4.6.2 Implications for Dense Imaging Array: Synthetic Sections at Variable Spacing

The high frequency content (>10 Hz) within local earthquake sources would ideally be included in our autocorrelation imaging for highest resolution of thin structures. However, the MOOS station spacing of 10-15 km aliases signals at those higher frequencies (Figure 4.6d-e), and we down-filter the data in our analysis to remove the aliasing (Figure 4.5c). To preserve unaliased signals at 10 Hz would require a station spacing of ~150 meters for vertically-arriving signals at 6 km/sec. The need for dense spacing to preserve unaliased data and high frequency, or alternatively the need to decrease the dominant frequency used for sparse station spacing, is clear in our synthetic comparison of the two spacings (Figure 4.10). For the MOOS station spacing, boundaries are only clearly visible on the 0.2 Hz section, and are aliased and not visible at higher frequencies. In contrast, at the 100-m station spacing, the boundaries are visible at all frequencies including 10 Hz. A dominant frequency of 10 Hz, for 6 km/s wavespeed, allows resolution of boundaries on the scale of hundreds of meters, much better than the resolution at the scale of kilometers possible with the dominant frequency of 0.2 Hz used in this study based on the MOOS station spacing. Deploying dense arrays to record seismicity, for use in autocorrelation,

could facilitate imaging of detailed plate interface structure if a sufficient distribution of earthquakes is recorded.

4.7 Conclusions

We present seismic images of the subducting slab in the central Alaskan subduction zone using autocorrelation to extract scattered energy from local earthquake coda. Dipping interfaces of the subducting oceanic plate are evident in our image, and correlate to boundaries visible in the lower-resolution but well-accepted receiver function methodology. Our results suggest that velocity decreases toward the top of oceanic crust, providing information on plate boundary structure at scales beyond the limits of receiver functions. Additionally, we also observe an interface at the bottom of the subducting Yakutat crust that is not well-imaged in receiver functions. Our result is thus one of the most compelling examples to date of using body waves within local earthquake coda (interferometry) to study mantle structure. Our new images both provide information on the nature of the plate interface in the Alaska-Aleutian system, and demonstrate the utility of using local earthquake coda for structural imaging in subduction zone with appropriate arrays. Dense station spacing would provide the resolution necessary to constrain small-scale structures and further probe the physical properties of plate interfaces in subduction zone. Such imaging methodologies have the ability to produce higher resolution images of deep structure than possible using other passive techniques, at much lower cost than active-source multichannel studies.

4.8 Figures

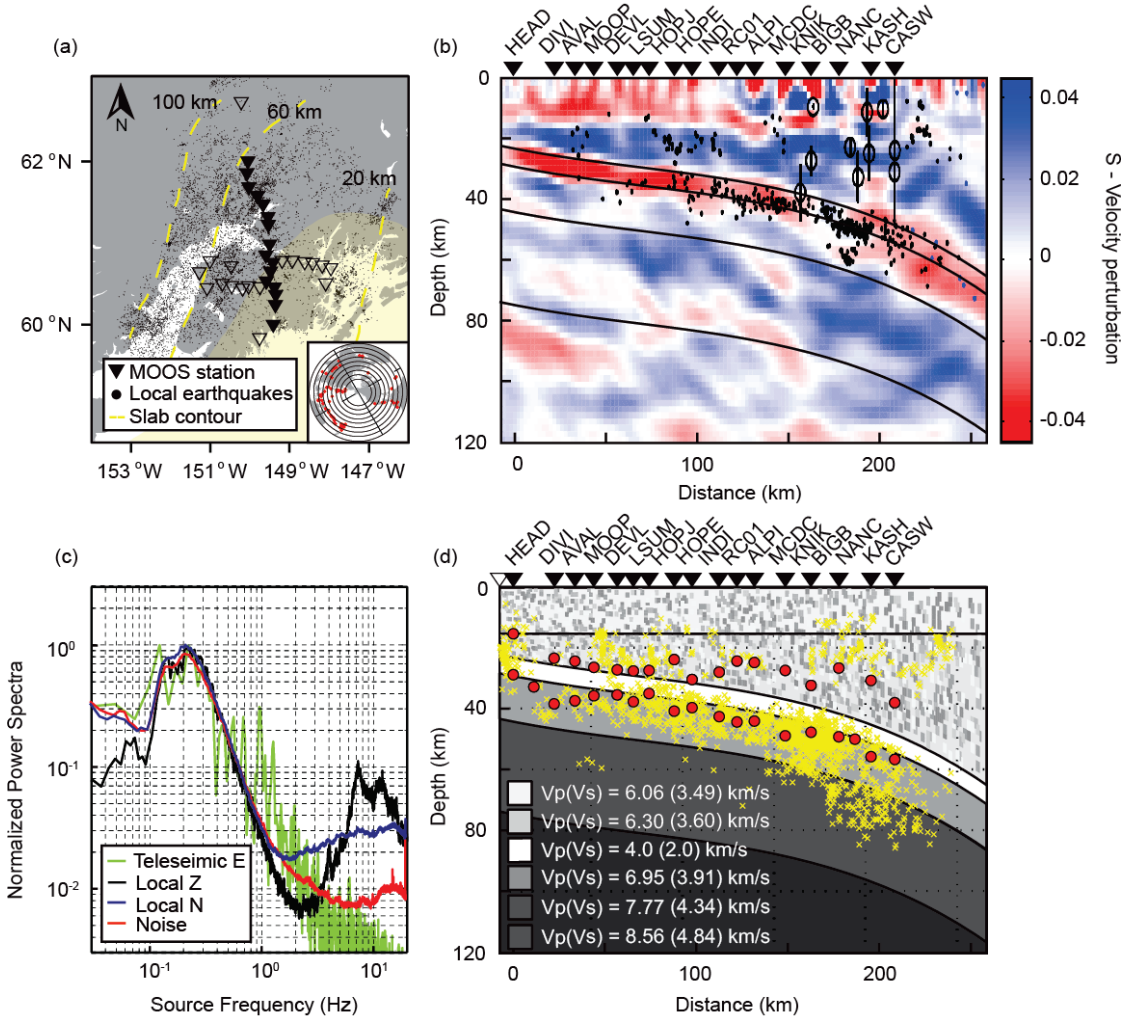

Figure 4.1: (a) Study area in the Alaska-Aleutian subduction zone. MOOS seismic stations (Li et al., 2013) are black reverse triangles; data from stations with solid symbols are used in this study. Local seismicity from 2007-2008 (black dots) is from the relocated catalog of Li et al. (2013) along with inferred contours of depth to the top of the subducting slab (dashed yellow lines). Teleseismic earthquakes for receiver functions are red circles in the inset map. (b) The receiver function migration image (Kim et al. 2014) used to create the forward model of subducting slab structure (black lines). Distance at 0 km indicates station HEAD. (c) Normalized power spectra for P waves from a local (red/blue), and teleseismic (green) earthquake, and ambient noise (black), recorded at MOOS station HOPJ. Peak frequencies are ~10 Hz for the local earthquake and ~0.2 Hz for the teleseismic earthquake. (d) Local earthquakes (yellow symbols) from within 20 km of the best-fit line to the MOOS stations, projected onto the slab model from (b). Earthquakes used in synthetic modeling are denoted by red circles. Seismic velocities are from Li et al., 2013, with random scatterers in the upper

crustal layer of ±5 % (e.g. Frankel and Clayton, 1986) to generate earthquake coda energy (see Figure 4.4).

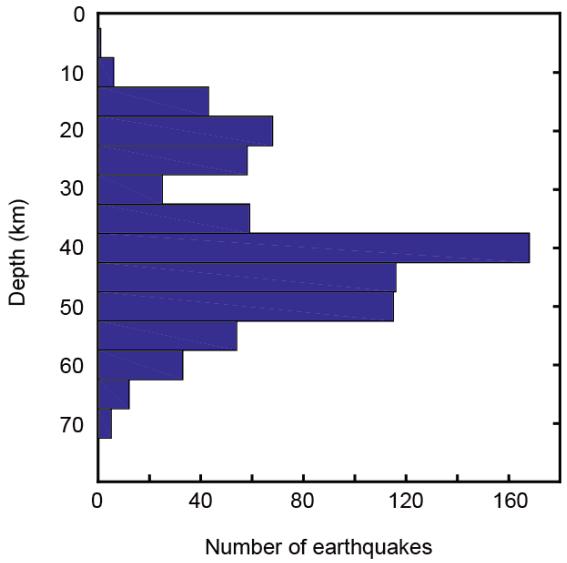

Figure 4.2: Depth distribution of 763 local earthquakes used in the final imaging result.

HEAD	DIVI	AVAL	MOOP	DEVL	LSUM	HOPJ	HOPE	INDI	RC01
46	22	110	79	91	130	42	151	131	13
ALPI	MCDC	KNIK	BIGB	NANC	KASH	CASW			
77	17	28	152	58	47	24			

Table 4.1: Number of local earthquakes used for each MOOS station.

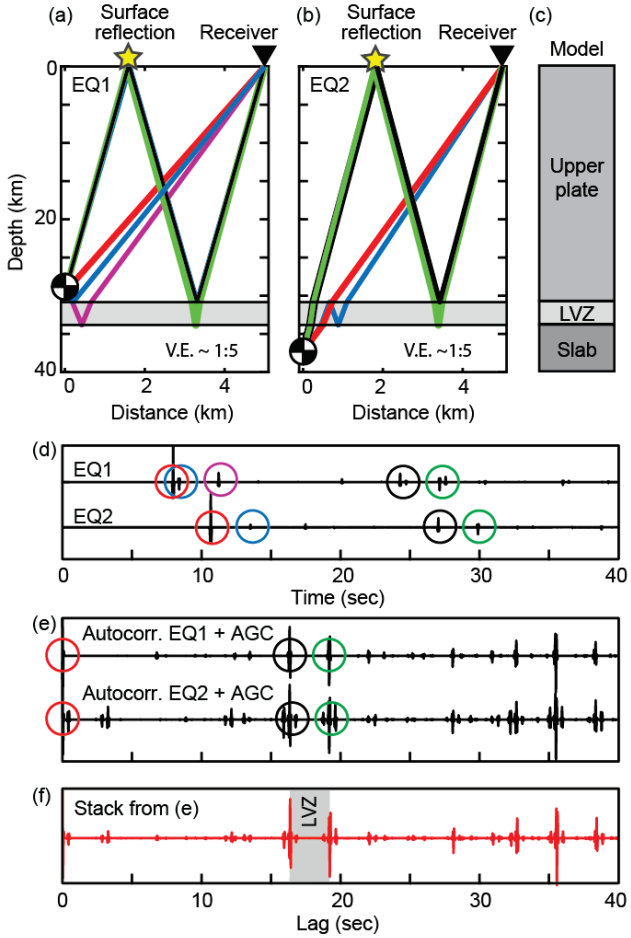

Figure 4.3: Schematic of the autocorrelation imaging method. (a-b) Earthquakes above (a) and below (b) a modeled low-velocity zone (LVZ) in (c) produce multiple phases on recorded traces (d), including direct arrivals (red circles), peg-leg multiples from the top and bottom of the LVZ (blue and magenta circles), reflections from the top and bottom of the LVZ following a surface reflection of the direct arrival (black and green), and additional reverberations at greater times (paths not shown in 4.3a-b). Autocorrelation of each trace in (d) re-datums the start time to the direct arrival and removes source effects (e). For near-vertical ray-paths, reflections from subsurface boundaries will arrive at similar times at a given station regardless of earthquake location or mechanism, and traces can be stacked to enhance signal to noise ratio (f).

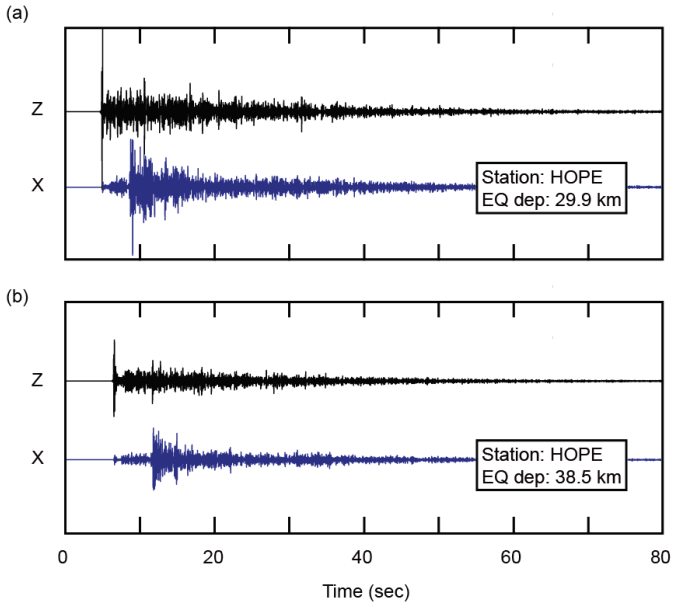

Figure 4.4: Two examples of synthetic waveforms produced by SPECFEM2D modeling including vertical (Z) and horizontal (X) components.

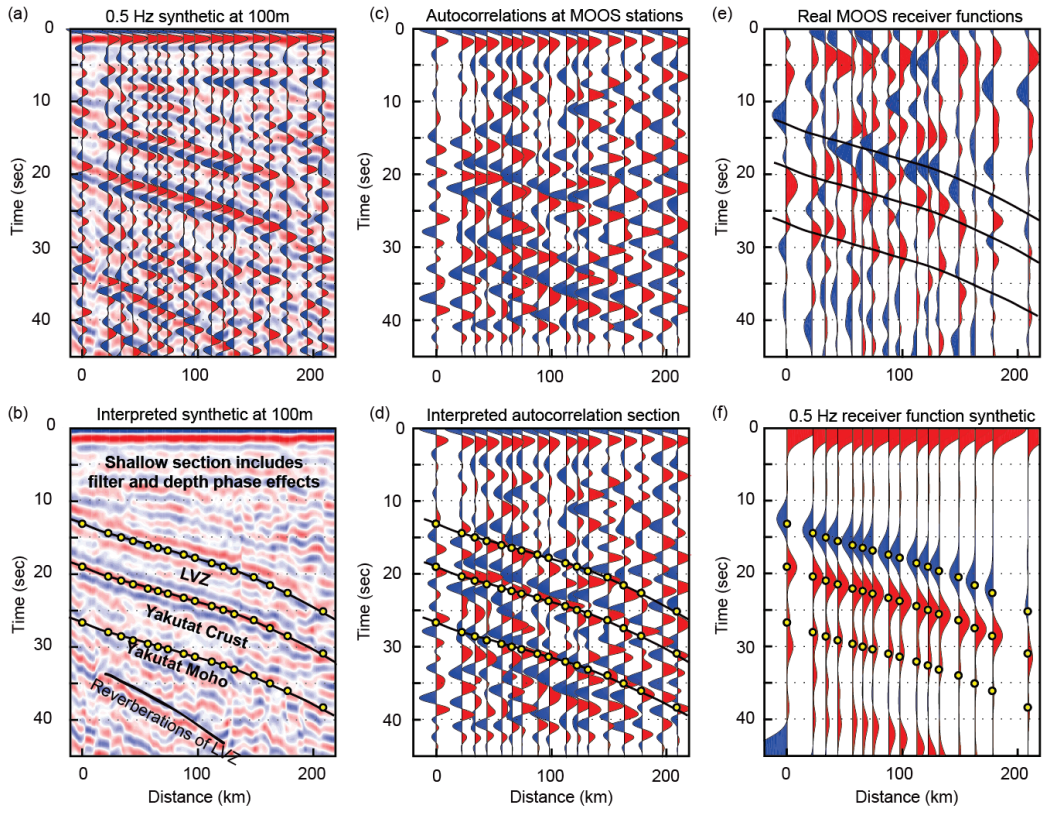

Figure 4.5: (a) Comparison of synthetic and real autocorrelation traces and receiver

functions. (a) Synthetic autocorrelation section produced by SPECFEM (Tromp et al., 2008) using the modeled slab structure and the actual MOOS station locations. The same synthetic section of idealized 100m station spacing is shown in the background. (b)The interpreted synthetic section from (a); yellow circles denote the primary peaks and troughs from the receiver function synthetic section in (f) to demonstrate the correlated arrivals in data of different types. (c) and (d) show the real stacked autocorrelation section from the MOOS stations, and the annotated version, respectively. (e) and (f) show the real stacked, and synthetic receiver functions at MOOS stations, respectively. Distance is from station HEAD (Figure 4.1).

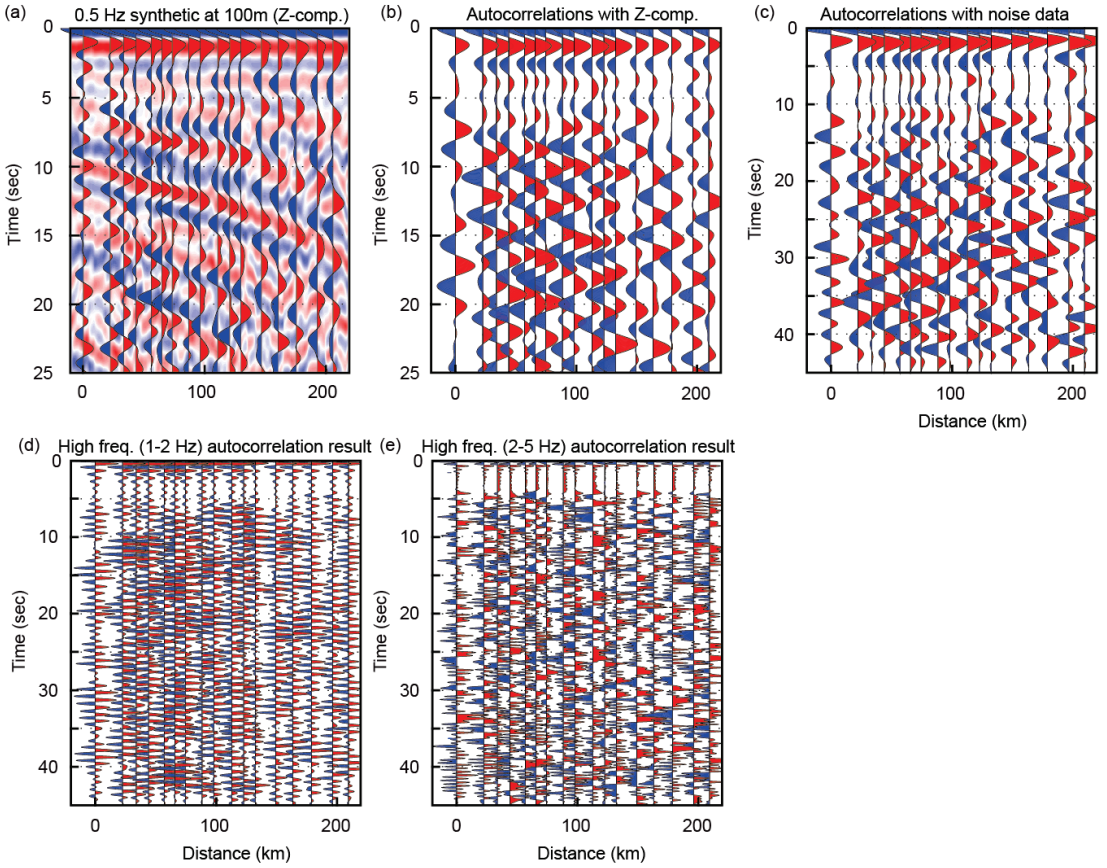

Figure 4.6: (a) Synthetic autocorrelation from a vertical component at MOOS station spacing overlaid with an idealized station spacing of 100m, using the velocity model shown in Figure 5.1c. (b) Stacked autocorrelation section at MOOS station spacing with vertical component record. (c) Stacked autocorrelation response of the ambient noise data. For ambient noise data, 60 sec time window before the P arrivals of 763 earthquakes (yellow symbols, Figure 4.1d) are used. (d-e) Stacked autocorrelation sections using high frequency signals between 1-2 Hz and 2-5 Hz, respectively.

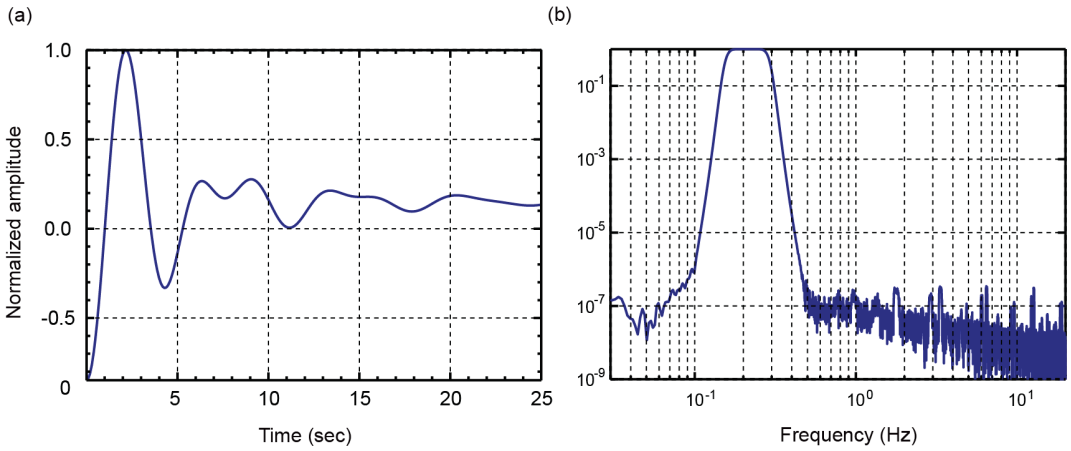

Figure 4.7: Representation of band-limited data used in autocorrelation. (a) An autocorrelation of the transfer function of a 0.05-1 Hz bandpass filter. (b) Amplitude spectra of the transfer function in (a).

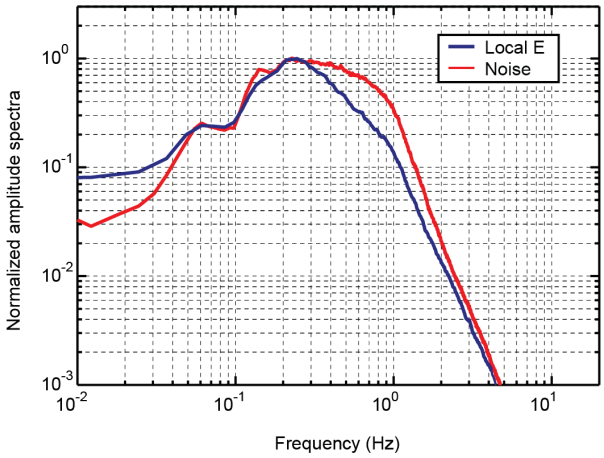

Figure 4.8: Normalized amplitude spectra of the frequency band used in earthquake (blue) and noise (red) windows.

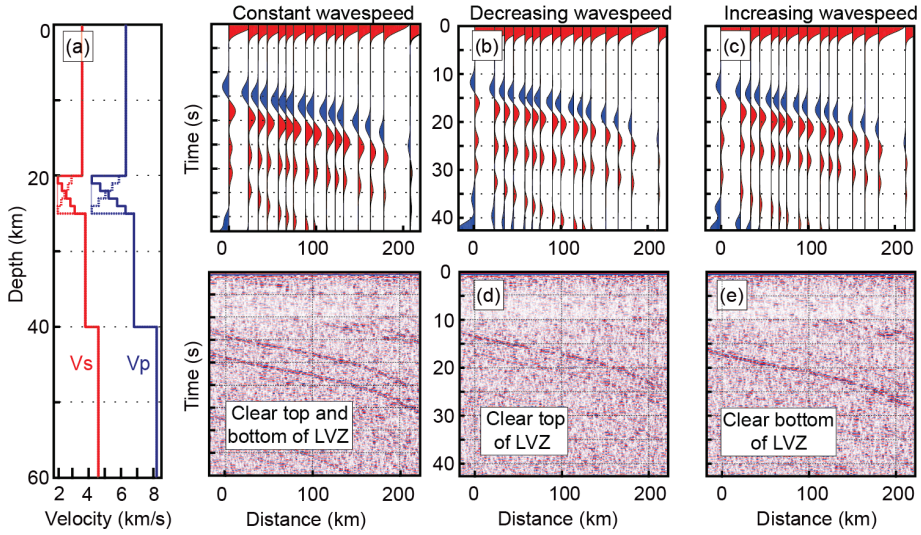

Figure 4.9: Variability in reflection strength for three models of LVZ structure. (a) Models of constant, increasing, and decreasing wavespeed within the LVZ. (b-c) Receiver function synthetic data for the three models. Receiver function models vary little for the three cases. In contrast, the strength of the top and bottom reflections of the LVZ are strongly dependent upon the structure of the LVZ. The model of decreasing wavespeed within the LVZ best matches the real autocorrelation data, which shows a strong bottom reflector but little to no top reflector (Figure 4.5c).

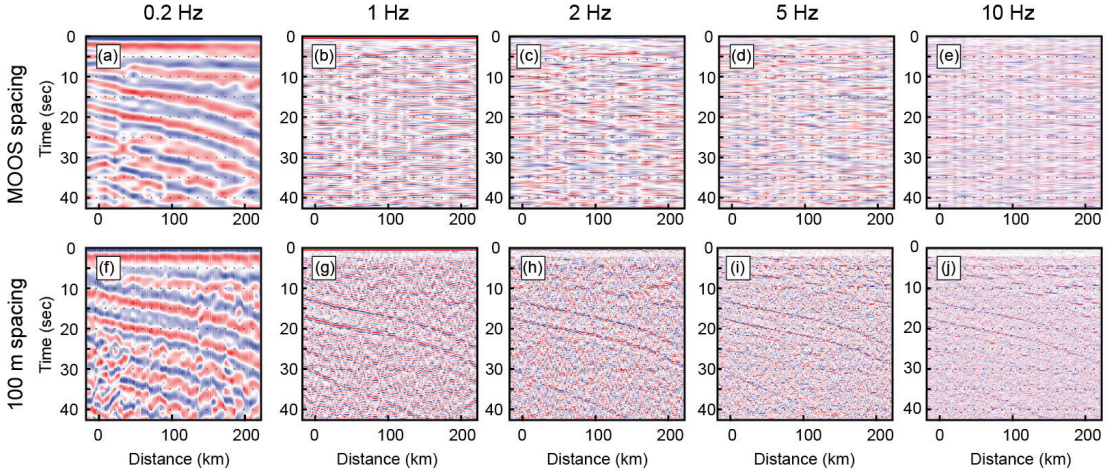

Figure 4.10: Synthetic SPECFEM autocorrelation sections shown at variable station spacing and frequency bands. (a-e) Synthetic sections at actual MOOS station spacing of 10-15km using dominant frequencies of 0.2, 1, 2, 5, and 10 Hz, respectively. (f-j) Synthetic sections at modeled 100m station spacing. Slab structure is weakly visible at 1 Hz at the MOOS station spacing, but is aliased. For the modeled dense station spacing, slab structure is visible using signals at 10 Hz, allowing greater resolution of proposed roughness or layering near the slab interface (*e.g.,* Li et al., 2015).

REFERENCES

Audet, P., Bostock, M. G., Christensen, N. I., & Peacock, S. M. (2009). Seismic evidence for overpressured subducted oceanic crust and megathrust fault sealing. Nature, 457(7225), 76–78.

Bécel, A., D. J. Shillington, M. Delescluse, M. R. Nedimović, G. A. Abers, D. M. Saffer, S. C. Webb, K. M. Keranen, P.-H. Roche, and J. Li (2017), Tsunamigenic structures in a creeping section of the Alaska subduction zone, Nature Geoscience, 10(8), 609.

Bostock, M. G. (2013), The Moho in subduction zones, Tectonophysics, 609, 547-557, doi:10.1016/j.tecto/2012.07.007.

Bostock, M. G., & Rondenay, S. (1999). Migration of scattered teleseismic body waves. Geophysical Journal International, 137(3), 732–746.

Burdick, L. J., & Langston, C. A. (1977). Modeling crustal structure through the use of converted phases in teleseismic body-wave forms. Bulletin of the Seismological Society of America, 67(3), 677–691.

Christensen, N. I. (1984). Pore pressure and oceanic crustal seismic structure. Geophysical Journal International, 79(2), 411–423.

Christeson, G. L., Gulick, S. P., van Avendonk, H. J., Worthington, L. L., Reece, R. S., & Pavlis, T. L. (2010). The Yakutat terrane: Dramatic change in crustal thickness across the Transition fault, Alaska. Geology, 38(10), 895–898.

Claerbout, J. F. (1968), Synthesis of a layered medium from its acoustic transmission response, Geophysics, 33(2), 264–269.

Dixon, T. H., & Moore, J. C. (2007). The seismogenic zone of subduction thrust faults. Columbia University Press.

Draganov, D., Campman, X., Thorbecke, J., Verdel, A., & Wapenaar, K. (2009). Reflection images from ambient seismic noise. Geophysics, 74(5), A63–A67. https://doi.org/10.1190/1.3193529

Ferris, A., Abers, G. A., Christensen, D. H., & Veenstra, E. (2003). High resolution image of the subducted Pacific (?) plate beneath central Alaska, 50–150 km depth. Earth and Planetary Science Letters, 214(3), 575–588.

Frankel, A., & Clayton, R. W. (1986). Finite difference simulations of seismic scattering: Implications for the propagation of short-period seismic waves in the crust and models of crustal heterogeneity. Journal of Geophysical Research: Solid Earth, 91(B6), 6465–6489.

Hansen, R. T. J., M. G. Bostock, and N. I. Christensen (2012), Nature of the low velocity zone in Cascadia from receiver function waveform inversion, Earth Planet. Sci. Lett., 337-338, 25-38.

Ichinose, G., P. Somerville, H. K. Thio, R. Graves, and D. O'Connell (2007), Rupture process of the 1964 Prince William Sound, Alaska earthquake from the combined inversion of seismic, tsunami and geodetic data, J. Geophys. Res., 112, B07306, doi:07310.01029/02006JB004728.

Ito, Y., & Shiomi, K. (2012). Seismic scatterers within subducting slab revealed from ambient noise autocorrelation. Geophysical Research Letters, 39(19).

Kato, A., T. Iidaka, R. Ikuta, Y. Yoshida, K. Katsumata, T. Iwasaki, S. i. Sakai, C. Thurber, N. Tsumura, K. Yamaoka, T. Watanabe, T. Kunitomo, F. Yamazaki, M. Okubo, S. Suzuki, and N. Hirata (2010), Variations of fluid pressure within the subducting oceanic crust and slow earthquakes, Geophys. Res. Lett., 37(14), L14310, doi:10.1029/2010gl043723.

Kim, Y., Abers, G. A., Li, J., Christensen, D., Calkins, J., & Rondenay, S. (2014). Alaska Megathrust 2: Imaging the megathrust zone and Yakutat/Pacific plate interface in the Alaska subduction zone. Journal of Geophysical Research: Solid Earth, 119(3), 1924–1941.

Kim, D., Brown, L. D., Árnason, K., Águstsson, K., & Blanck, H. (2017). Magma reflection imaging in Krafla, Iceland, using microearthquake sources. Journal of Geophysical Research: Solid Earth, doi/10.1002/2016JB013809/full

Lay, T., H. Kanamori, C. J. Ammon, K. D. Koper, A. R. Hutko, L. Ye, H. Yue, and T. M. Rushing (2012), Depth-varying rupture properties of subduction zone megathrust faults, Journal of Geophysical Research: Solid Earth (1978–2012), 117(B4).

Li, J., Abers, G. A., Kim, Y., & Christensen, D. (2013). Alaska megathrust 1: Seismicity 43 years after the great 1964 Alaska megathrust earthquake. Journal of Geophysical Research: Solid Earth, 118(9), 4861–4871.

Lin, F.-C., Moschetti, M. P., & Ritzwoller, M. H. (2008). Surface wave tomography of the western United States from ambient seismic noise: Rayleigh and Love wave phase velocity maps. Geophysical Journal International, 173(1), 281–298.

Nakata, N., Snieder, R., & Behm, M. (2014). Body-wave interferometry using regional earthquakes with multidimensional deconvolution after wavefield decomposition at free surface. Geophysical Journal International, 199(2), 1125–1137.

Nedimović, M. R., Hyndman, R. D., Ramachandran, K., & Spence, G. D. (2003). Reflection signature of seismic and aseismic slip on the northern Cascadia subduction interface. Nature, 424(6947), 416–420.

Nishitsuji, Y., Minato, S., Boullenger, B., Gomez, M., Wapenaar, K., & Draganov, D. (2016). Crustal-scale reflection imaging and interpretation by passive seismic interferometry using local earthquakes. Interpretation, 4(3), SJ29–SJ53.

Plafker, G. (1965). Tectonic deformation associated with the 1964 Alaska earthquake. Science, 148(3678), 1675–1687.

Plafker, G., & Berg, H. C. (1994). The geology of Alaska. Geological Society of America, 1068 p.

Rondenay, S. (2009), Upper mantle imaging with array recordings of converted and scattered teleseismic waves, Surv. Geophys., 30, 377-405.

Rondenay, S., Bostock, M. G., & Shragge, J. (2001). Multiparameter two-dimensional inversion of scattered teleseismic body waves 3. Application to the Cascadia 1993 data set. Journal of Geophysical Research: Solid Earth, 106(B12), 30795–30807.

Roux, P., Sabra, K. G., Gerstoft, P., Kuperman, W. A., & Fehler, M. C. (2005). P-waves from cross-correlation of seismic noise. Geophysical Research Letters, 32(19).

Rowe, C. D., J. C. Moore, F. Remitti, and t. I. E. T. Scientists (2013), The thickness of subduction plate boundary faults from the seafloor into the seismogenic zone, Geology, 41, 991-994.

Ruigrok, E., & Wapenaar, K. (2012). Global-phase seismic interferometry unveils P-wave reflectivity below the Himalayas and Tibet. Geophysical Research Letters, 39(11).

Ryberg, T. (2011). Body wave observations from cross-correlations of ambient seismic noise: A case study from the Karoo, RSA. Geophysical Research Letters, 38(13), L13311. https://doi.org/10.1029/2011GL047665

Schimmel, M., & Paulssen, H. (1997). Noise reduction and detection of weak, coherent signals through phase-weighted stacks. Geophysical Journal International, 130(2), 497–505.

Schuster, G. T. (2009). Seismic interferometry (Vol. 1). Cambridge University Press Cambridge.

Schwartz, S. Y., and J. M. Rokosky (2007), Slow slip events and seismic tremor at circum-pacific subduction zones, Reviews of Geophysics, 45(3), art. no. rg3004, doi:Rg300410.1029/2006rg000208.

Shapiro, N. M., Campillo, M., Stehly, L., & Ritzwoller, M. H. (2005). High-resolution surface-wave tomography from ambient seismic noise. Science, 307(5715), 1615–1618.

Tromp, J., Komattisch, D., & Liu, Q. (2008). Spectral-element and adjoint methods in seismology. Communications in Computational Physics, 3(1), 1–32.

Tsuji, Y., J. Nakajima, and A. Hasegawa (2008), Tomographic evidence for hydrated oceanic crust of the Pacific slab beneath northeastern Japan: Implications for water transportation in subduction zones, Geophys. Res. Lett., 35, L14308, doi:14310.11029/12008GL034461.

von Huene, R., Miller, J. J., & Weinrebe, W. (2012). Subducting plate geology in three great earthquake ruptures of the western Alaska margin, Kodiak to Unimak. Geosphere, 8(3), 628–644.

Wapenaar, K., Slob, E., & Snieder, R. (2008). Seismic and electromagnetic controlled-source interferometry in dissipative media. Geophysical Prospecting, 56(3), 419–434.

Worthington, L. L., Van Avendonk, H. J., Gulick, S. P., Christeson, G. L., & Pavlis, T. L. (2012). Crustal structure of the Yakutat terrane and the evolution of subduction and collision in southern Alaska. Journal of Geophysical Research: Solid Earth, 117(B1).

Zhan, Z., Ni, S., Helmberger, D. V., & Clayton, R. W. (2010). Retrieval of Moho-reflected shear wave arrivals from ambient seismic noise. Geophysical Journal International, 182(1), 408–420.

CHAPTER 5

FROM TRASH TO TREASURE: 3D BASEMENT IMAGING WITH "EXCESS" DATA FROM OIL AND GAS EXPLORATION

5.1 Abstract

Modern oil and gas seismic surveys often use areal arrays that record continuously and routinely collect "excess" data which are not needed for the conventional Common Reflection Point (CRP) imaging that is the primary goal for exploration purposes. These excess data, once considered as simply noise, have recently been recognized to have utility not only in resource exploration but also for addressing a diverse range of scientific issues. Here we report processing of such discarded data from recent exploration surveys carried out in southeastern New Mexico. From these we have produced the first 3D seismic reflection imagery of an extensive layered complex within the crystalline basement as well as elements of the underlying lower crust. This enigmatic basement layering has been found on industry and academic seismic reflection surveys at many sites in the central U.S. We interpret these reflections as marking an extensive, continental scale network of tabular mafic intrusions linked to the Keweenawan rifting of the igneous east-central U.S. during the late Proterozoic. This study clearly demonstrates that the new generation of continuously recorded 3D exploration datasets, which penetrate below the sedimentary rocks, represent a valuable source of fresh information on basement structure and evolution. Furthermore, such information can be helpful in assessing any risks associated with induced seismicity related to waste water injection in oil and gas producing areas.

5.2 Introduction

Seismology has been an essential tool for probing the deep crust since Mohorovičić first provided a seismological definition of its base (Mohorovičić, 1910)

The material in Chapter 5 has been submitted and currently in revision under Kim et al., From trash to treasure: 3D basement imaging with "excess" data from oil and gas exploration. *AAPG Bulletin* (2018)

using refraction techniques. Beginning with the Consortium for Continental Reflection Profiling (COCORP) program in the mid-1970s (*e.g.,* Oliver et al., 1976), systematic application of multichannel techniques has led to routine reflection imaging of crustal heterogeneities around the world (*e.g.,* Brown, 2013). Although a large fraction of the continental lithosphere has now been probed by deep reflection surveys, almost all of these have been in the form of 2D seismic profiling. The only deep 3D surveys of the continental basement which have been reported in peer reviewed literature are surveys associated with the Kontinentales Tiefbohrpro- gramm der Bundesrepublik Deutschland (KTB) deep drill hole in central Germany (*e.g.,* Stiller, 1991), a COCORP survey in southeastern Georgia (Cook et al., 1981) and a LITHOPROBE survey in Alberta, Canada (*e.g.,* Welford and Clowes, 2004).

Recent technical advances in the oil and gas industry's capability for acquiring 3D seismic reflection data in sedimentary basins represent a new opportunity for extracting 3D seismic imagery of underlying basement. Prior to this time, most traditional seismic surveys were based on the "roll-along" model, in which a finite array or grid of geophones recorded a fixed time of ground vibration after a seismic source was set off (Figure 5.1a). Thus the seismic recordings were tightly limited in both time and space. Today, modern nodal units are capable of recording continuously for much larger time spans (Figure 5.1b). However, normally only a fraction of these recordings are harvested to produce CRP stacks for the intended exploration purpose (typically equivalent to 5 second two-way travel time or less). In fact, little of the data that lies between those portions of the recordings specifically harvested for conventional reflection imaging have been utilized. However these "interstitial" or "excess" data record any ground vibrations between shots. These portions of the recordings may contain a wide variety of information that can be used for diverse studies including a) vibrations due to natural ambient noise that can be used to map

subsurface velocity variations using seismic interferometry (*e.g.,* Lin et al., 2013), b) vibrations due to cultural noise (*e.g.,* Nakata et al., 2011; Quiros et al., 2016), c) seismic arrivals from local earthquakes (*e.g.,* Inbal et al. 2015), and d) teleseismic arrivals (*e.g.,* Schmandt and Clayton, 2013). Within the exploration context, there is growing recognition that the ambient noise component can provide low frequency information that can enhance conventional reflection imagery and subsequent velocity inversion (*e.g.,* Bussat and Kuglar, 2011).

Of primary interest here is that such surveys will likely contain reflection energy that has probed the crystalline basement, arriving back to the array at travel times that exceed that harvested for resource exploration purposes. In short, these new generation industry surveys constitute a systematic exploration of the continental basement using high-resolution 3D seismic reflection techniques as a no-cost (at least in terms of field acquisition) by-product.

This analysis uses a small subset of a recent 3D seismic survey in the Permian Delaware Basin of southeastern New Mexico (Figure 5.2) that was conducted by Fairfield Nodal and provided to Cornell University for the purpose of this study. The 3D basement imagery produced from this dataset reveals details, for the first time in 3D, of a dramatic layered sequence that is correlative with upper crustal layering first reported in the late 1970s from COCORP crustal reflection surveys in north-central Texas and southern Oklahoma.

5.3 Data processing and methodology

The Permian Basin of west Texas and southeastern New Mexico (Figure 5.2) was formed during late Proterozoic and was subdivided into smaller basins due to subsequent tectonism in the Paleozoic (Keller et al., 1980). The geologic province extends from the Diablo platform on the west to the Midland basin to the east (Ward et al., 1986). The central part of the basin is dominated by a major north-south trending

fault zone associated with the uplift of the Central Basin Platform (Hills, 1984). Since 1921, when oil was first discovered in Mitchell County, Texas, hydrocarbon exploration in the basin has been intensive (Montgomery et al, 1999). The Permian basin is currently the largest oil and gas deposit active being explored in U.S. (Gaswirth et al., 2016).

The seismic data were collected using 16 second duration vibroseis signals and harvested as 21 second uncorrelated shot gathers. In total, 2562 shots were recorded by the same number of geophones. Source and receiver spacing were 50 and 250m respectively, with corresponding inline and crossline spacing of 250 and 50m. Ideally for deeper imaging, one would want to re-harvest the original field recordings for longer data windows. In our case, the conventionally harvested data were more immediately available. However, as these data were provided in uncorrelated form, the depth of potential reflection recovery could be increased by the well-known technique of extended correlation (*e.g.,* Okaya and Jarchow, 1989). As can be seen from Figure 6.3b significant energy was retained in the range of 10-20Hz at basement travel times.

Extended correlation basically trades bandwidth for additional travel time. Since an upsweep was used in the survey, the bandwidth loss will occur at the higher frequencies (*e.g.,* Figure 5.3b) which are less effective for deeper penetration due to attenuation. Figure 6.3d illustrates extended correlation as applied to a sample shot gather down to 15 seconds. After extended correlation, 2D profiles and a 3D reflection volume were produced with relatively conventional CRP processing routines (e.g., Yilmaz, 2001). The key components of this processing were: 1) trace editing to eliminate noisy traces, 2) bandpass (10-20Hz) filtering to emphasize deeper reflection signals, 3) CRP velocity analysis (*e.g.,* Figure 5.3e), 4) NMO correction, and 5) CRP stack (25 x 25m) binning. Post-stack 3D F-K migration was applied to the final CRP stacked volume.

5.4 Result and interpretation

5.4.1 Crustal vs. nodal survey

Comparison (Figure 6.4) of the 2D sections reprocessed from nodal data with a previous reported COCORP profile in the same basement terrane (Oliver et al., 1976) illustrates both the limitation and advantages of the new imagery. Although many similarities are found in both survey results, especially in the upper 5 second, the amplitude and continuity of deeper events are more prominent for the COCORP image. This is not unexpected, as the acquisition parameters for the crustal survey were chosen specifically for deep imaging, whereas those for the nodal survey were keyed to their much shallower sedimentary targets.

For example, the source effort for the COCORP survey was much greater than that for the nodal survey. To be specific, the COCORP data shown in Figure 5.3 used a 10 to 32Hz vibroseis sweep generated from five vibrators with 16 sweeps vertically stacked per record. Each of these records was collected using a 15 second sweep and harvested as 30 second raw data. In contrast, the source effort used for the nodal data consists of three vibrators using a total of 3 sweeps summed per record. Neglecting any differences in the size of the vibrators used, this corresponds to a source effort that was less than 20% of that of the COCORP survey. In addition, the total length of data harvested in the nodal survey (*i.e.,* 21 second raw data with 16 second duration vibroseis sweep) is only 70% of that of the COCORP data. Of course, a longer record length could be harvested from the original nodal data if it were available.

The gradual decay of the source-generated energy observed from the COCORP profile contrasts with the rapid decay with travel time for the nodal survey (Figure 5.3a). Note that amplitude decay after 5 second travel times for the nodal surveys includes the energy truncating effect of extended correlation. However, this does not imply the total absence of reflection energy at those times (Mayer and Brown, 1986).

The smaller source effort used in the nodal survey is compensated in part by the greater stacking fold for the 3D geometry, nominally 53 vs 12 for the COCORP profile. Even so, there is certainly a notable difference in quality of the two datasets at larger travel times, with the COCORP section exhibiting stronger discontinuous reflections in the deep crust (Figure 5.4). However, the key point is that the penetration of the nodal survey is more than sufficient to provide useful information at basement depths. Even more to the point, the nodal dataset is 3D versus 2D for the COCORP data, and is essentially a "free" byproduct of a survey carried out for purely exploration purposes.

5.4.2 Interpretation

Figure 5.6a shows the upper crustal portion of a 2D seismic section reprocessed from the nodal exploration survey in New Mexico, along with a previously reported seismic reflection section from nearby west Texas (Figure 5.2). As shown in Figure 5.4c, both sections are characterized by a sequence of strong layered reflections down to two-way travel times of at least 4 sec, with intermittent reflections at greater times. Although this layered character would suggest sedimentary rocks, wells in the vicinity (Figure 5.2) suggest otherwise.

For example, the Socony Mobil No. 95 State Bridges well in Lea County (Figure 5.1) encountered 0.6 meters of medium-grained micrographic granite porphyry at 4.2km depth under the Phanerozoic strata of the Delaware Basin (Muehlberger et al., 1966). The stacking velocity of 4.4 km/sec obtained from CRP analysis of the nodal data (Figure 5.3e) suggests that 4.2 km depth should correspond to 1.9 sec. Thus the any primary reflections from later than this time must lie within the Precambrian Basement. All of the samples collected from drill wells in Lea County, New Mexico as documented from Bickford et al. (2015), indicate the existence of basement rocks, usually granitic in composition. However, there is only one well, #1 Nellie (Figures

5.1 and 5.5b), of which we are aware that has reported basement samples that clearly correspond to the layered basement reflections. As first presented by Keller et al. (1989), #1 Nellie encountered an ultramafic layered intrusion, a portion of the Pecos Igneous Suite (top at 1.4km and continued to 5.8km, Kargi and Barnes 1995) at the depths corresponding to the first series of strong basement reflections beneath the nearby seismic line (Pecos, Figure 5.5b). Keller et al. (1989) conjectured these reflections to be a manifestation of Keweenawan rifting of the midcontinent, which is largely coeval with the Grenville compression (*e.g.,* Hauser et al., 1993). Adams and Miller (1995) also argued that the #1 Nellie results supported a similar interpretation of layered reflections on their seismic profile from eastern New Mexico, not far from the nodal survey (Figures 5.1 and 5.5b) although both New Mexico lines lie approximately 50 km away from the well (Figure 5.5c).

On the basis of reflection character and position beneath the Granite-Rhyolite province, we interpret this layered basement sequence to be correlative with the basement reflections mapped by COCORP surveys (*e.g.,* Figure 5.4c) carried out in 1975-1981 in northern Texas and southern Oklahoma (Oliver et al., 1976; Brewer et al., 1981; Figure 5.7). This layered sequence was originally interpreted as Proterozoic sediment or metasediment by Brewer et al. 1981. Comparable reflections were later observed on COCORP seismic profiles in Illinois, Indiana and Ohio and were argued to be an accumulation of rhyolitic flows perhaps with the occasional granite intrusion, based on the spatial correlation with the Granite-Rhyolite province (Pratt et al., 1989). However the thickness of the layered sequence (ca 5 km or more) seems incompatible to the observed thickness of known silicic volcanic deposits (Bonnichsen and Kauffman, 1987; Henry et al., 1988; Green and Fitz, 1993). If, as indicated by the #1 Nellie, this extensive sequence were the result of Keweenawan magmatism, it would imply igneous intrusion event over a much greater expanse of the eastern U.S. than

generally realized (Figure 5.6). While a sequence of related sills over such a vast area may seem extraordinary, we point out that similar sill-like basement reflectors found on several LITHOPROBE seismic lines in the Trans-Hudson orogen (*e.g.,* Mandler and Clowes, 1997; Figure 5.7) have been linked to the Mckenzie dikes swarm, which has been mapped over a comparably large area (Figure 5.6).

5.4.3 New insight from 3D

The nodal data now provide 3D imagery with which to evalute the various hypothesis for the nature of this basement layering. The advantages of 3D over 2D seismic surveys are well known in the exploration industry, both in terms of accurate imaging as well as interpretation (Brown, 1986). Since 3D imagery has largely been lacking for continental basement, its full value in the latter context remains to be explored. First, we note that the interval velocities for these basement strata obtained from stacking velocities (Figure 5.3e, and e.g., Oliver et al., 1976) are relatively high (6-6.5 km/sec) for sedimentary rocks, they are consistent with igneous or metamorphic materials. However, such average velocities do not preclude a depositional (volcanic or clastic) component, especially if substantial limestone is present, nor even the possibility that they may contain hydrocarbons. Here our focus is on geometrical features within the data volume in an attempt to identify possible structural discriminants of intrusive versus depositional activity.

Figure 5.9a shows a series of seismic time slices from the data cube in Figure 5.8 for travel times from 1.9-5.3 second. This corresponds to the upper portion of the Precambrian layering. The linear features exhibited in these time slices could be the expression of igneous dikes, a vertical feature that might be difficult to distinguish on any 2D basement reflection imagery. Circular features in the upper basement depth slices might also be interpreted as intrusive events. For example, the circular feature in Figure 6.9b that exhibits a successively decreasing radius with increasing travel time

(depth) implies a cuspate geometry. Saucer-shaped reflections in both Phanerozoic strata and basement rocks observed on industry and academic seismic surveys elsewhere have been either identified or interpreted as mafic igneous intrusions (*e.g.,* Hansen and Cartwright, 2006; Polteau et al., 2008). Neither of these particular patterns is unique to igneous processes. Linear patterns are common in sedimentary sequences due to faulting, and a cuspate geometry could just as easily be evidence of a sag in a sedimentary (or now metasediementary) basin, especially given such a small sample of data. 3D coverage of a significantly larger area would be likely to provide a more definitive view of structural relationship that might distinguish between depositional and intrusive origins.

5.4.4 Relevance to oil and gas exploration

The structure and evolution of the basement imaged by data such as that examined here, is of more than academic interests. Sedimentary basins and their internal structures are often linked to underlying basement tectonics. In a more recent context, basement faults are suspected to play a major role in defining the hazards related to seismicity due to water injection related to both hydraulic fracturing and waste disposal (Ellsworth 2013; Keranen et al., 2014). Knowledge of the geometry and distribution of basement faults in areas of water injection would aid in mitigating any hazards associated with such activities (Horton, 2012; Kim, 2013).

5.5 Conclusions

We present the first industry scale 3D reflection image of deep intrabasement features in the United States. The processed 3D reflection volume was produced by reprocessing normally discarded portions of petroleum seismic surveys from the northern Permian Delaware Basin in southeastern New Mexico. The resulting 3D seismic volume details the dramatic basement layering that was first revealed by crustal profiling by the COCORP program. Based on the combination of these

COCORP results, mafic borehole lithology, and basement stratigraphy in our new 3D images, we suggest that these prominent Precambrian layered sequences are part of an extensive, continental scale network of tabular mafic intrusions associated with Keweenawan rifting. Although the quality of the deeper imaging obtained is inferior to that from a dedicated deep reflection survey, it is more than adequate to address important geologic issues of both academic and practical significance. Stratigraphic ambiguity notwithstanding, the imagery is truly 3D, allowing recognition of features that are unrecognizable in 2D profiles. Such information is vital to understand the evolution of the basement structures, including such energy related issues as seismic risk associated with fluid injection near basement faults. The most significant aspect in this study is the demonstration of modern, nodal, continuously recorded industry surveys are routinely and serendipitously collecting an important 3D image to intrabasement depths. This already extensive and growing volume of deep crustal information should be examined and certainly should not be discarded. It has the potential to revolutionize our understanding of continental structure and tectonics to the same degree that 3D seismic surveying has revolutionized the resource exploration industry itself.

5.6 Figures

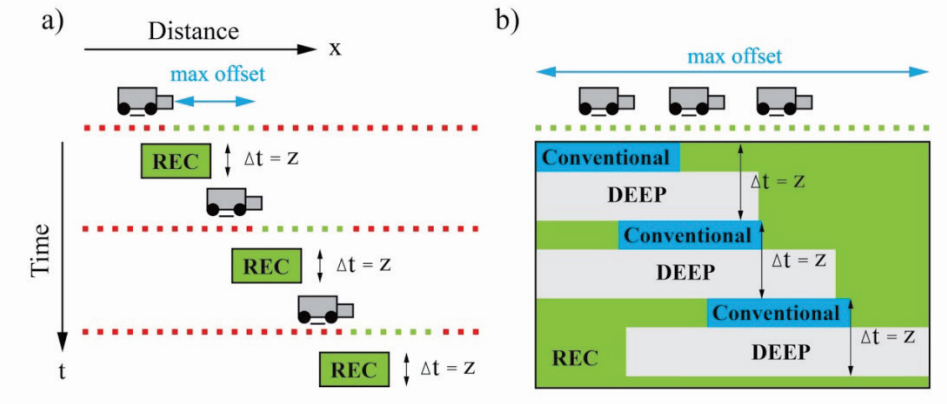

Figure 5.1: A comparison of (a) traditional roll-along multichannel reflection profiling

with (b) modern nodal recordings. Green and red dots are active and inactive channels, respectively. The green box represents recording in time and space. Light blue arrow shows maximum source receiver offset. Note that all channels record for the full duration of the nodal survey. The blue boxes represent the subset of the recordings that is typically harvested for exploration purposes. The green and gray boxes represent surplus recordings that contain nominally untapped information. The gray boxes correspond specifically to recording of deep reflections from beneath the zone of direct exploration interest.

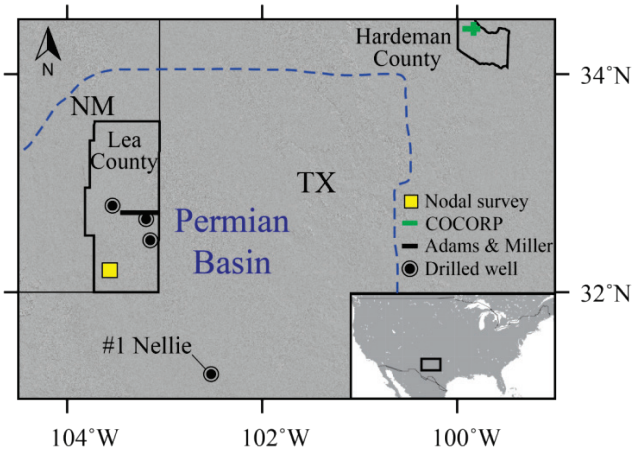

Figure 5.2: Portion of a 3D exploration survey conducted by Fairfield Nodal in the Permian Delaware Basin (blue dotted line) of south-eastern New Mexico. Green and black lines correspond to reflection surveys by COCORP (Brewer et al., 1981) and Adams and Miller 1995, respectively. Black dot indicates the location of relevant nearby wells (Muehlnerger et al, 1966).

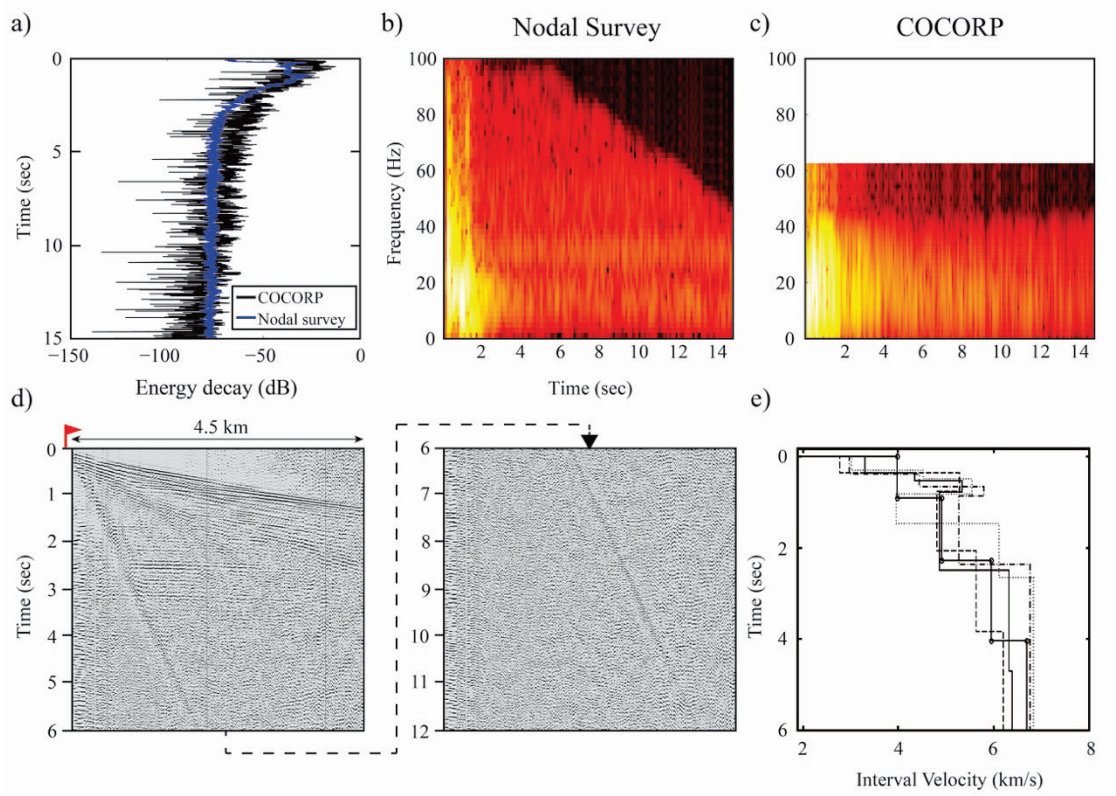

Figure 5.3: a) Average energy (10log10 amplitude2) of 19 correlated traces corresponding to source-receiver offsets of 400m for the nodal data (blue line) compared with a COCORP deep reflection survey collected in 1976 (black line). Traces are normalized relative to the amplitudes at 15 second in each case. Spectrogram for nodal traces b) compared with COCORP traces c) (Due to the lower sampling rate of the COCORP survey, no information was recorded above 62.5Hz). Note that the nodal result retains the same bandwidth as the COCORP data down to 15 second. d) A typical shot gather (wrapped around at 6 sec) produced by extended correlation of nodal data. Red flag represents the location of vibroseis. Prominent reflection energy is visible to travel times of at least 4 sec, with weaker coherency recognizable even at later travel times. e) Interval velocities computed from CRP analysis of the nodal data.

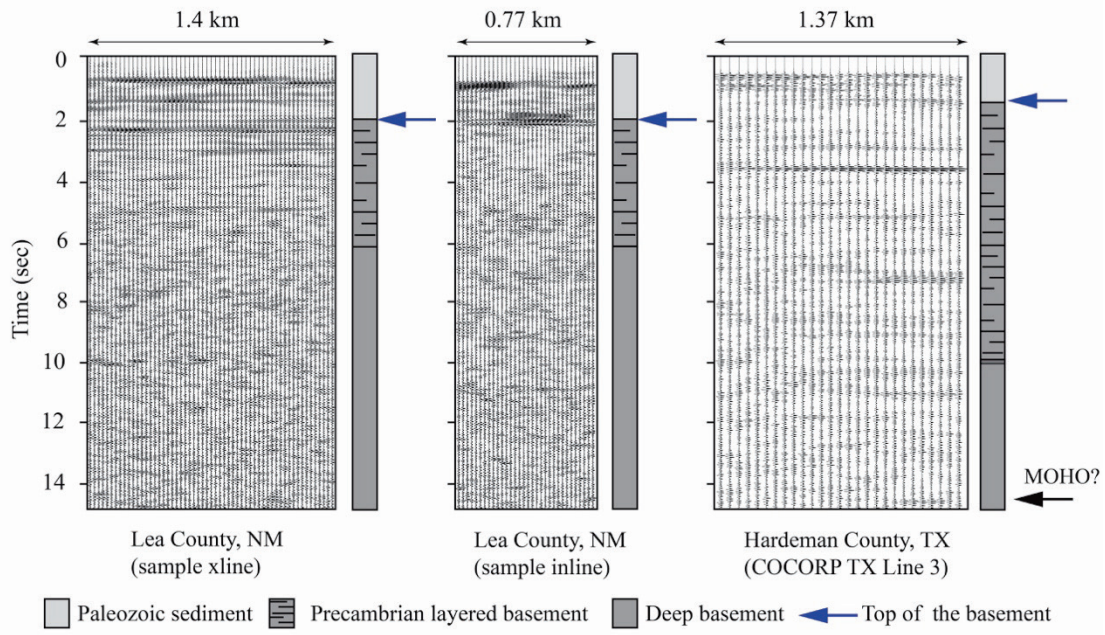

Figure 5.4: a) – b) 2D CMP stacked sections extracted from the 3D data volume produced in this study (SE New Mexico) and c) stacked section from a 2D COCORP profile in Hardeman County. The blue arrows indicate the top of Precambrian basement as reported from drill holes near each survey, respectively. Moho is expected at times greater than 14 sec in this area (Oliver et al., 1976). Note that the CRP spacing for the nodal profile is 25m, in contrast with that for the COCORP survevy (100m).

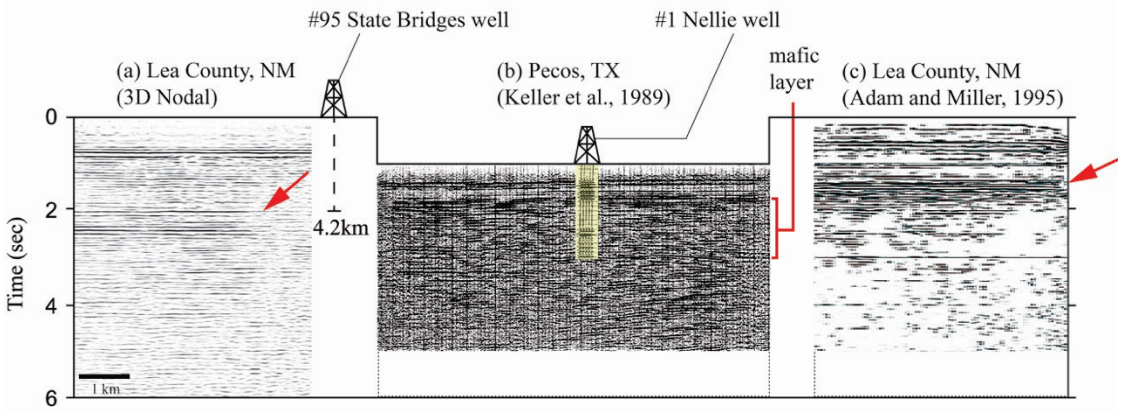

Figure 5.5: a) 2D CMP stacked section extracted from the 3D data volume produced in this study (SE New Mexico) from the surveying site and b) a reflection section from southwest Texas (Keller et al., 1989). The #1 Nellie well (see Figure 6.1 for location) is shown in (b) also with synthetic seismograms derived from the well logs (Adam and Miller 1995). Note that the Pecos section (b) has been shifted 1.2 sec downward to account for relatively thicker sediments in Lea County (a). The red arrows in (a) and

(c) indicate top of the interpreted igneous intrusion from each survey. Note an additional layer of granite material in (a) that is missing in (b) and (c).

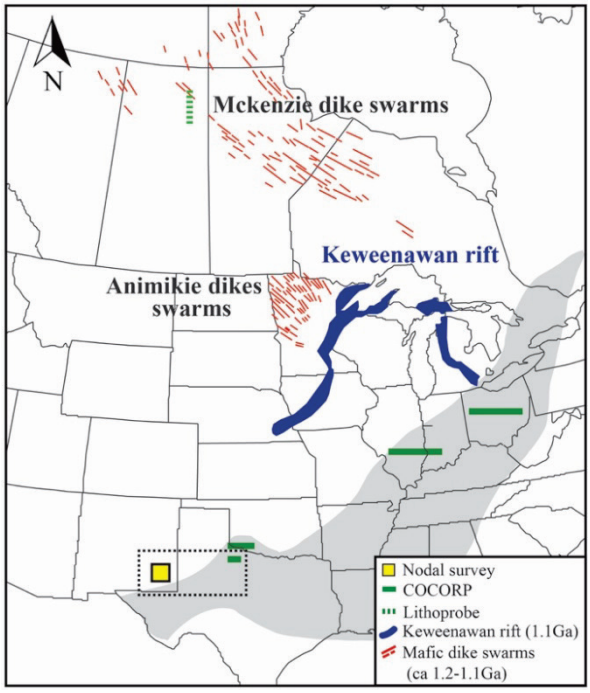

Figure 5.6: Depiction of Keweenawan rifting (blue) with Mckenzie and Animikie dike swarms (red). Gray shaded region in the midcontinent U.S. represents the Granite-Rhyolite terrains. Dotted box corresponds to the study area in Figure 5.2. Green solid and dotted green lines correspond to continental reflection surveys by COCORP and LITHOPROBE, respectively. Note these reflection profiles show similar basement layering as discussed in the main text. Modified from Whitmeyer and Karlstrom 2007.

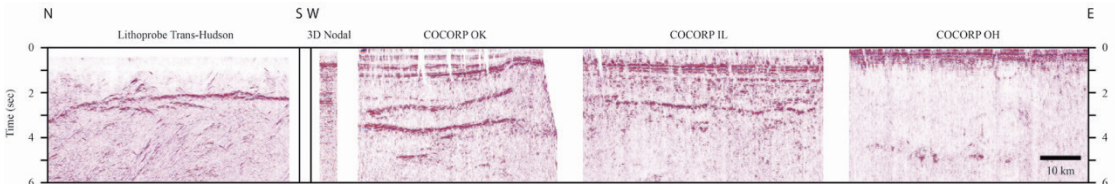

Figure 5.7: Layered basement sequence observed from seismic surveys in North American continent. Note the reprocessed produced in this study is labeled as "3D Nodal"

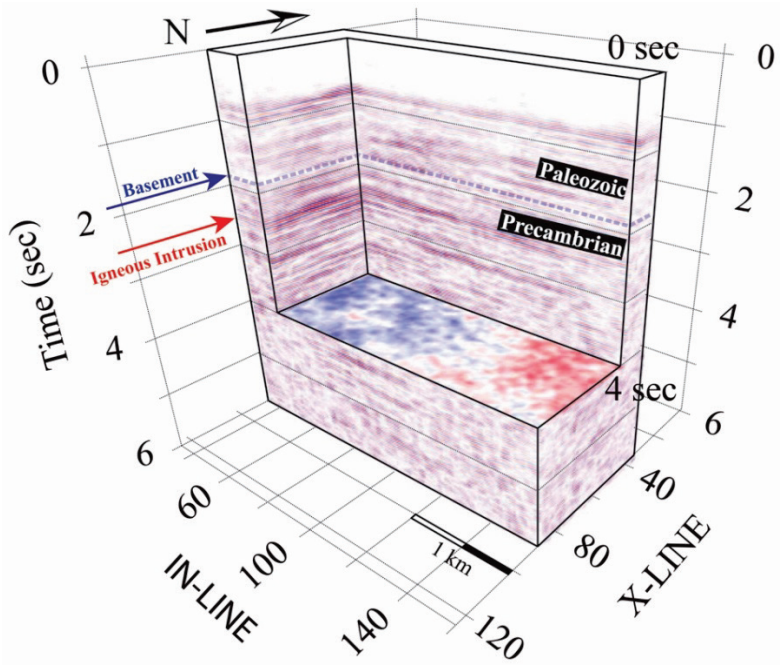

Figure 5.8: A 3D seismic reflection volume of the basement discussed in this study. The blue and red arrows indicate the top of Precambrian basement as reported from a drill hole near the survey and interpreted igneous intrusive layering within the basement, respectively.

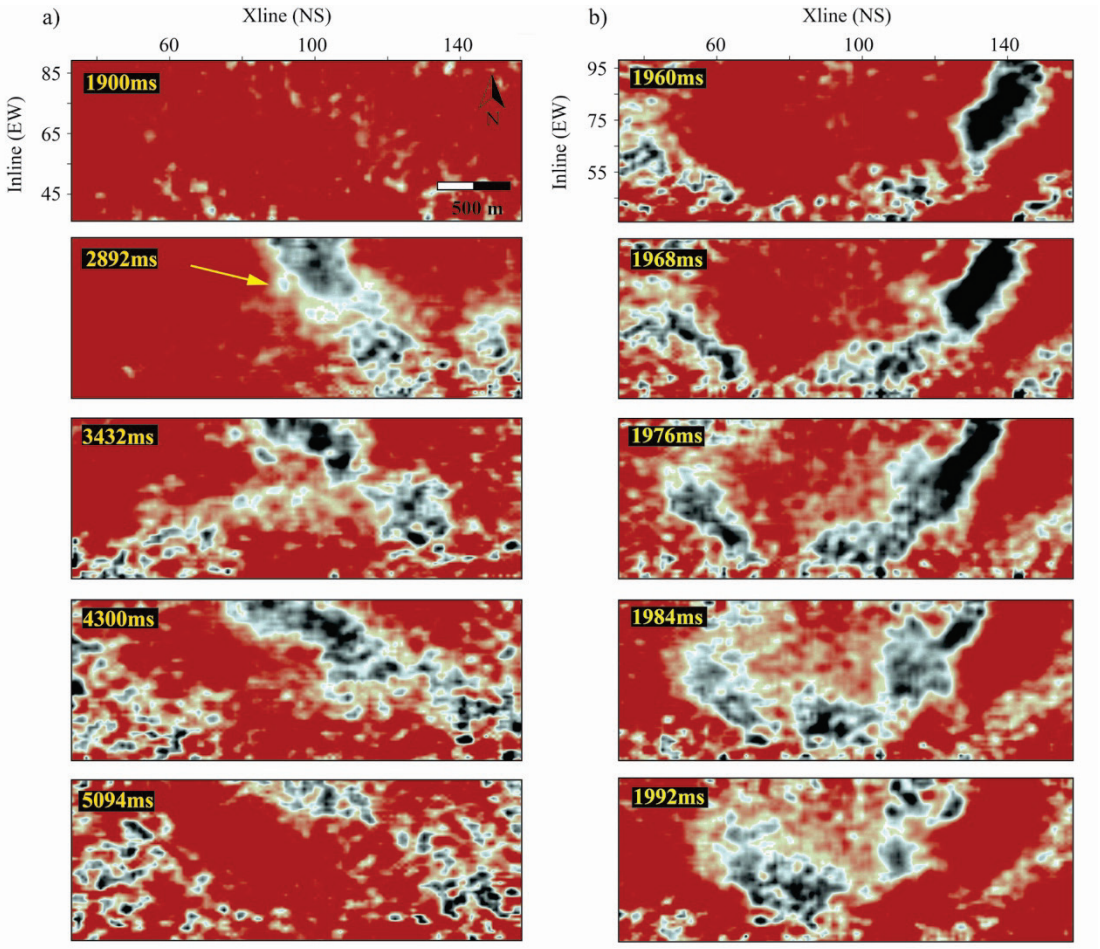

Figure 5.9: a) A series of seismic time slices for travel times from 1.9-5.1 second from 3D reflection data volume processed in this study. The linear reflection pattern (yellow arrow) could be interpreted as igneous dike, a feeder to the postulated sills making up the Precambrian layering. b) The shrinking ovoid pattern suggests a conical or saucer shaped reflector. Such geomteries have been associated with cuspate mafic sills in other areas (Polteau et al., 2008).

REFERENCES

Adams, D. C., and K. C., Miller. (1995), Evidence for late Middle Proterozoic extension in the Precambrian basement beneath the Permian basin: Tectonics, 14, 1263-1272.

Bonnichsen, B., & Kauffman, D. F. (1987), Physical features of rhyolite lava flows in the Snake River Plain volcanic province, southwestern Idaho. Geological Society of America Special Papers, 212, 119–145.

Brewer, J. A., L. D. Brown, D. Steiner, J. E. Oliver, S. Kaufman, and R. E. Denison.

(1981) Proterozoic basin in the southern Midcontinent of the United States revealed by COCORP deep seismic reflection profiling: Geology, 9, 569-575.

Brown, A. R.. (1986) Interpretation of three-dimensional seismic data: American Association of Petroleum Geologists and Society of Exploration Geophysicists.

Brown, L. D. (2013) From layer cake to complexity: 50 year of geophysical investigations of the Earth: The Geological Society of America Special Paper, 500, 233-258.

Bickford, M. E., W. R. Van Schmus, K. E. Karlstrom, P. A. Mueller, and G. D. Kamenov. (2015) Mesoproterozoic-trans-Laurentian magmatism: A synthesis of continent-wide age distributions, new SIMS U–Pb ages, zircon saturation temperatures, and Hf and Nd isotopic compositions, Precambrian Research, 265, 286–312.

Bussat, S., and S. Kugler. (2011), Offshore ambient-noise surface-wave tomography above 0.1 Hz and its applications, The Leading Edge, 30(5), 514–524.

Cook, F. A., L. D. Brown, S. Kaufman, J. E. Oliver, and T. A. Petersen. (1981) COCORP seismic profiling of the Appalachian orogen beneath the Coastal Plain of Georgia, Geological Society of America Bulletin, 92(10), 738–748.

Ellsworth, W. L. (2013). Injection-induced earthquakes. Science, 341(6142), 1225942.

Gaswirth, S., and K. R. Marra. (2016) Geologic-Based Assessment of Continuous Resources in the Permian Basin, Texas and New Mexico, USA, in AAPG Annual Convention and Exhibition.

Green, J. C., & Fitz, T. J. (1993), Extensive felsic lavas and rheoignimbrites in the Keweenawan Midcontinent Rift plateau volcanics, Minnesota: petrographic and field recognition. Journal of Volcanology and Geothermal Research, 54(3–4), 177–196.

Hansen, D. M., and J. Cartwright. (2006), The three-dimensional geometry and growth of forced folds above saucer-shaped igneous sills, Journal of Structural Geology, 28(8), 1520–1535.

Hauser, E. C. (1993), Grenville foreland thrust belt hidden beneath the eastern US midcontinent, Geology, 21(1), 61–64.

Henry, C. D., Price, J. G., Rubin, J. N., Parker, D. F., Wolff, J. A., Self, S., Barker, D. S. (1988), Widespread, lavalike silicic volcanic rocks of Trans-Pecos Texas. Geology, 16(6), 509–512.

Hills, J. M. (1984) Sedimentation, tectonism, and hydrocarbon generation in Delaware Basin, west Texas and southeastern New Mexico, The American Association of Petroleum Geologists Bulletin, 68, 250-267.

Horton, S. (2012). Disposal of hydrofracking waste fluid by injection into subsurface aquifers triggers earthquake swarm in central Arkansas with potential for damaging earthquake. Seismological Research Letters, 83(2), 250–260.

Inbal, A., R. W. Clayton, and J.-P. Ampuero. (2015), Imaging widespread seismicity at midlower crustal depths beneath Long Beach, CA, with a dense seismic array: Evidence for a depth-dependent earthquake size distribution, Geophysical Research Letters, 42(15), 6314–6323.

Kargi, H., and C. G. Barnes. (1995) A Grenville-age layered intrusion in the subsurface of west Texas: Petrology, petrography, and possible tectonic setting, Canadian Journal of Earth Sciences, 32(12), 2159–2166.

Keller, G. R., J. M. Hills, and R. Djeddi. (1980) A regional geological and geophysical study of the Delaware basin, New Mexico and west Texas, Field Trip Guideb. NM Geol. Soc, 31, 105–111.

Keller, G. R., J. M. Hills, M. R. Baker, and E.T. Wallin. (1989) Geophysical and geochronological constraints on the extent and age of mafic intrusions in the basement of west Texas and eastern New Mexico, Geology, 17, 1049-1052.

Keranen, K. M., Weingarten, M., Abers, G. A., Bekins, B. A., & Ge, S. (2014). Sharp increase in central Oklahoma seismicity since 2008 induced by massive wastewater injection. Science, 345(6195), 448–451.

Kim, W. Y. (2013), Induced seismicity associated with fluid injection into a deep well in Youngstown, Ohio. Journal of Geophysical Research: Solid Earth, 118(7), 3506–3518.

Lin, F.-C., V. C. Tsai, B. Schmandt, Z. Duputel, and Z. Zhan. (2013), Extracting seismic core phases with array interferometry, Geophysical Research Letters, 40(6), 1049–1053.

Mandler, H. A. F., and R. M. Clowes. (1997), Evidence for extensive tabular intrusions in the Precambrian shield of western Canada: A 160-km-long sequence of bright reflections, Geology, 25(3), 271–274.

Mayer, J. R., and L. D. Brown. (1986), Signal penetration in the COCORP Basin and Range-Colorado Plateau survey, Geophysics, 51(5), 1050–1055.

Miller, J. D., and E. M. Ripley. (1996), Layered intrusions of the Duluth complex,

Minnesota, USA, Developments in Petrology, 15, 257–301.

Mohorovičić, A., 1910, Das Beben vom 8. X. (1909) Jahrbuch des Meteorologischen Observatoriums in Zagreb (Agram) fur das Jahr 1909, Jahrgang 9, Teil 4, Abschnitt 1, p. 3–63.

Montgomery, S. L., J. Worrall, and D. Hamilton. (1999) Delaware Mountain Group, west Texas and southeastern New Mexico, a case of refound opportunity: part 1–Brushy Canyon, AAPG bulletin, 83(12), 1901–1926.

Muehlberger, W. R., C. E. Hedge, R. E. Denison, and R. F. Marvin. (1966) Geochronology of the Midcontinent Region, United States: Journal of Geophysical Research, 71, 5409-5426.

Nakata N., Snideder R., Tsuji T., Karner K., and T. Matsuoka. (2011) Shear wave imaging from traffic noise using seismic interferometry by cross-coherence: Geophysics, 76, SA97-SA106.

Okaya, D. A., and C. M. Jarchow. (1989) Extraction of deep crustal reflection from shallow vibroseis data using extended correlation: Geophysics, 54, 555-562.

Oliver, J., M. Dobrin, S. Kaufman, R. Meyer, and R. Phinney. (1976) Continuous seismic reflection profiling of the deep basement, Hardeman County, Texas: Geological Society of America Bulletin, 87, 1537-1546.

Polteau, S., A. Mazzini, O. Galland, S. Planke, and A. Malthe-Sørenssen. (2008) Saucer-shaped intrusions: Occurrences, emplacement and implications, Earth and Planetary Science Letters, 266(1), 195–204.

Pratt, T., R. Culotta, E. Hauser, D. Nelson, L. Brown, S. Kaufman, J. Oliver, and W. Hinze. (1989) Major Proterozoic basement features of the eastern midcontinent of North America revealed by recent COCORP profiling: Geology, 17, 505-509.

Quiros, D. A., L. D. Brown, and D. Kim. (2016) Seismic interferometry of railroad induced ground motions: body and surface wave imaging, Geophys J Int, 205(1), 301–313.

Schmandt, B., and R. W. Clayton. (2013) Analysis of teleseismic P waves with a 5200-station array in Long Beach, California: Evidence for an abrupt boundary to Inner Borderland rifting, Journal of Geophysical Research: Solid Earth, 118(10), 5320–5338.

Stiller, M.. (1991) 3-D vertical incidence seismic reflection survey at the KTB location, Oberpfalz, in Continental Lithosphere: Deep Seismic Reflections (eds R. Meissner, L. Brown, H.-J. Dürbaum, W. Franke, K. Fuchs and F. Seifert),

American Geophysical Union, Washington, D. C.

Ward, R. F., C. G. S. C. Kendall, and P. M. Harris. (1986) Upper Permian (Guadalupian) facies and their association with hydrocarbons–Permian basin, west Texas and New Mexico, AAPG Bulletin, 70(3), 239–262.

Welford, J. K., and R. M. Clowes. (2004) Deep 3-D seismic reflection imaging of Precambrian sills in southwestern Alberta, Canada: Tectonophysics, 388, 161-172.

Whitmeyer, S. J., and K. E. Karlstrom. (2007) Tectonic model for the Proterozoic growth of North America, Geosphere, 3, 220–259.

Yilmaz, Ö. (2001) Seismic Data Analysis: Society of Exploration Geophysicists.